Breakdown of topological type-II fracton phases

Master's Thesis in Physics

Presented by:

Matthias Walther

Submission date: 22.03.2019

Institut für Theoretische Physik I
Friedrich-Alexander-Universität Erlangen-Nürnberg

Supervisor: Professor Dr. Kai Phillip Schmidt

Abstract

Haah's cubic code is an exactly solvable, three-dimensional quantum spin model realizing topological fracton order. It is a promising candidate for a self correcting quantum memory due to its macroscopic energy barrier between different ground states. Here we analyse the quantum robustness of this topological fracton order in a homogeneous magnetic field at zero temperature. Technically, this is achieved by applying the method of perturbative continuous unitary transformation and a mean-field approach. In all cases studied, we find strong first-order phase transitions separating the topological fracton phase and the polarized phase.

Contents

Chapter 1

Introduction: Quantum computing and quantum memory

The digital revolution is the third industrial revolution. It is characterized by the mass production of digital logical circuits and its derived technologies. The internet has revolutionized communication and grants billions access to information. While we are still in the middle of the digital revolution and its influence on technology and society, the devices at the heart of the digitalization - micro chips - are in a difficult situation.

In 1965, former Intel CEO Gordan Moore predicted that the density of transistors in integrated circuits doubles every two years [1]. This prediction, now known as Moore's Law, has been true up to day [2]. However, this has proven to be increasingly harder, because the manufacturing process became more difficult with decreasing feature size. This is nicely illustrated by the fact that in 1998 the whole industry formulated the International Technology Roadmap for Semiconductors (ITRS). In this road map, manufactures and suppliers sat together and planned their next steps in order to fulfill Moore's law making it self fulfilling [2]. But even these combined efforts seem not to be able to continue Moore's law. The smallest structures in modern micro chips are about 14 nm wide. This corresponds to a few hundred atoms. Smaller structures are then coming in the regime of quantum fluctuations, which makes them unreliable. In 2016, the industry initiative renamed the ITRS to International Roadmap for Devices and Systems and replaced Moore's law by "More Moore", which shifts the focus form further miniaturization to specialized hardware for certain tasks [3].

As Moore's law is slowly lain down, the question arises: What comes next? One approach is to utilize quantum states instead of the classic bits. A classical bit can be in one of two possible states: 0 and 1. However, a quantum bit, or shorter a qubit, can not just be in the 0 or 1 state but rather in any superposition of these. We usually write

$$|\Psi\rangle = \alpha\,|0\rangle + \beta\,|1\rangle,$$

where α and β are complex numbers and $|\alpha|^2 + |\beta|^2 = 1$. When we consider a system with two qubits the corresponding state can be written as

$$|\Psi\rangle = \alpha_{00}\,|00\rangle + \alpha_{01}\,|01\rangle + \alpha_{10}\,|10\rangle + \alpha_{11}\,|11\rangle,$$

where again α_x are complex numbers and $\sum_x |\alpha_x|^2 = 1$. Note that, the basis now contains four orthogonal states ($|00\rangle, |01\rangle, |10\rangle$ and $|11\rangle$), while a classical system with two bits has only two

orthogonal basis states, namely $(1, 0)^T$ and $(0, 1)^T$. This is one of the aspects that makes quantum computation so promising. The number of basis states grows exponentially with the number of qubits n in a quantum computer. For example, the number of basis states in a quantum computer with 500 qubits is larger than the number of atoms in the universe. Hence, a realization of a quantum computer making use of these basis states can do calculations unthinkable for classical computers. [4]

There is an even more important aspect to quantum computing: cryptography. In the age of the internet, sharing data is much easier than ever before. However, when data is sensitive nobody except the sender and receiver of a message should be able to read it. This is where cryptography comes into play. Usually, cryptography schemes are based on problems that are hard to solve for a classical computer. For example, the widely used RSA algorithm relies on the difficulty of the prime-number factorization of large integers [5]. However, in 1995, Peter Shor showed that a quantum computer can solve this problem in polynomial time [6]. This sparked huge interest in quantum computation.

Physically, a quantum algorithm is an unitary transformation of the quantum state of the system. An universal quantum computer should therefore be able to implement an arbitrary unitary transformation on a highly entangled state. Additionally, we want to program a quantum computer in a similar fashion than a classical computer with a finite set of instructions [4]. Naturally, the realization of an universal quantum computer is challenging. The main difficulty to overcome is that quantum states are fragile. Hence, the quantum information can get lost due to imperfections in the circuits and coupling to the environment. For example, experiments studying qubits based on Josephson junctions must be performed at extremely low temperatures of $30 \, \mathrm{m \, K}$ [7]. In 1995, Shor introduced a scheme how to perform quantum computation with faulty circuits [8]. The idea is to store a logical qubit into several physical qubits. Given that the errors are rare enough, one can detect an error on a single physical qubit and actively restore the state. This is remarkable, but so far no scalable realization could be developed. Additionally, it seems more desirable to build a quantum computer that does not need active error correction. We call such a computer self-correcting.

Similar to a classical computer, a quantum computer can be build making use of the von Neumann architecture [9]. This divides the quantum computer into a central processing unit and a memory unit. We can use that in order to search for schemes for a quantum memory and for quantum gates independently. An experimental realization for this division is presented in [10].

A very promising and heavily investigated field for both aspects is topological quantum order [11]. This field was mainly instigated by D. Thouless, M. Kosterlitz, and D. Haldane who won the nobel prize in 2016 for that [12]. In contrast to Landaus theory of phases, topological phases have different physical properties without a broken symmetry [13]. Additionally, some of the phyical properties of topological phases depend - as the name implies - on the topology of the system. For the central processing unit, two-dimensional models are under investigation, because the reduced dimension gives rise to new types of particles. For that, consider two non-distinguishable, point-like particles in three dimensions. The wave function of the composite system can either be symmetric or anti-symmetric under the exchange of the two particles. A symmetric wave function corresponds to Bosons and an anti-symmetric one to Fermions. The spin-statistic theorem tells us that there are no other options. However, this is different in two dimensions, where so called anyons can pick up any phase under the exchange of two particles [14, 15]. Kitaev proposed to utilize the braiding of anyons for quantum gates [16], which started

the field of topological quantum computation [17]. Solid state physics is one of the most promising areas for finding two-dimensional systems that realize anyons [18].

While the movement and braiding of anyons are desired for a quantum gates, they are a problem for a self-correcting quantum memory. For example, Kitaevs two-dimensional toric code has topological non-trivial, degenerate, and locally non-distinguishable ground states that could serve as a quantum memory [16]. However, in chapter 2, we give an argument why the dynamics of the excitations make it not self-correcting. In [19], B. Terhal and S. Bravyi even showed that a self-correcting quantum memory is not possible in two dimensions. J.Haah and S. Bravyi identified so called string-logical operators as one of the reasons for this [20]. Additionally, they showed that three-dimensional models without so called string-logical operators are good candidates for a self-correcting quantum memory. Motivated by this, J. Haah constructed a cubic code in three dimensions, where the elementary excitations and composites of theses are not mobile [21]. We explain all of that in more detail in chapter 3. While the existence of such a model is remarkable by itself, we want to stress a crucial point. The elementary excitations found in Haah's code are immobile. This is fundamentally different from point-like particles in two and three dimensions, as we cannot categorize them by their exchange statistics. Hence, these kind of type-II fracton phases with such elementary excitations are a new type of quantum matter (see also section 3.6). Single type-I fractons, found for example in the X-Cube model [22], are immobile but composites can move in restricted subspaces. For the three-dimensional toric code in a magnetic field D. Reiss and K. P. Schmidt found a second-order phase transitions between the topological phase and a polarized phase in regimes where mobile quasi-particles dominate [23]. In contrast to that, they found a first-order phase transition where immobile quasi-particles dominate. As the elementary exciations in Haah's code are all immobile, we expect a first-order phase transition. The aim of this thesis is to explicitly investigate this by examining the quantum robustness of the type-II fracton phase in Haah's code in a homogeneous magnetic field. Additionally, the investigation of the quantum robustness of the fracton phase is crucial for a later application as a self-correcting quantum memory.

The thesis is structured in the following way. In the first two chapters we review the most crucial steps for the discovery of Haah's code. For that, we start with Kitaevs toric code as an intuitively accessible example for topological quantum order and show that is has degenerate, locally non-distinguishable ground states. We then give an argument why the mobility of excitations make it not suitable for a self-correcting quantum memory. Coming from that, we generalize the structure of the toric code to stabilizer codes and present two necessary conditions for a self-correcting quantum memory. In order to fulfill both of theses conditions, Haah constructed a three-dimensional model that does not have so called string-like operators, which we review in the second half of chapter 3. In chapter 4, we introduce the unperturbed Haah's code and discuss its symmetries, ground states and illustrate the immobility of the elementary excitations. The central object of the thesis is Haah's code in a homogeneous magnetic field, which we define at the end of chapter 4. In chapter 5 we introduce the methods used to investigate the phase transition between the topological fracton phase and a trivial phase. Finally, we find a first-order phase transition for all considered cases in chapters 6, 7 and 8.

Chapter 2

The toric code

In order to understand whats makes models with topological quantum order good candidates for quantum memory, we introduce Kitaev's toric code. First, we define the model and construct the ground state. As a next steps, we explain what makes the ground states suitable for a good quantum memory. However, in the second part we show that the dynamics of excitations prevent it from being self-correcting.

2.1 Definition and ground states

The toric code is one of the first and certainly one of the most influential models realizing topological quantum order, which we will define later. It was first introduced in 2003 by Alexei Kitaev [16]. The main motivation was the self-correcting character of conventional memory found on a hard drive. In such a hard drive, the information is stored in the collective magnetization of many magnetic moments. Hence, local fluctuations are not able to change the information. The toric code is a proposal to bring something similar to the quantum case.

It is defined on a square lattice with a single spin-1/2 particle at the edges of each unit cell (see figure 2.1). The Hamiltonian is

$$\hat{\mathcal{H}} = -J \sum_s \hat{A}_s - J \sum_p \hat{B}_p \tag{2.1}$$

with the coupling constant $J > 0$ and the operators

$$\hat{A}_s = \prod_{i \in s} \hat{\sigma}_i^x,$$

$$\hat{B}_p = \prod_{i \in p} \hat{\sigma}_i^z.$$

$\hat{A}_s$ is called a star and $\hat{B}_p$ a plaquette operator. The reason for this is that the spins, one of these operators act on, form a pattern that looks like a star or a plaquette. This is illustrated in figure 2.1. One can quickly check that

$$[\hat{A}_s, \hat{A}_{s'}] = [\hat{B}_p, \hat{B}_{p'}] = [\hat{A}_s, \hat{B}_p] = 0 \ \forall s, s', p, p', \tag{2.2}$$

$$\hat{A}_s^2 = \hat{B}_p^2 = \mathbb{1}. \tag{2.3}$$

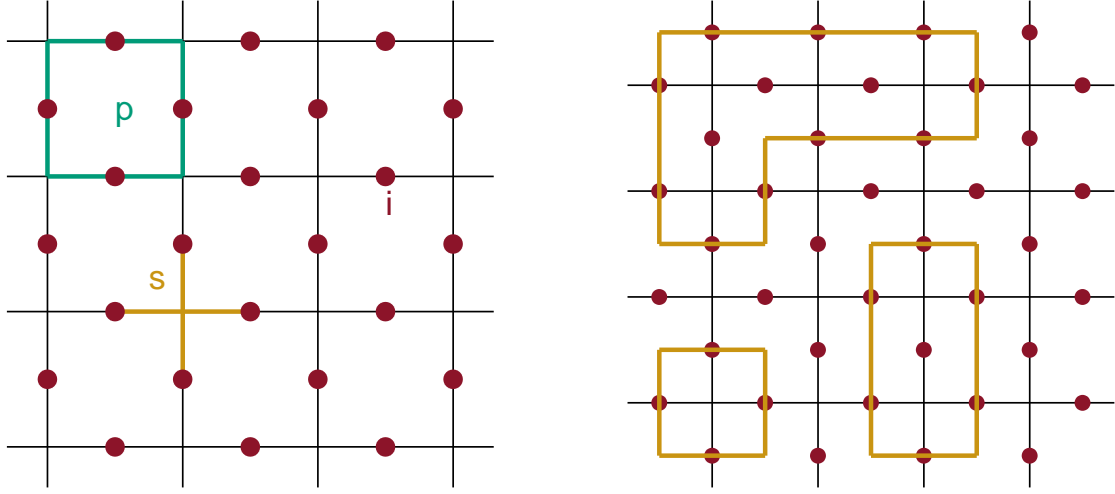We use these properties to construct the ground state.

Figure 2.1: Left: The toric code is defined on a square lattice with spin-1/2 particles sitting at the edges of the squares illustrated by the red dots. The operators are defined with respect to stars and plaquettes depicted in yellow and green. Right: The ground state of the toric code is the superposition of all possible configurations of contractible loops at different locations with different sizes and shapes. That includes small loops around a single star as shown in the bottom left. Two neighboring loops merge to a bigger loop as shown in the bottom right. That way various shapes and sizes of loops can emerge.

We start with the ground state for open boundary conditions. Equation 2.3 implies that the eigenvalues of all $\hat{A}_s$ and $\hat{B}_s$ are ±1. As there are two spin-1/2 particles in each unit cell, we have $2N$ particles in the lattice, where N is the total number of unit cells. That means that, we need to fix $2N$ two-valued spin degrees of freedom in order to completely describe the system. However, we also have $2N$ two valued, conserved operator degrees of freedom - namely the eigenvalues of all $\hat{A}_s$ and $\hat{B}_s$ operators. That means, we can fix the operator degrees of freedom instead of the spin degrees of freedom in order to completely describe any state. This has the huge advantage that the ground state is easily found in terms of operator eigenvalues, because the Hamiltonian in equation 2.1 is just the sum of the eigenvalue times $-J$. Hence, the ground state is

$$|0\rangle = \left|a_1 = +1, ..., a_{N_c} = +1, b_1 = +1, ..., b_{N_c} = +1\right\rangle,$$

where a_s is the eigenvalue of $\hat{A}_s$ and b_p is the eigenvalue of $\hat{B}_p$. This state is automatically an eigenstate of the Hamiltonian, because $[\hat{\mathcal{H}}, \hat{A}_s] = [\hat{\mathcal{H}}, \hat{B}_p] = 0$ for all stars and plaquettes. More formally, the $\hat{A}_s$ and $\hat{B}_p$ operators form a complete set of commuting observables and their eigenvalues are hence good quantum numbers [24]. We can even construct the ground state with respect to the spin degrees of freedom by using projectors

$$|0\rangle = \prod_s \underbrace{\left(\frac{\mathbb{1} + \hat{A}_s}{2}\right)}_{\substack{\text{Projector to} \\ a_s = +1 \text{ state}}} \prod_p \underbrace{\left(\frac{\mathbb{1} + \hat{B}_p}{2}\right)}_{\substack{\text{Projector to} \\ b_p = +1 \text{ state}}} |\Uparrow\rangle, \tag{2.4}$$

where $|\Uparrow\rangle$ is the state with all spins pointing in z-direction. Note that. instead of $|\Uparrow\rangle$ we can use any state that is not orthogonal to the ground state. In this form we can also visualize the ground

6

state. First of all, we can see that $\hat{B}_p |\Uparrow\rangle = |\Uparrow\rangle$. This holds, because $\hat{B}_p$ is a product of $\hat{\sigma}^z$ operators and hence leaves $|\Uparrow\rangle$ unchanged. Therefore, we are left with

$$
\begin{aligned}
|0\rangle &= \prod_s \left(\frac{\mathbb{1} + \hat{A}_s}{2} \right) |\Uparrow\rangle \\
&= 2^{-Nc} \left(\mathbb{1} + \sum_s \hat{A}_s + \sum_{s<s'} \hat{A}_s \hat{A}_{s'} + \sum_{s<s'<s''} \hat{A}_s \hat{A}_{s'} \hat{A}_{s''} + ... + \prod_s \hat{A}_s \right) |\Uparrow\rangle ,
\end{aligned}
$$

which is a highly entangled state. A single $\hat{A}_s$ operator acting on the polarized state flips the spins surrounding a star, forming a small loop. For a summand with two neighboring $\hat{A}_s$ operators, the shared spin is flipped twice and is back in its original state. Therefore, the two smaller loops merge into a bigger loop. The formation of loops with different sizes is illustrated in figure 2.1. Hence, $|0\rangle$ is the superposition of all possible configurations of contractible loops at different locations with various sizes and shapes. $|0\rangle$ is therefore often referred to as *loop soup*.

The key feature for the application of the toric code as a quantum memory arises when considering periodic boundary conditions. The main difference from the open-boundary case is that the $\hat{A}_s$ and $\hat{B}_p$ operators do not form a complete set of commuting observables anymore, because we find the relation

$$
\prod_s \hat{A}_s = \mathbb{1} \quad \text{and} \quad \prod_p \hat{B}_p = \mathbb{1}.
$$

This relation holds, because each $\hat{\sigma}_i^x$ appears twice in the product over all $\hat{A}_s$. As all Pauli operators commute with Pauli operators at different sites, we can write $\prod_s \hat{A}_s = \prod_i (\sigma_i^x)^2 = \prod_i \mathbb{1} = \mathbb{1}$. Conversely, this means that a_s can be determined by knowing all other $a_{s'}$. The same is true for the b_p. Together, we have two two-valued operator degrees of freedom less and can not fix all spin degrees of freedom. But the periodic boundary conditions also give rise to new operators that are not present in the open boundary case. An intuitive way of finding these is recalling that $|0\rangle$ only contains contractible loops. This makes sense for open boundary conditions, as non-contractible loops cannot be constructed in this geometry. However, for open boundaries, which is topologically equivalent to a two-dimensional a genus 1 torus, we have two non-contractible loops l_1 and l_2; one winding around the torus in x- and one in y-direction. Hence, we can define two new operators

$$
\hat{c}_1 = \prod_{s \in l_1} \hat{\sigma}_i^x \quad \text{and} \quad \hat{c}_2 = \prod_{i \in l_2} \hat{\sigma}_i^x. \tag{2.5}
$$

These commute with all $\hat{A}_s$ operators, because both consist of $\hat{\sigma}^x$ operators, and with all $\hat{B}_p$ operators, as they always share zero or two sites. Additionally, $\hat{c}_1^2 = \hat{c}_2^2 = \mathbb{1}$ and $[\hat{c}_1, \hat{c}_2] = 0$. That means that similar to the $\hat{A}_s$- and $\hat{B}_p$ operators the eigenvalues of $\hat{c}_1$ and $\hat{c}_2$ are ± 1. Therefore, we can add these two operator eigenvalues to the set of a_s and b_p and are back with a complete set of commuting observables that can fix all spin degrees of freedom. Using projectors, the ground state can then be written as

$$
|c_1, c_2\rangle = \left(\frac{\mathbb{1} + \hat{c}_1}{2} \right) \left(\frac{\mathbb{1} + \hat{c}_2}{2} \right) |0\rangle , \tag{2.6}
$$

where $|0\rangle$ is the ground state from equation 2.4. However, this ground state is now four-fold degenerate, because $\hat{c}_1$ and $\hat{c}_2$ commute with the Hamiltonian. Hence, the presence or absence of a contractible loop does not change the energy of the state. But quite remarkably, $\hat{c}_1$ and $\hat{c}_2$ are non-local operators. That means, by locally probing the system, we can not distinguish the ground states. Putting it in a different way, it seems plausible that local, thermal fluctuations are
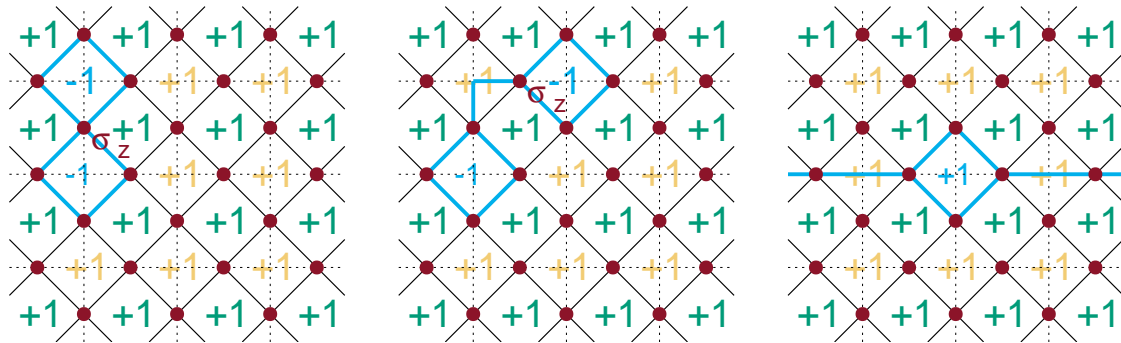
Figure 2.2: Dynamics of the elementary excitations of the toric code. The ground state of the toric code the state with all $\hat{A}_s$ eigenvalues (green) and all $\hat{B}_p$ eigenvalues (yellow) being equal to +1. Excitations of the toric code are flipped eigenvalues of $\hat{A}_s$ or $\hat{B}_p$. A pair of $\hat{A}_s$ excitations can be created by acting with a $\hat{\sigma}^z$ operator on one of the spins. This is shown on the left. A Excitation can be moved by acting with a $\hat{\sigma}^z$ operator on one of the adjacent spins without an additional energy cost. This is shown in the center. This can lead to one excitation winding around the torus and annihilating with the other excitation from the original pair, which is illustrated on the right. This process changes the ground state.

not able to change the ground state. This makes a ground state robust against perturbations This is true for quantum perturbations, but - as we will argue in the following section - it does not hold for thermal fluctuations [13].

2.2 Excitations and string-like operators

An elementary excitation in the toric code is a flipped eigenvalue of either an $\hat{A}_s$ or $\hat{B}_p$ operator. We can create a pair of $\hat{A}_s$ excitations from the ground state by acting with $\hat{\sigma}_i^z$ on a spin i. The two $\hat{A}_s$ operators in that include $\hat{\sigma}_i^x$ anti-commute with $\hat{\sigma}_i^z$ and therefore the eigenvalue of the adjacent stars get flipped. All others $\hat{A}_s$ and $\hat{B}_p$ operator commute with $\hat{\sigma}_i^z$. Acting with a $\hat{\sigma}_j^z$ on a neighboring site j flips the eigenvalue of the original excitation back to +1, but also flips the eigenvalue of the other plaquette to −1. Hence, the elementary excitation hopped from one site to an neighboring site. By iterating this, we can move an excitation along a line. This process is illustrated in figure 2.2. For periodic boundary condition, an excitation can wind around the torus in either directions and can then be annihilated with the second excitation of the original pair. This however changes the ground state, as a non-contractible loop was formed by the moving excitation. The fact that these processes are possible and only require two excitations, provides an good intuition why the toric code is no candidate for a self-correcting quantum memory. Thermal fluctuations can easily create two excitations and there is no process hindering the excitations from moving. Indeed, S. Bravyi and B. Terhal argue in [19] that a macroscopic energy barrier between ground states is a necessary condition for a self correcting quantum memory. We will discuss their idea in the next chapter. Before that, we make some final remarks on the toric code.

2.3 Remarks on the toric code

The toric code is much richer than what we are able to discuss in this thesis. However, we want to mention a few more interesting aspects here. As already mentioned in the introduction, Kitaev introduced abelian anyons showing non-trivial exchange statistics in his original work on the toric code [16]. This sparked the idea of topological quantum computing [17].

The toric code can also be derived as limit of the Kitaev honeycomb model, which is a model with only two-spin interactions. This way the complicated four-spin interactions of the toric code can be constructed from a more realistic model, which give hope for an experimental realization in a solid [25].

The full phase diagram of the toric code in a homogeneous magnetic field was studied in [26]. This publication is also a good example of how the methods used in this thesis can be applied to a topological phase.

Chapter 3

The way to Haah's code, its thermal properties and fractons

In this chapter we give a short overview of the most important steps toward the discovery of Haah's code. We start by introducing a more general class of quantum codes called stabilizer codes and recognize the toric code as one of theses models. We then introduce necessary conditions for a self-correcting quantum memory. One of them will be a macroscopic energy barrier and we explain that models without string logical operators fulfill this condition. At the end, we illustrate how Haah's code was constructed as a model without string logical operators.

3.1 Stabilizer codes

In this section, we introduce the concept of stabilizer codes. This will generalize the structure of the toric code as we want to change to models such that it becomes a self-correcting quantum memory. All definitions are taken from [20]. Note that, the definitions refer to qubits instead of spin degrees of freedoms, which both describe two-valued degrees of freedom.

3.1.1 Topological quantum order

We start with the most underlaying concept: topological quantum order (TQO) [11]. There are many different ways of defining TQO. The property that makes TQO important to quantum memory is that a Hamiltonian that exhibits TQO has degenerate ground states that are locally indistinguishable. We will restrict ourself to this definition. However, there are more properties that define TQO. One of the most notable is topological entanglement entropy that was introduced by Kitaev and Preskill in [27] and independently by Levin and Wen in [28].

3.1.2 Stabilizer codes

A *stabilizer Hamiltonian* is defined as

$$\hat{\mathcal{H}} = -\sum_{a=1}^{M} \hat{G}_a,$$

(3.1)

where each $\hat{G}_a$ is a multi-qubit Pauli operators, e.i. a tensor product of Pauli-x, -y, z operators and identity with an overall sign ±1. All $\hat{G}_a$ operators commute and square to identity. Hence,

$$[\hat{G}_a, \hat{G}_b] = 0 \ \forall a,b \quad \text{and} \quad \hat{G}_a^2 = \mathbb{1}. \tag{3.2}$$

The abelian group $\mathcal{G}$ generated by $\hat{G}_1, ..., \hat{G}_n$ is called *stabilizer group*. Therefore, $\mathcal{G}$ includes all operators that can be written as a product of operators $\hat{G}_1, ..., \hat{G}_n$. Note that, in order to be physical, the stabilizer models considered on the way to Haah's code were local stabilizer codes. That means that, each $\hat{G}_a$ only acts on the corners of a hypercube in D dimensions.

We can directly see that the toric code is a stabilizer code, because the $\hat{A}_s$ and $\hat{B}_p$ operators fulfill the requirements in equation 3.2. The operators in the stabilizer group correspond to operators creating and annihilating contractible loops.

3.1.3 Ground state and logical operators

We will only consider frustration free Hamiltonians. A *ground state* $|\Psi_0\rangle$ is then the state with

$$\hat{G}_a |\Psi_0\rangle = + |\Psi_0\rangle \tag{3.3}$$

for all a. A Pauli operator E that flips no eigenvalues of any $\hat{G}_a$ is either a stabilizer ($E \in \mathcal{G}$) or a *logical operator* ($E \notin \mathcal{G}$, but E commutes with $\mathcal{G}$). A logical operator E maps a ground state to an orthogonal ground state.

The definition of the ground state mirrors exactly the way we constructed the ground state for the toric code, which we identified as the loop soup in equation 2.4. We can also name the logical operators in the toric code. These are $\hat{c}_1$ and $\hat{c}_2$ creating and annihilating non-contractible loops.

Starting from this more general notion of a stabilizer code, we will now summarize the most important steps leading to the discovery of Haah's code.

3.2 Macroscopic energy barrier

In [29] S. Bravyi and B. Terhal formulate two necessary conditions for a quantum spin system realizing a self-correcting quantum memory. The first is that, a candidate for a self-correcting memory must have degenerate ground states and every logical operator must act non-trivially on a macroscopic number of qubits. Otherwise, an interaction with the environment on a few spins destroys the encoded information. The second condition states, that a macroscopic energy barrier has to be traversed by any sequence of single-qubit Pauli errors resulting in an undetectable error. This makes sure that local errors cannot accumulate in some energy dissipation process to an undetectable error. For the toric code, the logical operators $\hat{c}_1$ and $\hat{c}_2$ act on L spins, where L is the linear system size. Hence, the first condition is fulfilled. But, as we explained in chapter 2.1, we only need to create two excitations in order to change the ground state, witch is an undetectable error. Therefore, the toric code violates the second condition.

S. Bravyi and B. Terhal also showed in the same paper that the first condition is always violated by local stabilizer codes in one dimension, while the second condition is always violated by local stabilizer codes in two dimensions. That means that a self-correcting quantum memory based on local stabilizer code must be at least three dimensional.

3.3 String logical operators

As illustrated in chapter 2.2, the reason why the toric code does not have a macroscopic energy barrier between ground states, is that excitations can move along a line without any energy cost. Therefore, logical operators even with a non-trivial action on a macroscopic number of spins can be realized by a sequence of locally acting operators. In [20], S. Bravyi and J. Haah argue that the existence of so called *string logical operators* prevents the existence of a macroscopic energy barrier also in three dimensions. Therefore, they formulated the no-string rule. Informally, it states that one cannot create (clusters of) excitations at the two ends of a string that cannot be created from local Pauli operators if the string is sufficiently long. Conversely, two clusters of excitations must be created from locally acting Pauli operators if they are sufficiently far away. They were able to show that a model with TQO that obeys the no string rule has an energy barrier for any logical operator of a least $c \cdot \log(L)$, where c is a constant and L is the linear lattice size. Hence, if a local stabilizer code without string logical operators exists, it does fulfill Bravyi's and Terhal's second condition for self-correcting quantum memory.

3.4 Construction of Haah's code

Motivated by this, Haah systematically searched for three-dimensional models without string logical operators. The results were published in [21]. In order to limit the number of candidates while also ruling out models with obvious string local operators, he imposed four conditions on the stabilizer codes.

1. There are one or two qubits per site in the infinite simple cubic lattice $\mathbb{Z}^3$.

2. The stabilizer group $\mathcal{G}$ is translation invariant and is generated by two types of operators acting on the corners of a elemental cube.

3. If a logical operator E is a single-site operator, then E is identity up to a phase.

4. If a logical operator l is supported along one of the three coordinate axis, along one of the six face diagonals or along one of the four body diagonals, then l is identity up to a phase.

Condition 1 is a restriction to cubic models for simplicity. The focus on models with one or two qubits per site is motivated by condition 2. Again, for simplicity, the search is limited to local stabilizer codes with two stabilizer operators per cube that generate $\mathcal{G}$. The number of qubits per site should be limited by the number of stabilizer operators per cube in order to obtain an exactly solvable model, which explains this part in condition 1. If the code had a single-site logical operator, two ground states could be mapped to each other by local errors. This would violate the first condition presented in section 3.2. Therefore, condition 3 is imposed. Condition 4 forbids trivial string like logical operators along a straight line. Note that this does not imply the absence of string logical operators, but it reduces the number of candidates.

Haah then analyzed the conditions algebraically and formulated efficient ways of implementing them. After an extensive search, he found 15 models that fulfilled condition 1-4. Five of them obeyed a global no-string rule and hence realized a macroscopic energy barrier between ground states. The most symmetric solution was further investigated and is now known as Haah's code.

3.5 Thermal stability

Before we move on to the main motivation of this thesis, we will briefly discuss the results of further analysis on the thermal properties of Haah's code. In [29], Bravyi and Haah investigated the quantum self-correction of the model analytically and numerically. They showed that the memory time for qubits associated with the logical operators mentioned at the end of section 4.2 is at least $L^{\beta c}$ where β is the inverse temperature of the heat bath and c is a constant. However, this is only true for system sizes L that are smaller than a critical value L_c that grows exponentially with β. Therefore, Haah's cubic code can be called a partially self-correcting quantum memory.

Even though this shows that Haah's code is not a fully self-correcting quantum code, it is the first model that shows self-correcting behavior, which is remarkable by itself. However, as we argued in the introduction, the phases featuring fundamentally immobile elementary excitations like the ones in Haah's code are a new type of quantum matter called fractons. In the next section, we introduce a categorization of fractons.

3.6 Fractons

Haah's code is one of the first models that realize so called *fracton-topological order*. TQO is often understood in the framework of topological quantum filed theory. World lines of elementary quasi-particles are described by Wilson lines and the braiding of these lines determines the exchange statistics of the particles [30]. However, fractons do not fit in this scheme due to the lack of mobile particles. That makes the phases featuring fractons a new kind of topological quantum order. Vijay, Haah and Fu categorize fracton phases in [22] into two types:

> **Type I**: Type-I fractons are excitations on the corners of *membrane* operators. The nature of the membrane operators allows composites of excitations to move in lower-dimensional subsystems. Examples for type I fractons are the X-Cube model and the checkerboard model [22].

> **Type II**: Type-II fractons are excitations on the corner of *fractal* operators. The fractal character of the operator makes it impossible for composites to be mobile. Hence, all excitations and composites are fundamentally immobile.

Haah's code and all other models constructed in [21] are type-II fractons. We will illustrate the immobility of the elementary excitations in Haah's code in chapter 4.4.

As this new type of topological order is new and three-dimensional models are usually more difficult to investigate, not much is know about fracton phases. The aim of the thesis is to gain some insight on the properties of Haah's code in a homogeneous magnetic field. Therefore, we investigate the zero-temperature phase transition between the topological phase and a trivial phase in order to study the quantum robustness of the fracton phase.

Chapter 4

Haah's code and magnetic fields

In this chapter we introduce Haah's code. We discuss the symmetries, introduce the ground state and discuss its degeneracy. Subsequently, we illustrate the properties of the operators such as the fractal character and the immobility of the excitations. Finally, we introduce the central object of this thesis: Haah's code in a homogeneous magnetic field.

4.1 Definition

Haah's code is defined on a cubic lattice. Each vertex of the lattice is occupied by two spin-1/2 particles. We will denote one of them with σ and the other one with μ, which is indicated in figure 4.1. The Hamiltonian of the system is

$$\hat{\mathcal{H}} = -J \sum_c \left(\hat{A}_c + \hat{B}_c \right), \tag{4.1}$$

with

$$\hat{A}_c = \hat{\mu}_j^z \hat{\mu}_k^z \hat{\sigma}_l^z \hat{\mu}_m^z \hat{\sigma}_n^z \hat{\sigma}_p^z \hat{\sigma}_q^z \hat{\mu}_{q'}^z,$$
$$\hat{B}_c = \hat{\sigma}_i^x \hat{\mu}_i^x \hat{\mu}_j^x \hat{\mu}_k^x \hat{\sigma}_l^x \hat{\mu}_m^x \hat{\sigma}_n^x \hat{\sigma}_{p'}^x,$$

where we used the labeling of the corners of the cube according to figure 4.1. $\hat{\sigma}_i^\alpha$ with $\alpha \in \{x, y, z\}$ denotes the action of the Pauli-α operator on spin σ_i and $\hat{\mu}_i^\alpha$ the action of the Pauli-α operator on spin μ_i. $J > 0$ is the coupling constant of the system.

The action of $\hat{A}_c$ and $\hat{B}_c$ operators is visualized in figure 4.1. There, we use capital characters to illustrate the action of the operator on each spin. The left character represents the action of the operator on the σ-spin and the right character the action on the μ-spin. For example, XI represents the tensor product $\hat{\sigma}^x \otimes \mathbb{1}$ and ZZ is $\hat{\sigma}^z \otimes \hat{\mu}^z$. The axis in the figure define the coordinate system used throughout this thesis.

Haah's code is a stabilizer code. That means that

$$\left[\hat{A}_c, \hat{B}_{c'} \right] = 0, \ \left[\hat{A}_c, \hat{A}_{c'} \right] = 0, \ \left[\hat{B}_c, \hat{B}_{c'} \right] = 0 \ \forall c, c' \tag{4.2}$$

and

$$\hat{A}_c^2 = \hat{B}_c^2 = \mathbb{1} \ \forall c. \tag{4.3}$$

which implies that the eigenvalues a_c of the $\hat{A}_c$ operators and b_c of the $\hat{B}_c$ operators are ± 1.
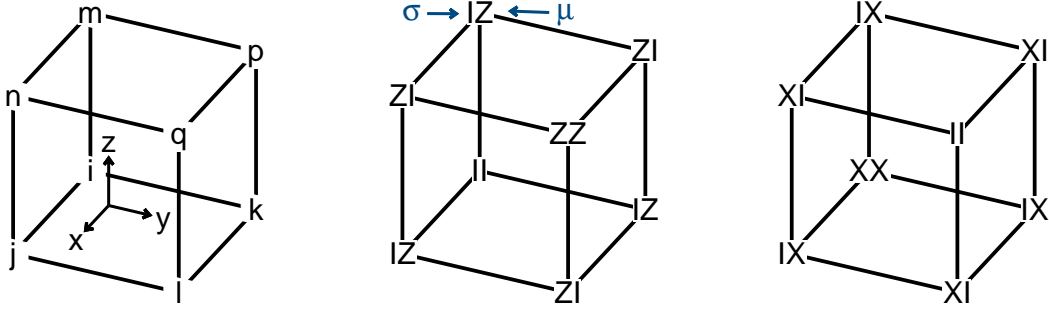
Figure 4.1: Illustration of the $\hat{A}_c$ and $\hat{B}_c$ operators that define Haah's code. The cube on the left shows the chosen labeling of the corners of the cube and the used coordinate system throughout this thesis. There are two spins on each vertex of the lattice. We call the left one σ and the right one μ. The sketch in the center illustrates the action of the $\hat{A}_c$ operator on the spins at the corners of the cube. IZ represents the tensor product $\mathbb{1} \otimes \hat{\sigma}^z$, where the operator on the left acts on the σ spin and the operator on the right on the μ spin. The sketch on the right illustrates the action of the $\hat{B}_c$ operator on the spins.

4.2 Ground state and ground-state degeneracy

In this section we investigate the ground state of Haah's code and the ground-state degeneracy. This is particularly important for the application as a quantum memory, as usual schemes use degenerate ground states for storing qubits. We start by considering open boundary conditions.

4.2.1 Open boundary conditions

As both toric code and Haah's code are stabilizer codes, we can construct the ground state of Haahs code in the same way as in section 2.1. In each unit cell of the cubic lattice we have two two-valued spin degrees of freedom and two two-valued operator degrees of freedom. Therefore, the ground state of Haah's code can directly be written as

$$|0\rangle = |a_c = b_c = +1, \ \forall c\rangle,$$

where a_c is the eigenvalues of $\hat{A}_c$ and b_c is the eigenvalue of $\hat{B}_c$. We can again construct the ground state with respect to the spin configuration using projectors:

$$|0\rangle = \prod_c \underbrace{\left(\frac{\mathbb{1} + \hat{A}_c}{2}\right)}_{\substack{\text{Projector to} \\ a_c = +1 \text{ state}}} \underbrace{\left(\frac{\mathbb{1} + \hat{B}_c}{2}\right)}_{\substack{\text{Projector to} \\ b_c = +1 \text{ state}}} |\Uparrow\rangle . \tag{4.4}$$

In contrast to the toric code, the operators for Haah's code do not have an easy geometrical form. Hence, we cannot visualize the ground state of Haah's code. But in many cases one can think of a *fractal soup* in analogy to the loop soup.

4.2.2 Periodic boundary conditions

For periodic boundary conditions, Haah's code is more complicated than the toric code. The reason is that, there is no exact expression for the relations between the operators for all system

sizes due to the complex nature of the operators. In [21] Haah found an upper and a lower bound for the number of degenerate ground states. These bounds will be introduced in the following and we start with the lower bound.

Lower bound

For periodic boundary conditions in a $L \times L \times L$ lattice, one finds at least one relation between each type of operators. It is the same we found for the toric code in chapter 2.1, namely that the product of all $\hat{A}_c$ operators equals identity. The reason for this is that each $\hat{\sigma}_i^z$ and $\hat{\mu}_i^z$ appears four times in the product of all $\hat{A}_c$ operators. As a consequence, on can determine the eigenvalue of a single operator by knowing the eigenvalues of all other operators. This also holds for the $\hat{B}_c$ operators

$$\prod_c \hat{A}_c = \mathbb{1} \quad \Longrightarrow \quad \hat{A}_c = \prod_{c' \neq c} \hat{A}_{c'}, \tag{4.5}$$

$$\prod_c \hat{B}_c = \mathbb{1} \quad \Longrightarrow \quad \hat{B}_c = \prod_{c' \neq c} \hat{B}_{c'}. \tag{4.6}$$

That means, we cannot fix all N_c spin degrees of freedom as we only have $N_c - 2$ independent operator degrees of freedom left. Hence, the lower bound for the ground-state degeneracy is $2^2 = 4$.

Upper bound

The upper bound for the ground-state degeneracy is 2^{4L}, witch corresponds to $4L$ qubits. Consider a set S of $\hat{A}_c$ operators outside a tunnel along the z-axis with a 2×1 cross section. Let K be a linear combination of operators in S. We require that K is identity. We will show that the only possible linear combination realizing K is the zero combination. Choose the tunnel such that the coordinates of the corners of the cross section of the tunnel are $x \pm 1$ and $y = 0, 1$. This is illustrated in figure 4.2. Consider the line given by $x = 0$, $y = 1$. At any given edge on this line the linear combination of the two operators outside the tunnel adds up to one of the following actions (reading downwards)

$$\begin{aligned}
\text{a)} \quad 0 \cdot \hat{A}_1 + 0 \cdot \hat{A}_2 &= II - II, \\
\text{b)} \quad 1 \cdot \hat{A}_1 + 0 \cdot \hat{A}_2 &= IZ - II, \\
\text{c)} \quad 0 \cdot \hat{A}_1 + 1 \cdot \hat{A}_2 &= ZI - IZ, \\
\text{d)} \quad 1 \cdot \hat{A}_1 + 1 \cdot \hat{A}_2 &= ZZ - IZ.
\end{aligned}$$

As we imposed that the linear combination of operators outside the tunnel is identity, any action that is not identity on a certain edge must be canceled by the action on the neighboring edges. Therefore, reading downwards, a) must always be followed by a), b) must be followed by a), and c) and d) must be followed by b), which again must be followed by a). That means that after two steps any sequence reaches the zero combination a), which can only be followed by further zero combinations. Due to the periodic boundary conditions, the only consistent sequence is the zero combination along the line. Therefore, the linear coefficients for K on the tube next to the original tube are zero. Together with the original tube, this new tube forms the bigger tube illustrated in
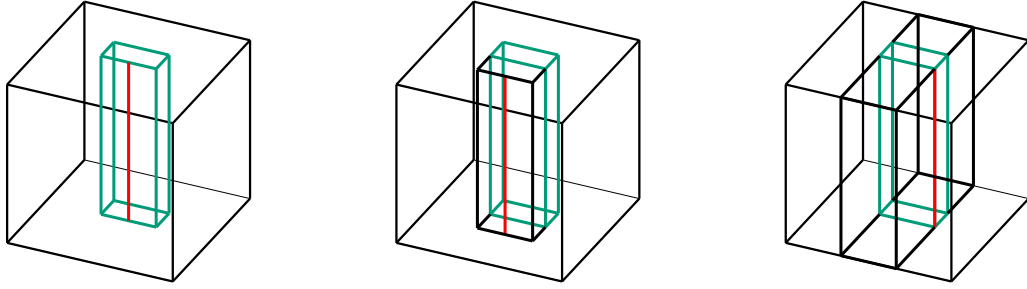
Figure 4.2: Proof of the upper bound for the ground-state degeneracy. Suppose a linear combination of $\hat{A}_c$ operators is identity. We start from tube with cross-section 1×2 shown on the left. One can show that the only allowed sequence of operators outside the tube along the red line must be the zero combination. This argument can be iterated as, shown in the center, until these tubes form a slap. A similar argument can be made for the red line on the right. This way, we can show that all operators outside the tube must be identity. [21]

the center of figure 4.2. The former argument can be repeated along the central line on this newly fixed tube. We can iterate this scheme until we reach the back of the original tube forming a slab. This way we showed K must be the zero combination on this slab. As a next step, we choose a line on the face of the slab and can argue in a similar way by finding sequences that are only consistent for the zero combination. That way we can show that K must be the zero combination.

In conclusion, any logical operator can only be non-trivial for the $2L$ $\hat{A}_c$ and - due to symmetry - the $2L$ $\hat{B}_c$ operators inside the original tube. Together, there is a maximum of 2^{4L} options to set these operators. This corresponds an upper bound of 2^{4L} degenerate ground states or $4L$ encoded qubits.

Empirical results and plane logical operators

Despite the fact that there is no exact expression for the ground-state degeneracy, Haah found an empirical expression for the ground-state degeneracy for $2 \leq L \leq 200$ in [21]. The results are plotted in figure 4.3. One can see that, the number of encoded qubits is always within the derived bounds and usually oscillates between 2 for odd and 6 for even numbers. However, there are certain magical numbers that come with a peak, most notable Ls that are divisible by powers of 2, 15 or 63.

Per construction, Haah's code does not have string-like operators. Nevertheless, it is important to find explicit expressions for logical operators, as these are the ones that could be used to measure the stored qubits. Instead of string-like operators Haah constructed so called *plane logical operators*. These are operators, where a single site operator E in repeated on a plane perpendicular to the vector $[x, y, z]$. The notation for such a plane-logical operators is $\sigma_E^{(x,y,z)}$. Haah explicitly states the operators $\sigma_{IX}^{[1,0,0]}$ and $\sigma_{ZZ}^{[1,-1,0]}$. These two operators commute for even system sizes and thus could be used to measure the corresponding qubits.
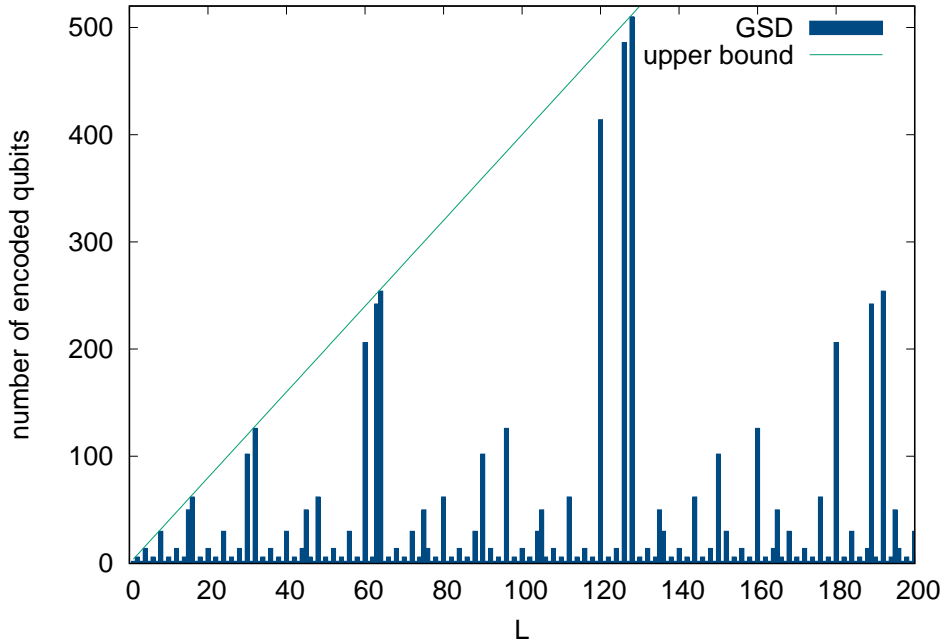
Figure 4.3: Number of encoded qubits for Haah's code [21]. The value oscillates between 2 for odd and 6 for even numbers. Additionally, there are peaks, most notable for *L*s that are divisible by powers of 2, 15 or 63

4.3 Visualization of three-dimensional lattices

Before we start discussing the properties of the operators and elementary excitations in Haah's code, we introduce a way to visualize these objects. The reason for introducing this visualization scheme is that, drawing the cubes in the conventional way like shown on the left of figure 4.4 gets messy for larger lattices. Many intersecting lines make it hard to distinguish the different cubes from each other. Therefore, instead of drawing the whole three-dimensional cubes, we take *xy*-planes intersecting the center of the cubes. Then we rescale the *z*-axis until the planes do not overlap anymore. The ground state is the state where all eigenvalues of $\hat{A}_c$ and $\hat{B}_c$ are +1. In our visualization, this state is denoted by coloring all squares white. We visualize an flipped eigenvalue of a $\hat{A}_c$ operator by coloring the corresponding squares yellow. If a $\hat{B}_c$ eigenvalue is −1, we color the square blue. If both the $\hat{A}_c$ and the $\hat{B}_c$ eigenvalue are −1 we color the cube green. This color scheme reflects the usual subtractive color mixing of blue and yellow to green.

4.4 Symmetries and fractal character

The most useful symmetry of Haah's code is that a $\hat{B}_c$ can be mapped to $\hat{A}_c$ by

- Lattice inversion,

- Renaming σ to μ and vice versa,

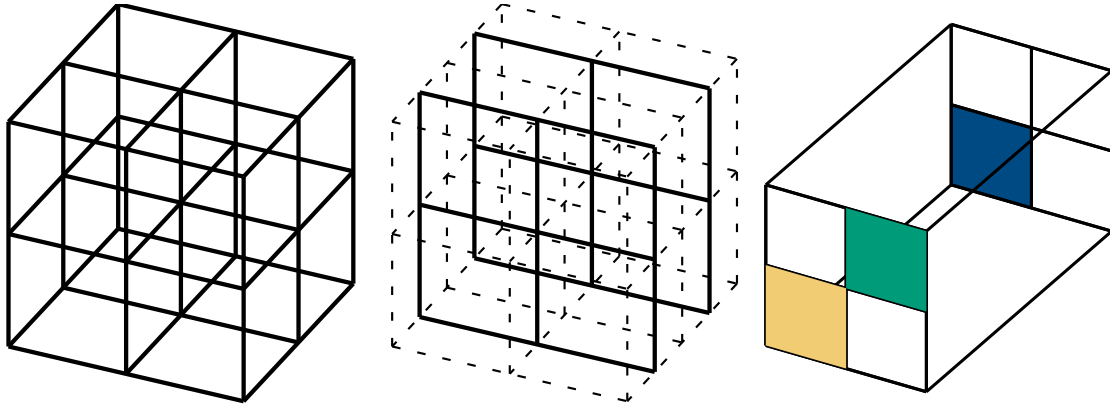- Rotating the Hilbert space such that $x \rightarrow z$.

19

Figure 4.4: Visualization of excitations in Haah's code. Elementary excitations correspond to flipped eigenvalues of $\hat{A}_c$ and $\hat{B}_c$ operators. Instead of drawing the whole lattice in three dimensions like shown on the left, we draw xy-planes intersecting the center of the cubes and rescale the z-axis such that the planes do not overlap anymore. Each square then represents a cube. We visualize a flipped eigenvalue of an $\hat{A}_c$ operator by coloring the corresponding square yellow. For a flipped $\hat{B}_c$ eigenvalue we color the square blue. If both the $\hat{A}_c$ and the $\hat{B}_c$ eigenvalues are flipped we color the square green.

Following similar steps, we can map $\hat{A}_c$ to $\hat{B}_c$ [31]. This symmetry is extremely useful as it allows us in many cases to investigate just one of the operator types and we can deduce the properties of the other one from that. Additionally, Haah's code has a three-fold rotational symmetry around the $(1,1,1)^T$-axis. Note that, none of these symmetries were required in the construction of the model.

In chapter 3.6, we introduced the idea of fractons and stated that Haah's code realizes type-II fracton order. That means that the elementary excitations are immobile and sit at the corners of fractal operators. We will illustrate this by taking a look at both action of a $\hat{B}_c$ operator on the σ spins and on the μ spins. In figure 4.5, one can see that the action of $\hat{B}_c$ on both spins is a Sierpinski tetrahedron with a self similar character. Therefore, $\hat{B}_c$ is a fractal operator. This is also true for the $\hat{A}_c$ operator because of the above mentioned relation between $\hat{A}_c$ and $\hat{B}_c$.

We also want to illustrate that the elementary excitations are immobile. Elementary excitations in Haah's code correspond to a flipped eigenvalue of an $\hat{A}_c$ or $\hat{B}_c$ operator. The excitation of an elementary excitation requires a energy of $2J$, hence Haah's code is gapped. In figure 4.6, we start from an elementary $\hat{B}_c$ excitation and try to move it using single-site $\hat{\mu}^z$ operators. We find that trying to move the excitations always creates three new excitations in the first step. Any additional action either creates even more excitations or separates the excitation further from each other. Therefore, moving a single excitation is impossible without creating additional excitations. The further we want to move a single excitations, the more elementary excitations are created - at least in an intermediate steps.

Doing the same for single-site $\hat{\sigma}^z$ operators yields a similar picture.

We have a similar situation for composites of two particles. We find that acting with a sequence of $\hat{\sigma}^z_i$ or $\hat{\mu}^z_i$ either creates more excitations or separates excitations from each other for the vast majority of configurations. However, there are three case, where three two-particles configurations can be transformed into each other
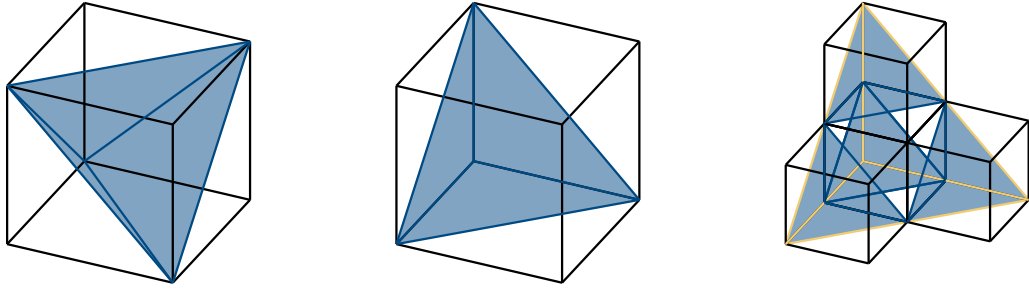
Figure 4.5: Illustration of the fractal character of the operators in Haah's code. The action of a single $\hat{B}_c$ operator on the σ spins is geometrically a tetrahedron. This shown on the left side. The figure in the center shows the action of a single $\hat{B}_c$ operator on the μ, again, forming a tetrahedron. The fractal character can be seen when putting four tetrahedrons together. These form a larger version of the same tetrahedron in a self-similar way, which is shown on the right.
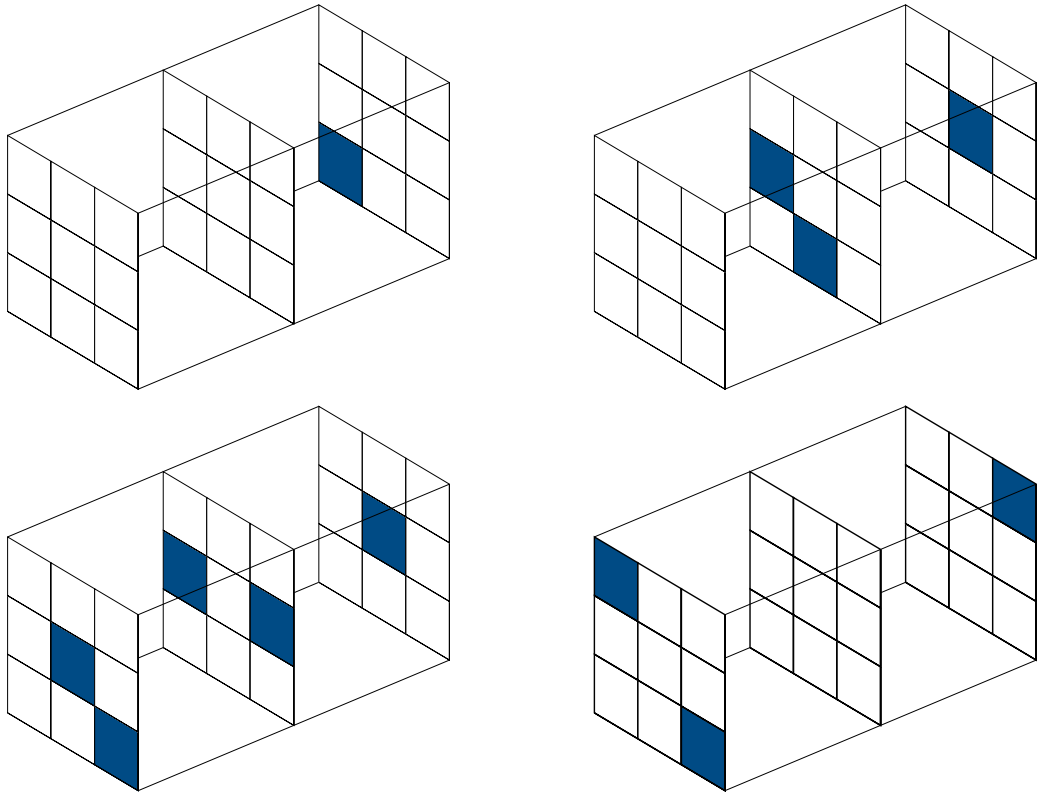

Figure 4.6: Illustration of the immobility of elementary excitations in Haah's code. We start from a elementary $\hat{B}_c$ excitation shown in the top left. If the excitation was mobile, we could reach a state with a single excitation located at the center of another cube by acting with the some perturbation on the spins. We restrict ourselves in this case to flipping of the μ spin. We find that the only option to flip the eigenvalue of the original excitation it to create three new excitations. This is shown on the top-right. Iterating this we either create more excitations like in the bottom left or move the three excitations from the top right further away from each other, which can be seen in the bottom right.
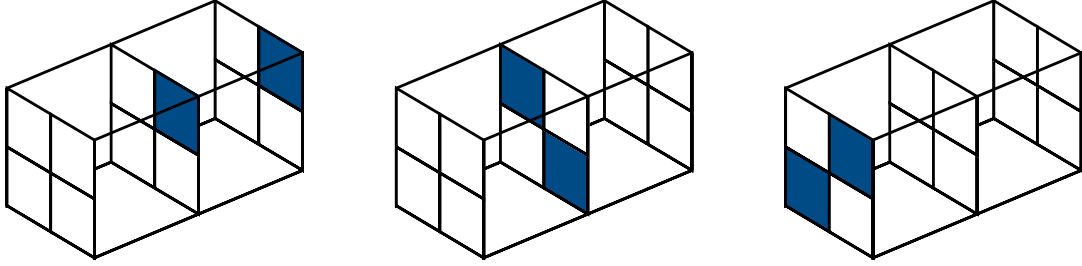
Figure 4.7: Hopping processes for elementary excitations of a $\hat{B}_c$ operator. The configuration in the center can be mapped to the configuration on the left by the action of a $\hat{\mu}_i^z$ operator on the spin in the center of the upper $2 \times 2 \times 2$ cube and vise versa. The configuration on the right can is transformed to the configuration in the center by the action of a $\hat{\sigma}_i^z$ operator on the spin in the center of the upper $2 \times 2 \times 2$ cube and vise versa.

One of these three cases is illustrated in figure 4.7. The configuration in the center can be mapped to the configuration on the left by the action of a $\hat{\mu}^z$ operator on the spin in the center of the $2 \times 2 \times 2$ cube formed by the center and right plane. The inverse process is also possible. Similarly, the configuration on the right can be transformed into the configuration in the center by the action of a $\hat{\sigma}^z$ operator on the spin in the center of the $2 \times 2 \times 2$ cube formed by the plane on the left and in the center. In the following we will call these processes hopping terms. Acting with a different Pauli-z operator on any other site gives the same phenomenology than for the case with a single excitation. That means that these actions either separate the elementary excitations or create additional ones. When considering either $\hat{\sigma}^z$ or $\hat{\mu}^z$ only one of the above hopping processes is possible. Note that the other two cases are identical to the illustrated one up to a rotation of $120°$ or $240°$ around the symmetry axis of the three-fold rotational symmetry.

We also want to mention that for configurations with three and four particles additional three- and four-particle hopping processes arise. These require intermediate states and are all happening locally.

4.5 Haah's code in a homogeneous magnetic field

In this section we introduce the central object of this thesis: Haah's code in a homogeneous magnetic field. The Hamiltonian of Haah's code in the presence of a homogeneous magnetic field pointing in an arbitrary direction reads

$$\hat{\mathcal{H}} = -J \sum_c \hat{A}_c - J \sum_c \hat{B}_c - \sum_i \left(h_\sigma \hat{\sigma}_i + h_\mu \hat{\mu}_i \right),$$

where h_σ, h_μ, σ_p, and μ_p are vectors representing all possible field directions. From now on, we will call h_σ the σ-field and h_μ the μ-field.

The two limiting cases for Haah's code in a homogeneous magnetic field are

- **Low-field limit**: In the so called low-field limit with $J \gg |h_\sigma|$ and $J \gg |h_\mu|$ the coupling between the spins is much stronger than the magnetic field. Therefore, the system will realize the topological fracton phase described in section 4.2.

- **High-field limit**: In the high-field limit with $J \ll |h_\sigma|$ and $J \ll |h_\mu|$ the magnetic field is much stronger than the coupling between spins. That implies that the spins will be aligned along the field direction. We call this state the trivial or polarized state.

As these two phases have very different properties, there has to be at least one phase transition between these cases. We want to investigate the nature of this phase transition for different field directions. In the next chapter we introduce the methods used.

Chapter 5

Methods

Generally, in solid-state physics, we have a good understanding of the properties of the system at high temperatures. The behavior of a macroscopic number of particles can easily be understood as the statistical properties of many individual entities. This changes when going to low temperatures. The quantum properties of individual excitations become more important and lead to new and interesting collective quantum phenomena. In order identify and describe these, we want to solve Schrödinger's equation by diagonalizing the Hamiltonian of the system and look for the lowest eigenvalues and eigenstates. Doing this analytically is only possible for a small number of problems and straight forward numerical methods are often only capable of solving problems with few contributing particles.

In this chapter, we introduce two approaches to such complicated problems. The first is the method of perturbative continuous unitary transformation (pCUT), which solves the so called flow equation perturbatively. The aim of pCUT is establishing a quasi-particle picture on the operator level in a perturbative manner. In this thesis, this will be applied to fractons and spin flip excitations. As a result, we get expressions for the low temperature energies ϵ or the dispersion $\omega(\mathbf{k})$ in the form of power series. In order to investigate the convergence of these series we introduce the Padé approximations. The second tool is a mean field approach that gives more qualitative insights and is mainly used to double check results obtained by pCUT.

5.1 Perturbative continuous unitary transformation

Diagonalizing the Hamiltonian is an unitary transformation. However, finding this transformation directly is usually extremely complicated. Motivated by this difficulty Wegner introduced a new ansatz called continuous unitary transformation (CUT) [32].

5.1.1 Continuous Unitary transformation

We start from the initial Hamiltonian $\hat{\mathcal{H}}$ that has both diagonal and off-diagonal elements. The goal is to transform $\hat{\mathcal{H}}$ to a more diagonal effective Hamiltonian $\hat{\mathcal{H}}_{\text{eff}}$. As we do not want to change the eigenvalues that correspond to the energies of $\hat{\mathcal{H}}$, this transformation $\hat{U}$ has to be unitary. Therefore, we can write

$$\hat{\mathcal{H}}_{\text{eff}} = \hat{U}\hat{\mathcal{H}}\hat{U}^{\dagger}. \tag{5.1}$$

However, finding $\hat{U}$ directly is challenging. Wegner [32] instead proposed constructing $\hat{U}$ continuously using a the flow parameter l such that

$$\hat{\mathcal{H}}(l) = \hat{U}(l)\hat{\mathcal{H}}(0)\hat{U}^\dagger(l), \tag{5.2}$$

with $\hat{\mathcal{H}}(0) = \hat{\mathcal{H}}$ and $\hat{\mathcal{H}}(\infty) = \hat{\mathcal{H}}_{\text{eff}}$. Up to this point, $\hat{U}$ is an arbitrary unitary transformation. However, by forming the derivative of equation (5.1) with respect to l we find the so called flow equation

$$\frac{\mathrm{d}\hat{\mathcal{H}}(l)}{\mathrm{d}l} = \left[\hat{\eta}(l), \hat{\mathcal{H}}_l\right]. \tag{5.3}$$

where $\hat{\eta}(l)$ is the anti-hermitian, infinitesimal generator of the unitary transformation.

As $\hat{U}(l)$ is arbitrary, the next step is to choose the generator such that the elements far from the diagonal vanish in the limit $l \to \infty$. The generator Wegner initially chose is $\eta_{ij} = (h_{ii} - h_{jj})h_{ij}$ where h_{ij} denotes the matrix elements of the Hamiltonian. This choice makes sure that all off-diagonal elements vanish for large l. However, as pointed out by Knetter and Uhrig in [33], this results in a complicate form of the differential equations for models that have an initially block-diagonal nature. Knetter and Uhrig instead introduce a different generator that applied to certain problems allows for a very efficient, perturbative solution.

5.1.2 Quasi-particle conservation

The method of perturbative continuous unitary transformation (pCUT) transforms the Hamiltonian such that it becomes quasi-particle conserving. In this chapter we explain how a quasi-particle is defined and which quasi-particles will be considered in this thesis.

Consider a few positively changed ions in a sea of electrons. Due to their charges, an ion attracts a cloud of electrons. When the ions moves the electrons are dragged along for some while until fall off due to collisions and are replaced by other electrons. The composite of the ion and the electron cloud is still largely defined by the properties of the ion, but the electrons for example shield the charge of the ion. A particle together with a polarization cloud, or sometimes also called clothes, is called a quasi-particle or a dressed particle. [34]

We use this concept in this thesis for fractons in the topological phase and spin-flips in the polarized phase. The fractons in the unperturbed Hamiltonian are particles. If we introduce a magnetic field, we mix these particles which dresses them. The quasi-particles emerging from that mixing are still characterized by the same quantum numbers as the original particles, but have different properties due to the dressing. With pCUT, we extract the ground-state energies and the energies of the one- and two-particle block.

5.1.3 Perturbative continuous unitary transformation

The idea of pCUT is to transform the Hamiltonian into a block diagonal form, where each block corresponds to a fixed number of quasi-particles. Conversely, the effective Hamiltonian must be quasi-particle conserving [33]. This is illustrated in figure 5.1. pCUT offers an efficient perturbative solution for systems that fulfill the following constraints

1. The spectrum of the unperturbed Hamiltonian $\hat{\mathcal{H}}$ is equidistant and bounded from below. That means that $\hat{\mathcal{H}}_0$ can be written up to a constant as the (quasi) particle number operator $\hat{Q}$
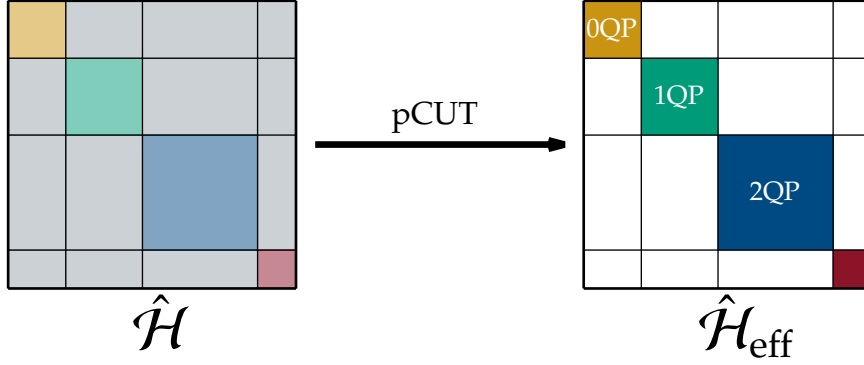
Figure 5.1: pCUT transforms a complicated non-diagonal Hamiltonian $\hat{\mathcal{H}}$ into a block diagonal effective Hamiltonian $\hat{\mathcal{H}}_{\text{eff}}$, where each block corresponds to a regime with constant number of quasi-particles. The yellow block on the right is zero quasi-particle block, the green one the one quasi-particle block and the blue the two quasi-particle block.

2. There exists a number $N \in \mathbb{N}$ such that the perturbation can be written as

$$\hat{V} = \sum_{m=-N}^{m=N} \hat{T}_m, \tag{5.4}$$

where we introduce the operators $\hat{T}_m = \hat{T}^\dagger_{-m}$ that create and annihilate quasi-particles. If m is positive the operator creates m quasi-particles and if m is negative it annihilates $|m|$ quasi-particles. Hence, the action on a state $|n\rangle$ with n quasi-particles is

$$\hat{T}_m |n\rangle = \begin{cases} |n+m\rangle & \text{for } m+n \geq 0, \\ 0 & \text{for } m+n < 0. \end{cases} \tag{5.5}$$

Note that, $\hat{T}_m$ includes all possible actions that change the particle number by m. For example, if we consider a translationally invariant lattice, we often have local operators $\hat{\tau}_{m,i}$ on each lattice site i changing the particle number by m. $\hat{T}_m$ is the sum of all $\hat{\tau}_{m,i}$. Hence, $\hat{T}_m = \sum_i \hat{\tau}_{m,i}$.

Knetter and Uhrig introduced the generator $\eta_{ij}(l) = \text{sgn}(q_{ii} - q_{jj})h_{ij}(l)$, where q_{ij} is the number of quasi-particles in the matrix element in the eigenbasis of $\hat{Q}$. One can see that η_{ij} vanishes if the number of quasi-particles in each block is constant. Using this generator and following the steps in [33], one can derive the model independent effective Hamiltonian

$$\hat{\mathcal{H}}_{\text{eff}} = \hat{Q} + \sum_{\lambda=k}^{\infty} \lambda^k \sum_{\substack{|\mathbf{m}|=k, \\ M(\mathbf{m})=0}} C(\mathbf{m})\hat{T}(\mathbf{m}), \tag{5.6}$$

27

where $\mathbf{m} = (m_1, m_2, ..., m_k)$ a tuple of numbers, $|\mathbf{m}|$ is the number of elements in the tuple and $M(\mathbf{m}) = \sum_i m_i$. $\hat{T}(\mathbf{m}) = \prod_i \hat{T}_{m_i}$ is a sequence of $\hat{T}$ operators. Each $\hat{T}(\mathbf{m})$ leaves the number of quasi-particles unchanged, as $M(\mathbf{m}) = 0$. Hence, the whole effective Hamiltonian is quasi-particle conserving, which was the aim of the derivation. $C(\mathbf{m})$ are model independent coefficients. Therefore, these have to be computed once by solving a set of coupled differential equations and can then be used for all problems with the same $\hat{T}$ operators. A scheme to compute the coefficients with computer aid is presented in [35]. The model dependent part of pCUT is to efficiently normal-order $\hat{\mathcal{H}}_{\text{eff}}$ in order to extract the relevant low-energy properties. This is most efficiently done by evaluating $\hat{\mathcal{H}}_{\text{eff}}$ on finite clusters making use of the linked cluster theorem.

5.1.4 Linked-cluster theorem

The fact that the linked-cluster theorem can be applied to pCUT is a key property of the method. The way of understanding this presented here is taken from [36]. Due to the perturbative nature of the approach, $\hat{\mathcal{H}}_{\text{eff}}$ can be written as infinite sum of weighted, nested commutators of $\hat{T}_n$ operators. The $\hat{T}_n$ operators themselves can be written as a sum of operators $\hat{\tau}_{n,\nu_1,..\nu_n}$ acting on a local set of sites $\nu_1, ..\nu_n$. Naturally, a pair of $\hat{\tau}_{n,\nu_1,..\nu_n}$ operators commutes if they act on spatially disconnected sites. Therefore, only summands with connected $\hat{\tau}_{n,\nu_1,..\nu_n}$ have a non-zero contribution to $\hat{\mathcal{H}}_{\text{eff}}$. An alternative approach making use of the so called cluster additivity can be found in [35].

As a consequence, one can efficiently normal-order $\hat{\mathcal{H}}_{\text{eff}}$ by evaluating it on a finite cluster that is large enough to include all possible linked processes in the highest considered order. This makes a computer aided evaluation possible, that systematically tries all options to act with a $\hat{T}$ operator sequence. Without the linked-cluster theorem, a computer must store the whole infinite lattice, which is not possible. A scheme how to implement the action of a $\hat{T}$ operator sequence is presented in [35]. As a computer aided evaluation tries to act with all local $\hat{\tau}_n$ in the cluster for each $\hat{T}_n$ operator in the sequence, the computational cost grows exponentially with the size of the cluster. In the next section we introduce the approach we chose to minimize the clusters.

5.1.5 Cluster optimization

For the cluster optimization, we want to find the minimal cluster that still incorporates all linked processes in the considered order. All the $\hat{T}$ operators for Haah's code act locally. This is discussed in more detail in section 6.4. The fact that $\hat{T}$ operators act locally, implies that single $\hat{T}$ operators can only link neighboring sites. Hence, two sites that are n sites away from each other in one direction can only be linked by $\hat{T}$ operator sequences that are at least n operators long. We use this to construct the minimal clusters for the evaluation of the pCUT. However, we have to make a distinction between the ground-state energies, i.e. the zero quasi-particle sector, and all other quasi-particle sectors, which we will call multi quasi-particle sectors. We start with the latter.

Multi quasi-particle sector

For the multi quasi-particle sector, we take two states $|A\rangle$ and $|B\rangle$ with a certain equivalent number of quasi-particles and evaluate expressions like

$$\langle A| \hat{\mathcal{H}}_{\text{eff}} |B\rangle .$$
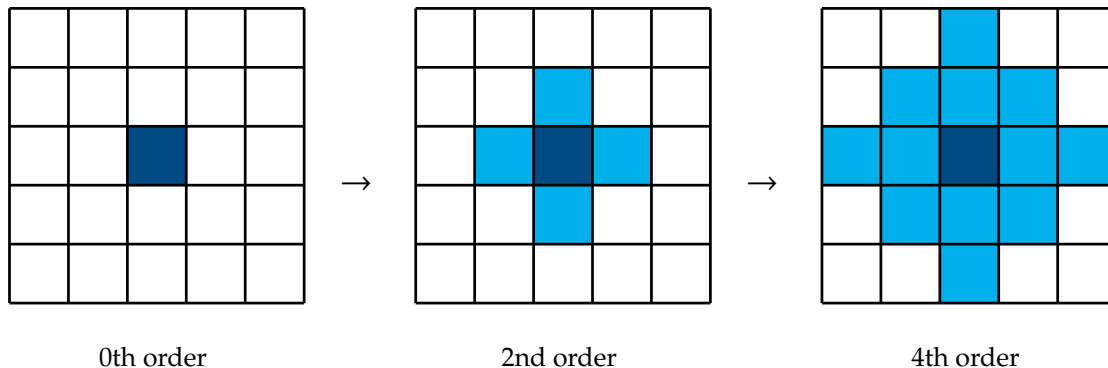
Again, we have different cases.

Figure 5.2: Example of the construction of the optimal cluster for a diagonal matrix element in the one quasi-particle block on a square lattice. In this example we consider $\hat{T}$ operators that link two squares that are direct neighbors. The initial excitation is indicated in dark blue. The starting cluster consists of the initial excitations. This cluster is shown on the left. For the second order all sites that can be reached from the starting cluster by a single $\hat{T}$ operator are added to the cluster. This is indicated in bright blue in the center picture. This is iterated for the fourth order in the right picture.

For diagonal elements, i.e. $|B\rangle = |A\rangle$, only those $\hat{T}$ operator sequences contribute that return to the same state. Consider two sites s and s'. s is one of the initial excitations in $|A\rangle$ and s' is an unoccupied site at a distance d in one direction. s' can only be in the cluster if we can find a $\hat{T}$ operator sequence that creates a quasi-particle at s' starting from s. If we find such a sequence, we create many additional quasi-particles or separate quasi-particles from each other due to the fractal character of the operators in Haah's code. As we are calculating diagonal elements, we need to get back to the original state. But again, due to the fractal character of the $\hat{T}$ operators the only option to get back is to act with $\hat{T}$ operators at the same sites then in the original sequence. Note that, the order and the number of created and annihilated quasi-particles for these $\hat{T}$ operators might be different, but they have to act on the very same sites. Conversely, in order k, a site s' that cannot be reached a sequence of $k/2$ $\hat{T}$ operators cannot be part of a linked process, because can not go back to the original state with the remaining $\hat{T}$ operators. Hence, we construct the minimal cluster for the diagonal elements as follows. Start from a cluster that consists of the sites containing the initial excitation. Then iteratively add all sites to the cluster that can be reached from the cluster in the previous step with one $\hat{T}$ operator. Repeat this for $k/2$ steps in order k. An example for such a process in shown in figure 5.2.

For off-diagonal elements, e.i. $|B\rangle \neq |A\rangle$, we can follow a similar approach. However, the initial cluster and the number of iterations is different. If an off-diagonal element has a non-zero contribution, there has to be at least one $\hat{T}$ operator sequence that maps $|A\rangle$ to $|B\rangle$. Let S be the set of the shortest of these sequences. All of those have a certain length l. The initial cluster is the cluster that includes the sites with the initial excitations from $|A\rangle$ and $|B\rangle$ and all sites are touched by any of these sequences in S. For the optimization, we do the same iteration as above for $\frac{k-l}{2}$ steps. An example for such a process in shown in figure 5.3.
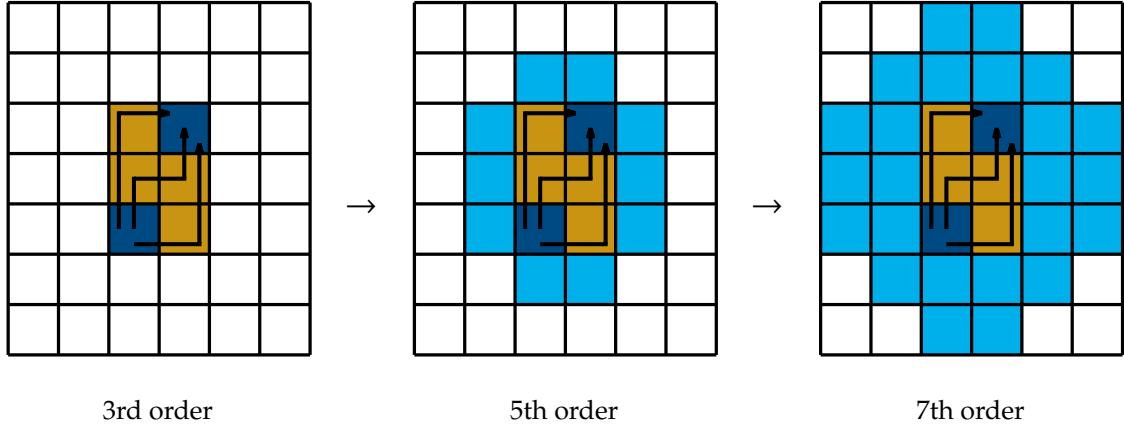
29

| 3rd order | 5th order | 7th order |

Figure 5.3: Example for the construction of the optimal cluster for a off-diagonal matrix element in the one quasi-particle block on a square lattice. In this example we consider $\hat{T}$ operators that link two squares that are direct neighbors. The initial and final excitations are indicated in dark blue. There are three processes containing three $\hat{T}$ operators connecting the two initial excitations. These are indicated by the arrows. The starting cluster consists of the initial excitations and all sites touched by one of the processes indicated in yellow. This cluster is already the optimal cluster in 3rd order. For the 5th order all site that can be reached from the starting cluster by a single $\hat{T}$ operator are added to the cluster. This is indicated in bright blue in the center picture. The iteration for the 7th order is shown in the right picture.

Ground-state energies

If we calculate ground-state energies, we do not have a special set of sites that we can use as starting point of the optimal cluster. For the ground-state energies all sites are equal. Hence, we have to make sure that the surrounding of each site in the cluster is the same. For a finite lattice we can achieve this with periodic boundary conditions. We have to make this lattice large enough such that no processes contribute, that are linked process via the periodic boundary. Practically, we start with a cubic lattice thats linear sizes is larger than the highest order. For the optimal we start from a random initial site. Then we add iteratively all sites that can be reached from the cluster in the previous step with one $\hat{T}$ operator. We stop when in one iteration no new sites are to be added to the cluster. We use this approach in chapter 7, where we also illustrate an example in figure 7.3.

5.1.6 Graph expansion

For completeness, we want to mention that the efficiency of pCUT calculations can further be enhanced by a graph expansion or a white graph expansions. The idea of the graph expansion is to perform a cluster decomposition of the lattice and evaluate $\hat{\mathcal{H}}_{\text{eff}}$ for smaller clusters. Finally, subclusters are embedded in the whole lattice and their contributions are added up according to the number of possible embeddings. This way, the computational expensive evaluation of $\hat{\mathcal{H}}_{\text{eff}}$ can be done on significantly smaller clusters. A white graph expansion can reduce the complexity of problems with many bond types [37]. However, a graph or white graph expansion was not done in this thesis.

5.2 Padé approximation

As mentioned, the results for the energies or the dispersion obtained by pCUT are power series. Mathematically, one can interpret this series as a Taylor series approximating a function $f(\lambda)$ around $\lambda = 0$. Due to the fact that increasingly higher orders become more and more computational expensive, we have to truncate the series at some point. While power series are a good approximation for small λ, they diverges for large λ. As we are interested in quantum phase transitions that might occur for large values of λ, this can be a problem. We can increase the convergence radius of the series by Padé approximations.

Instead of the best power series approximation a function $f(\lambda)$ at $\lambda = 0$, a Padé approximation is the best approximation of $f(\lambda)$ using rational functions. Given a pair of integer numbers L and M the Padé approximation of order $[L/M]$ is defined as

$$P[L/M](\lambda) = \frac{\sum_{l=1}^{L} a_l \lambda^l}{1 + \sum_{m=1}^{M} b_m \lambda^m} = \frac{a_1 \lambda + a_2 x \lambda^2 + ... + a_l \lambda^L}{1 + b_1 \lambda + b_2 \lambda^2 + ... + b_M \lambda^M}, \quad (5.7)$$

where the first $L + M$ derivatives of $f(\lambda)$ and $P[L/M](\lambda)$ at $\lambda = 0$ are identical. Hence,

$$\begin{aligned}
f^{(0)}(\lambda = 0) &= P[L/M]^{(0)}(\lambda = 0) \\
f^{(1)}(\lambda = 0) &= P[L/M]^{(1)}(\lambda = 0) \\
f^{(2)}(\lambda = 0) &= P[L/M]^{(2)}(\lambda = 0) \\
&\vdots \\
f^{(L+M)}(\lambda = 0) &= P[L/M]^{(L+M)}(\lambda = 0).
\end{aligned}$$

Given a Taylor expansion up to Nth order with coefficients c_n, one can derive a set of linear equations for the coefficients a_l and b_m of a Padé approximation of order $[L/M]$ with $L + M \leq N$ [38]. Due to the rational nature of the Padé approximations, approximants of order $[L, M]$ with $M > L$ do not diverge. More importantly, these Padé approximations can be used to get more insight to the convergence of the original series. The idea is treat the power series from pCUT as a Taylor expansion and to calculate all possible Padé approximations for a given order. Then, we compare the approximants and thus have a measure for the convergence of the series [39].

However, there are a few caveats. First, the linear set of equations has no solution for some Padé approximations. Among the ones with a solution, some have pole in the relevant regime. Hence, we will not consider these. Second, the Padé approximants where the order of the numerator and the order of the dominator are close are considered to be better approximations than those, were these orders differ dramatically [39]. Therefore, we will for example not include Padé approximants of order $[1/5]$ in order 6. Lastly, we can also calculate Padé approximants for lower orders than the order of the original series. This make only sense within a certain region [39]. That means that we will not include Padé approximants thats orderis more than two to three orders lower than the original series.

5.3 Variational ansatz

In section 4.5, we introduced Haah's code in a homogeneous magnetic field which is the central object of the thesis. One approximate approach to locate quantum phase transitions is to use a

variational ansatz containing both limits exactly. In the past, this has been exploited successfully for two-dimensional and three-dimensional topological order in [40, 41].

The ground state in the high-field limit is the state where all spins are polarized in the direction of the magnetic field. We denote this state for an arbitrary h_σ and h_μ with $|h\rangle$. The ground state for the low-field limit can be written with using projectors as in equation 4.4. Here we will write the ground state as

$$|0\rangle = \prod_c \frac{(\mathbb{1} + \hat{A}_c)}{2} \prod_c \frac{(\mathbb{1} + \hat{B}_c)}{2} |h\rangle$$

provided that $|h\rangle$ is not orthogonal to the ground state.

The idea of the variational ansatz introduced in [40] is to define a state $|\alpha, \beta\rangle$ that can be tuned between the exact low- and high-field ground state using two variational parameters α and β. This state reads

$$|\alpha, \beta\rangle = \mathcal{N} \prod_c (\mathbb{1} + \alpha \hat{A}_c) \prod_c (\mathbb{1} + \beta \hat{B}_c) |h\rangle \,, \tag{5.8}$$

where $\mathcal{N}$ is a normalization factor depending on α and β. By setting $\alpha = \beta = 0$ one is back at the polarized state $|h\rangle$ and for $\alpha = \beta = 1$ one recovers the topological fracton phase $|0\rangle$.

We can use this state to calculate the energy as a function of α and β by evaluating

$$E(\alpha, \beta) = \langle \alpha, \beta | \hat{\mathcal{H}} | \alpha, \beta \rangle \,.$$

Finally, we can minimize $E(\alpha, \beta)$ with respect to α and β for different magnetic fields h and track the energy of the minimum to get an idea of the nature of the phase transition.

Chapter 6

Breakdown of the fracton phase

We consider three cases

- In the *single-field case*, where h_σ or h_μ is zero and the other field points in either x- or z-direction.

- In the *two-field case $h_\sigma = h_\mu \neq 0$* and point in the same direction. Again, we consider fields pointing in x- or z-direction.

- In the *mixed-field case h_σ* and h_μ are nonzero, but one of them points in x-direction and the other one in z-direction.

In this chapter, we start by structuring the above cases. We find that these cases are related and we can get the results for all of them by considering a general homogeneous magnetic field pointing in z-direction. As a next step, we make the variational ansatz for this general homogeneous magnetic field in z-direction and calculate the ground-state energy as a function of the amplitudes of the magnetic fields $h_{\sigma,z}$ and $h_{\mu,z}$. We introduce hardcore bosons for both the high- and the low-field limit and bring both cases in the form required for pCUT. Finally, we will also show that the single-field case is self-dual. In the next two chapters, we take these general results and determine the nature of the phase transitions.

6.1   Relations between the cases

In section 4.4, we already established that the $\hat{A}_c$ and $\hat{B}_c$ operators can be mapped to each other by inverting the lattice and renaming σ to μ and vice versa. We will make use of that in order to relate the different options for the above cases to each other.

For the single-field and the two-field case, we have two options to choose the orientation of the magnetic field

$$\hat{\mathcal{H}} = -J \sum_c \hat{A}_c - J \sum_c \hat{B}_c - \sum_i \left(h_{\sigma,z} \cdot \hat{\sigma}_i^z + h_{\mu,z} \cdot \hat{\mu}_i^z \right), \tag{6.1}$$

$$\hat{\mathcal{H}} = -J \sum_c \hat{A}_c - J \sum_c \hat{B}_c - \sum_i \left(h_{\sigma,x} \cdot \hat{\sigma}_i^x + h_{\mu,x} \cdot \hat{\mu}_i^x \right). \tag{6.2}$$

As $\hat{A}_c$ is a product of Pauli z operators, it commutes with the perturbation in equation 6.1. Hence, the energy correction is due to the action of the $\hat{B}_c$ operator on the σ- and μ-spin and vise versa.

For equation 6.2, $\hat{B}_c$ commutes with the perturbation and the energy correction is governed by the action of the $\hat{A}_c$ operators on the σ- and μ-spin and vise versa. However, the action of the $\hat{B}_c$ operator on the σ-spin is up to inversion identical to the action of the $\hat{A}_c$ operator on the μ-spins due to the symmetry of $\hat{A}_c$ and $\hat{B}_c$. Similarly, is the action of the $\hat{B}_c$ operator on the μ-spins up to a inversion identical to the action of the $\hat{A}_c$ operator on the σ-spins. This implies that the influence of the magnetic field in both cases yields the same energetics. That means that it is sufficient for the single- and two-field case to just consider the case where the magnetic field points in z-direction.

For the mixed field case, we can choose the orientation of the magnetic field as follows

$$\hat{\mathcal{H}} = -J \sum_c \hat{A}_c - J \sum_c \hat{B}_c - \sum_i \left(h_{\sigma,x} \cdot \hat{\sigma}_i^x + h_{\mu,z} \cdot \hat{\mu}_i^z \right), \tag{6.3}$$

$$\hat{\mathcal{H}} = -J \sum_c \hat{A}_c - J \sum_c \hat{B}_c - \sum_i \left(h_{\sigma,z} \cdot \hat{\sigma}_i^z + h_{\mu,x} \cdot \hat{\mu}_i^x \right). \tag{6.4}$$

There are no direct relations between the two cases. However, we rewrite the Hamiltonians for both cases as follows

$$\hat{\mathcal{H}} = \underbrace{-J \sum_c \hat{A}_c - \sum_i h_{\sigma,x} \cdot \hat{\sigma}_i^x}_{\hat{\mathcal{H}}_{A,\sigma^x}} \underbrace{-J \sum_c \hat{B}_c - h_{\mu,z} \cdot \hat{\mu}_i^z}_{\hat{\mathcal{H}}_{B,\mu^z}}, \tag{6.5}$$

$$\hat{\mathcal{H}} = \underbrace{-J \sum_c \hat{A}_c - \sum_i h_{\mu,x} \cdot \hat{\sigma}_i^x}_{\hat{\mathcal{H}}_{A,\mu^x}} \underbrace{-J \sum_c \hat{B}_c - h_{\mu,z} \cdot \hat{\sigma}_i^z}_{\hat{\mathcal{H}}_{B,\sigma^z}}. \tag{6.6}$$

In equation 6.6, all terms in $\hat{\mathcal{H}}_{A,\mu^x}$ commute with all terms in $\hat{\mathcal{H}}_{B,\sigma^z}$, e.i. $[\hat{A}_c, \hat{B}_{c'}] = 0 \; \forall c, c'$, $[\hat{A}_c, \hat{\sigma}_i^z] = 0 \; \forall c, i$, $[\hat{\mu}_i^x, \hat{B}_c] = 0 \; \forall i, c$ and $[\hat{\mu}_i^x, \hat{\sigma}_j^z] = 0 \; \forall i, j$. That means, we can treat each of the Hamiltonians in equations 6.5 and 6.6 separately. But due to the symmetry of $\hat{A}_c$ and $\hat{B}_c$ both $\hat{\mathcal{H}}_{A,\mu^x}$ and $\hat{\mathcal{H}}_{B,\sigma^z}$ in 6.5 give the same result. Hence, we only have to consider $\hat{\mathcal{H}}_{B,\sigma^z}$ and $\hat{\mathcal{H}}_{B,\mu^z}$ in order to get the full result. Conveniently, these expression are included in the single-field case.

In summary, it is sufficient to calculate the single- and two-field case for a magnetic field pointing in z-direction in order to get results for all the above cases. We will do this, by treating the Hamiltonian in equation 6.1 for arbitrary $h_{\sigma,z}$ and $h_{\mu,z}$ with the variational approach and pCUT. In a next step we set $h_{\sigma,z}$ and $h_{\mu,z}$ to their respective values for the single- and two field case. Finally, we use the results of the single-field case to treat the mixed-field case.

6.2 Reduction of the Hilbert space

We consider the Hamiltonian for a general magnetic field in z-direction (equation 6.1)

$$\hat{\mathcal{H}} = -J \sum_c \hat{A}_c - J \sum_c \hat{B}_c - \sum_i \left(h_{\sigma,z} \cdot \hat{\sigma}_i^z + h_{\mu,z} \cdot \hat{\mu}_i^z \right). \tag{6.7}$$

As $\hat{A}_c$ is a product of four $\hat{\sigma}_i^z$ and four $\hat{\mu}_i^z$ operators, it commutes with the magnetic field. We use this fact to reduce the Hilbert space of the problem by considering only the subspace where all eigenvalues of the $\hat{A}_c$ operators are +1. In principle, it possible that the state with the lowest energy is in another subspace, but due the high cost of creating an $\hat{A}_c$ excitation and our interest

in the low energy physics, this reduction of the problem yields the correct result. Using this equation 6.7 becomes

$$\hat{\mathcal{H}} = -JN_c - J\sum_c \hat{B}_c - \sum_i \left(h_{\sigma,z} \cdot \hat{\sigma}_i^z + h_{\mu,z} \cdot \hat{\mu}_i^z \right).$$

The ground state can also be simplified. In equation 4.4, the ground state is given by projectors. As all $\hat{A}_c$ operators commute with all $\hat{B}_c$ operators and act trivially on the state with all spins pointing in z-direction, we can reduce this to

$$|0\rangle = \prod_c \left(\frac{\mathbb{1} + \hat{B}_c}{2} \right) |\Uparrow\rangle. \tag{6.8}$$

We use the simplification of both the Hamiltonian and the ground state in the following for the variational ansatz and pCUT.

6.3 Variational ansatz for a homogeneous magnetic field in z-direction

Because all eigenvalues of the $\hat{A}_c$ operator are +1, we can set α to 1 in equation 5.8. This yields

$$|\beta\rangle = |\alpha = 1, \beta\rangle = \mathcal{N} \prod_c (\mathbb{1} + \beta\hat{B}_c) |\Uparrow\rangle, \tag{6.9}$$

where $|\Uparrow\rangle$ is the state with all spins pointing into z-direction.

We now calculate the mean energy per site of the system in state $|\beta\rangle$ as a function of $h_{\sigma,z}$, $h_{\mu,z}$ and J step by step.

Normalization

As a first step, we have to normalize $|\beta\rangle$:

$$
\begin{aligned}
\langle\beta|\beta\rangle &= \langle\Uparrow| \mathcal{N}^2 \prod_c \left(\mathbb{1} + \beta\hat{B}_c \right)^2 |\Uparrow\rangle = \\
&= \langle\Uparrow| \mathcal{N}^2 \prod_c \left(\mathbb{1} + 2\beta\hat{B}_c + \beta^2\hat{B}_c^2 \right) |\Uparrow\rangle = \\
&= \langle\Uparrow| \mathcal{N}^2 \prod_c (1 + \beta^2) \left(\mathbb{1} + \frac{2\beta}{1 + \beta^2}\hat{B}_c \right) |\Uparrow\rangle
\end{aligned}
$$

where we used $\hat{B}_c^2 = \mathbb{1}$ in the last line. $\hat{B}_c$ is a product of σ^x and μ^x operators that flip spins in an eigenstate of σ^z. Additionally, the spin flips caused by a $\hat{B}_c$ operator cannot be compensated by the action of a combination of other $\hat{B}_c$ operators due to open boundary conditions. Therefore, the only term contributing is the one proportional to $\mathbb{1}$. Using this, we can conclude that $|\beta\rangle$ is normalized for

$$1 = \langle\beta|\beta\rangle = \mathcal{N}^2(1 + \beta)^{N_c}, \tag{6.10}$$

where N_c is the number of cubes in the system.

Calculation of the energy per site

In order to calculate $\langle \beta | \hat{\mathcal{H}} | \beta \rangle$ we consider all contributing terms individually and gather the results in the end.

Calculation of $\left\langle \hat{B}_c \right\rangle_\beta$

We start by inserting the definition for $\langle \beta |$, which yields

$$\left\langle \hat{B}_c \right\rangle_\beta = \langle \Uparrow | \left(\mathcal{N} \prod_{c'} \mathbb{1} + \beta \hat{B}_{c'} \right) \hat{B}_c \left(\mathcal{N} \prod_{c'} \mathbb{1} + \beta \hat{B}_{c'} \right) | \Uparrow \rangle .$$

We now separate the terms with $c' \neq c$ from the terms including $\hat{B}_c$

$$
\begin{aligned}
\left\langle \hat{B}_c \right\rangle_\beta &= \langle \Uparrow | \mathcal{N}^2 \prod_{c' \neq c} \left(\mathbb{1} + \beta \hat{B}_{c'} \right)^2 \cdot \hat{B}_c \left(\mathbb{1} + \beta \hat{B}_c \right)^2 | \Uparrow \rangle \\
&= \langle \Uparrow | \mathcal{N}^2 \prod_{c' \neq c} \left(\mathbb{1} + 2\beta \hat{B}_{c'} + \beta^2 \hat{B}_{c'}^2 \right) \cdot \hat{B}_c \left(\mathbb{1} + 2\beta \hat{B}_c + \beta^2 \hat{B}_c^2 \right) | \Uparrow \rangle \\
&= \langle \Uparrow | (1 + \beta^2)^{N_c} \mathcal{N}^2 \prod_{c' \neq c} \left(\mathbb{1} + \frac{2\beta}{1 + \beta^2} \hat{B}_{c'} \right) \cdot \left(\hat{B}_c + \frac{2\beta}{1 + \beta^2} \mathbb{1} \right) | \Uparrow \rangle .
\end{aligned}
$$

Analogous to the normalization, only the terms proportional to $\mathbb{1}$ have a non-zero contribution and hence

$$\left\langle \hat{B}_v \right\rangle_\beta = \mathcal{N}^2 (1 + \beta^2)^{N_c} \frac{2\beta}{1 + \beta^2} = \frac{2\beta}{1 + \beta^2},$$

where we used the normalization derived in equation 6.10.

Calculation of $\langle \hat{\sigma}_c^z \rangle_\beta$ and $\langle \hat{\mu}_c^z \rangle_\beta$

The main difference compared to the last part is that we now have to consider anti-commutation rules for Pauli operators instead of the commutation rules for the stabilizer operators. We start by

$$\left\langle \hat{\sigma}_p^z \right\rangle_\beta = \langle \Uparrow | \mathcal{N}^2 \prod_c \left(\mathbb{1} + \beta \hat{B}_{c'} \right) \hat{\sigma}_p^z \prod_c \left(\mathbb{1} + \beta \hat{B}_{c'} \right) | \Uparrow \rangle$$

Since $\hat{B}_c$ is a product of $\hat{\sigma}_p^z$, $\hat{\sigma}_p^z$ anti-commutes with the $\hat{B}_c$ where $\hat{\sigma}_p^x \in \hat{B}_c$, but commutes with all others. A $\hat{\sigma}_p^x$ is part of four $\hat{B}_c$ operators. Using that, we rewrite the above equation as follows

$$
\begin{aligned}
\left\langle \hat{\sigma}_p^z \right\rangle_\beta &= \langle \Uparrow | \mathcal{N}^2 \prod_{\hat{\sigma}_p^x \notin \hat{B}_c} \left(\mathbb{1} + \beta \hat{B}_c \right)^2 \prod_{\hat{\sigma}_p^x \in \hat{B}_c} \left((\mathbb{1} + \beta \hat{B}_c)(\mathbb{1} - \beta \hat{B}_c) \right) | \Uparrow \rangle \\
&= \langle \Uparrow | \mathcal{N}^2 \prod_{\hat{\sigma}_p^x \notin \hat{B}_c} \left(\mathbb{1} + \beta \hat{B}_c \right)^2 \prod_{\hat{\sigma}_p^x \in \hat{B}_c} \mathbb{1} \left(1 - \beta^2 \right) | \Uparrow \rangle \\
&= \mathcal{N}^2 (1 + \beta^2)^{N_c - 4} (1 - \beta^2)^4 = \\
&= \left(\frac{1 - \beta^2}{1 + \beta^2} \right)^4
\end{aligned}
$$

The calculation for $\left\langle \hat{\mu}_p^z \right\rangle_\beta$ is analogous and yields the same result.

Energy per site

Gathering all contribution from above we can now calculate the energy per site.

$$
\begin{aligned}
\frac{\langle \mathcal{H} \rangle_\beta}{N_c} &= \frac{1}{N_c} \left[-J \sum_c 1 - J \sum_c \frac{2\beta}{1+\beta^2} - \sum_p \left(h_{\sigma,z} \left(\frac{1-\beta^2}{1+\beta^2} \right)^4 + h_{\mu,z} \left(\frac{1-\beta^2}{1+\beta^2} \right)^4 \right) \right] \\
&= -J \left(1 + \frac{2\beta}{1+\beta^2} \right) - (h_{\sigma,z} + h_{\mu,z}) \left(\frac{1-\beta^2}{1+\beta^2} \right)^4 \\
&= -J \frac{(1+\beta)^2}{1+\beta^2} - (h_{\sigma,z} + h_{\mu,z}) \left(\frac{1-\beta^2}{1+\beta^2} \right)^4 .
\end{aligned}
\tag{6.11}
$$

In order to use the same units than we do for the low-field case pCUT we divide equation 6.11 by $2J$

$$
\epsilon = \frac{\langle \mathcal{H} \rangle_\beta}{2JN_c} = -\frac{1}{2} \frac{(1+\beta)^2}{1+\beta^2} - \frac{1}{2J} (h_{\sigma,z} + h_{\mu,z}) \left(\frac{1-\beta^2}{1+\beta^2} \right)^4 .
\tag{6.12}
$$

6.4   pCUT for a homogeneous magnetic field in *z*-direction

In this section we use pCUT in order to determine the nature of the phase transition. We do perturbation theory in both the low- and the high-field limit. For both cases, we introduce quasi-particles. Using these we can explicitly bring the Hamiltonian in the form required for pCUT. We start with the low-field limit.

6.4.1   Low-field Limit

In the low-field limit, the magnetic field acts as a perturbation on the topological ground state

$$
|0\rangle = \prod_c \frac{(\mathbb{1} + \hat{B}_c)}{2} |\Uparrow\rangle \, ,
$$

where $|\Uparrow\rangle$ is the state with all spins pointing in *z*-direction. Acting with the perturbation flips the eigenvalues of certain $\hat{B}_c$ operators. Instead of implementing the system directly, we consider a so called dual model. It consists of hardcore bosons located at the center of the cubes. The lattice containing these sites is called the dual lattice. These particles have bosonic creation and annihilation operators that represent the eigenvalues of the $\hat{B}_c$ operators. They are called hardcore bosons, because we do not allow more than one particle per cube. An empty site represents $b_c = +1$ and an occupied site $b_c = -1$. Hence,

$$
\begin{aligned}
|b_c = +1\rangle &\; \hat{=} \;\; |0\rangle \\
|b_c = -1\rangle &\; \hat{=} \;\; |1\rangle \, .
\end{aligned}
$$

In that framework, the ground state can be written as $|0 \ldots 0\rangle$. The reason why we can investigate a simpler dual model instead of the original one is that the two models share the same energetics, since the energy depends solely on the presence of fracton excitations. Therefore, the critical behavior shown by investigating the energy of the dual model is the very same than for the original model. Using the above relations we can express the operators in equation 6.2 in terms of
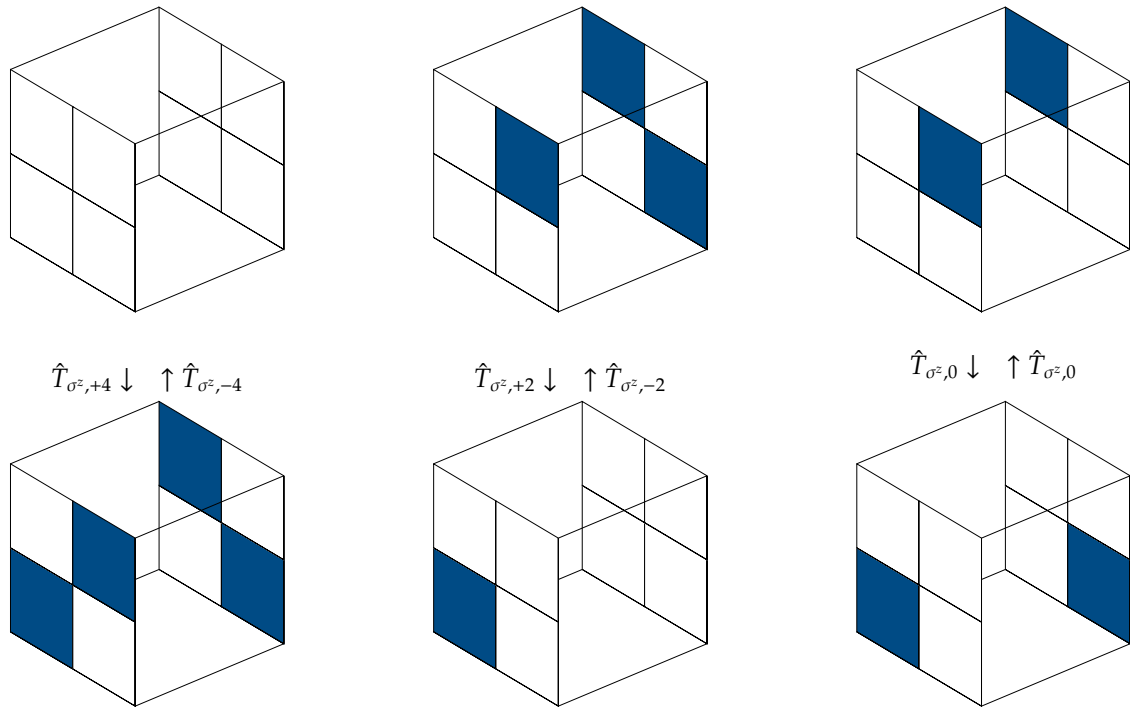
Figure 6.1: Examples of the action of the $\hat{T}_{\sigma^z,n}$ operators in equation 6.14. On the left side, the action of the $\hat{T}_{\sigma^z,+4}$ and $\hat{T}_{\sigma^z,-4}$ operators are shown. The four excitations in the lower part highlight all cubes that a $\hat{T}_{\sigma^z,n}$ operator can act on. A $\hat{T}_{\sigma^z,+2}$ operators annihilates one of the four excitations and creates the remaining three. Hence, a total of two excitations are created. The $\hat{T}_{\sigma^z,-2}$ is the inverse process. A $\hat{T}_{\sigma^z,0}$ operator annihilates two excitations and creates the other two, leading no changed in the number of quasi-particles.

this hardcore-boson picture. $\hat{B}_c$ can be written as $\left(\mathbb{1} - 2\hat{b}_c^\dagger \hat{b}_c\right)$. This can be checked by considering the two cases:

$$\hat{B}_c \,|b_c = +1\rangle = +1\,|b_c = +1\rangle \quad \Leftrightarrow \quad \left(\mathbb{1} - 2\hat{b}_c^\dagger \hat{b}_c\right)|0\rangle = (\mathbb{1} - 2\cdot 0)\,|0\rangle = +1\,|0\rangle,$$

$$\hat{B}_c \,|b_c = -1\rangle = -1\,|b_c = -1\rangle \quad \Leftrightarrow \quad \left(\mathbb{1} - 2\hat{b}_c^\dagger \hat{b}_c\right)|1\rangle = (\mathbb{1} - 2)\,|1\rangle = -1\,|1\rangle.$$

The magnetic field terms can also be expressed with the hardcore boson operators. $\hat{\sigma}_i^z$ can be written as $\prod_{c:\ \hat{\sigma}^x \in \hat{B}_c} \left(\hat{b}_c^\dagger + \hat{b}_c\right)$. Again this can be checked by considering the action of the operator on trial states that are changed by $\hat{\sigma}_i^z$:

$$\hat{\sigma}_i^z \,|b_c = +1\rangle = |b_c = -1\rangle \quad \Leftrightarrow \quad \left(\hat{b}_c^\dagger + \hat{b}_c\right)|0\rangle = (0 - |1\rangle) = |1\rangle,$$

$$\hat{\sigma}_i^z \,|b_c = -1\rangle = |b_c = +1\rangle \quad \Leftrightarrow \quad \left(\hat{b}_c^\dagger + \hat{b}_c\right)|1\rangle = (|0\rangle + 0) = |0\rangle.$$

38

$$\hat{T}_{\mu^z,+4} \downarrow \quad \uparrow \hat{T}_{\mu^z,-4} \qquad\qquad \hat{T}_{\mu^z,+2} \downarrow \quad \uparrow \hat{T}_{\mu^z,-2} \qquad\qquad \hat{T}_{\mu^z,0} \downarrow \quad \uparrow \hat{T}_{\mu^z,0}$$
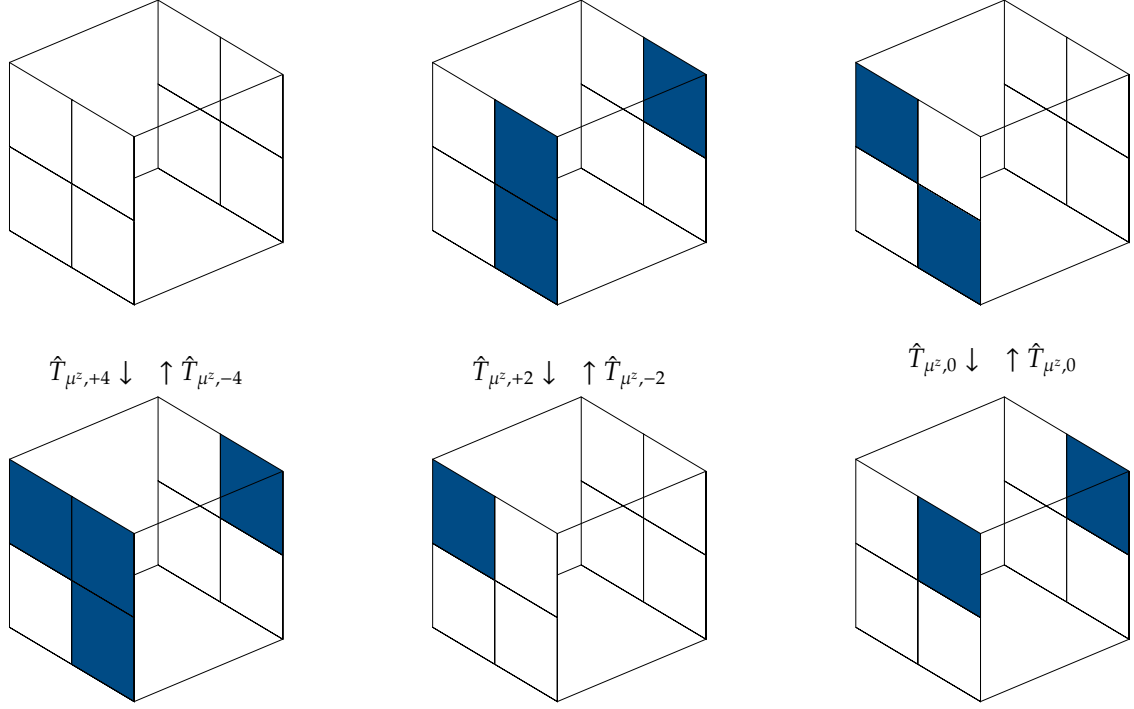
Figure 6.2: Examples of the action of the $\hat{T}_{\mu^z,n}$ operators in equation 6.14. On the left side, the action of the $\hat{T}_{\mu^z,+4}$ and $\hat{T}_{\mu^z,-4}$ operators is shown. The four excitations in the lower part highlight all cubes that a $\hat{T}_{\mu^z,n}$ operator can act on. A $\hat{T}_{\mu^z,+2}$ operator annihilates one of the four excitations and creates the remaining three. Hence, in total two excitations are created. The $\hat{T}_{\mu^z,-2}$ is the inverse process. A $\hat{T}_{\mu^z,0}$ operator annihilates two excitations and creates the other two, leading to no change in the number of quasi-particles.

Similarly, $\hat{\mu}_i^z = \prod_{c:\ \hat{\mu}^x \in \hat{B}_c} \left(\hat{b}_c^\dagger + \hat{b}_c \right)$. Inserting that in Hamiltonian 6.7 yields

$$
\begin{aligned}
\hat{\mathcal{H}} &= -J \cdot N_c - J \sum_c \left(1 - 2\hat{b}_c^\dagger \hat{b}_c \right) - \sum_i \left(h_{\sigma,z} \prod_{c:\ \hat{\sigma}^x \in \hat{B}_c} \left(\hat{b}_c^\dagger + \hat{b}_c \right) + h_{\mu,z} \prod_{c:\ \hat{\mu}^x \in \hat{B}_c} \left(\hat{b}_c^\dagger + \hat{b}_c \right) \right) = \\
&= -2J \cdot N_c + 2J \sum_c \left(\hat{b}_c^\dagger \hat{b}_c \right) - \sum_i \left(h_{\sigma,z} \prod_{c:\ \hat{\sigma}^x \in \hat{B}_c} \left(\hat{b}_c^\dagger + \hat{b}_c \right) + h_{\mu,z} \prod_{c:\ \hat{\mu}^x \in \hat{B}_c} \left(\hat{b}_c^\dagger + \hat{b}_c \right) \right)
\end{aligned}
\tag{6.13}
$$

We can identify the quasi-particle counting operator $\hat{Q} = \sum_c \left(\hat{b}_c^\dagger \hat{b}_c \right)$. Expanding the product over all c we also find explicit expressions for the $\hat{T}$ operators. The summand with only creation operators represent $\hat{T}_{+4}$, all summands with three creation and a single annihilation operators build $\hat{T}_{+2}$, all summands with two creation and two annihilation operators build $\hat{T}_0$. $\hat{T}_{-2}$ and $\hat{T}_{-4}$ are constructed similarly. Using all these identities in equation 6.13 and dividing by $2J$ yields

$$
\begin{aligned}
\frac{\hat{\mathcal{H}}}{2J} &= -N_c + \hat{Q} - \frac{h_{\sigma,z}}{2J} \left(\hat{T}_{\sigma^z,+4} + \hat{T}_{\sigma^z,+2} + \hat{T}_{\sigma^z,0} + \hat{T}_{\sigma,-2} + \hat{T}_{\sigma^z,-4} \right) \\
&\quad - \frac{h_{\mu,z}}{2J} \left(\hat{T}_{\mu^z,+4} + \hat{T}_{\mu^z,+2} + \hat{T}_{\mu^z,0} + \hat{T}_{\mu^z,-2} + \hat{T}_{\mu^z,-4} \right).
\end{aligned}
\tag{6.14}
$$

where $\hat{T}_{\mu^z,n}$ denotes the $\hat{T}_n$ coming from the action of $\hat{\mu}_i^z$ and $\hat{T}_{\sigma^z,n}$ denotes the $\hat{T}_n$ coming from the action of $\hat{\sigma}_i^z$.

From this equation it is also clear, that pCUT can be applied. In figures 6.1 and 6.2 we illustrate the action of the $\hat{T}$ operators on the $\hat{B}_c$ eigenvalues.

For the single field case in chapter 7.1, we set either $h_{\sigma,z}$ or $h_{\mu,z}$ to zero. Therefore we are left with the $\hat{T}$ operators of the remaining field. In the two field case, we set $h_{\sigma,z} = h_{\mu,z} = h$ and have to consider both $\hat{T}_{\sigma^z,n}$ and $\hat{T}_{\mu^z,n}$.

6.4.2 High-field Limit

In the high-field-limit, the stabilizer operators act as a perturbation to the polarized ground state, which is given by all spins pointing in the direction of the magnetic field. Again, we introduce hardcore bosons, this time representing local spin flips. An unoccupied hardcore boson site corresponds to a spin pointing up and an occupied boson to an spin pointing down in z-direction:

$$|\uparrow\rangle \ \hat{=} \ |0\rangle$$
$$|\downarrow\rangle \ \hat{=} \ |1\rangle .$$

The ground state is $|0 \dots 0\rangle$. We introduce two pairs of hardcore bosons with creation and annihilation operators - $\hat{s}$ and $\hat{s}^\dagger$ for the σ-spins and $\hat{m}$ and $\hat{m}^\dagger$ for μ-spins. Analogous to the low-field case, $\hat{\sigma}_i^z$ can be written as $\left(1 - 2\hat{s}_i^\dagger\hat{s}_i\right)$ and $\hat{\mu}_i^z$ as $\left(1 - 2\hat{m}_i^\dagger\hat{m}_i\right)$. A $\hat{B}_c$ operator can then be written as $\prod_{i:\ \hat{\sigma}_i\in\hat{B}_c}\left(\hat{s}_i^\dagger + \hat{s}_i\right)\prod_{i:\ \hat{\mu}_i\in\hat{B}_c}\left(\hat{m}_i^\dagger + \hat{m}_i\right)$. Plugging these identities in equation 6.2 yields

$$
\begin{aligned}
\hat{\mathcal{H}} &= -J \cdot N_c - J\sum_c\left[\prod_{i\in\sigma_c}\left(\hat{s}_i^\dagger + \hat{s}_i\right)\prod_{i\in\mu_c}\left(\hat{m}_i^\dagger + \hat{m}_i\right)\right] - \sum_i\left[h_{\sigma,i}\left(1 - 2\hat{s}_i^\dagger\hat{s}_i\right) + h_{\mu,i}\left(1 - 2\hat{m}_i^\dagger\hat{m}_i\right)\right] = \\
&= -\left(h_{\sigma,i}\cdot N_\sigma + h_{\mu,i}\cdot N_\mu\right) + 2\sum_i\left(h_{\sigma,z}\cdot\hat{s}_i^\dagger\hat{s}_i + h_{\mu,z}\cdot\hat{m}_i^\dagger\hat{m}_i\right) \\
&\quad -J\cdot N_c - J\sum_c\left[\prod_{i\in\sigma_c}\left(\hat{s}_i^\dagger + \hat{s}_i\right)\prod_{i\in\mu_c}\left(\hat{m}_i^\dagger + \hat{m}_i\right)\right].
\end{aligned}
$$

We again can identify the quasi-particle number operators $\hat{Q}_\sigma = \sum_i s^\dagger\hat{s}$ and $\hat{Q}_\mu = \sum_i \hat{m}^\dagger\hat{m}$. Using this, we find

$$
\begin{aligned}
\hat{\mathcal{H}} &= -\left(h_{\sigma,i}\cdot N_\sigma + h_{\mu,i}\cdot N_\mu\right) + 2h_{\sigma,z}\cdot\hat{Q}_\sigma + 2h_{\mu,z}\cdot\hat{Q}_\mu \\
&\quad -J\cdot N_c - J\sum_c\left[\prod_{i\in\sigma_c}\left(\hat{s}_i^\dagger + \hat{s}_i\right)\prod_{i\in\mu_c}\left(\hat{m}_i^\dagger + \hat{m}_i\right)\right].
\end{aligned}
\tag{6.15}
$$

In contrast to the low-field case, we cannot write the $\hat{T}$ operators for both single- and two-field case in one equation. For the single-field case either $h_{\sigma,z}$ or $h_{\mu,z}$ is zero. As a consequence, the corresponding creating and annihilation operators are not contributing. Therefore, the resulting Hamiltonian for $h_{\sigma,z} = 0$ is

$$
\begin{aligned}
\frac{\hat{\mathcal{H}}}{2h_{\mu,i}} &= -\frac{1}{2}N_c + \hat{Q}_\mu - \tilde{\lambda}N_c - \tilde{\lambda}\sum_c\left[\prod_{i\in\mu_c}\left(\hat{m}_i^\dagger + \hat{m}_i\right)\right] \\
&= -\frac{1}{2}N_c + \hat{Q}_\mu - \tilde{\lambda}N_c - \tilde{\lambda}\left(\hat{T}_{B,\mu,-4} + \hat{T}_{B,\mu,-2} + \hat{T}_{B,\mu,0} + \hat{T}_{B,\mu,+2} + \hat{T}_{B,\mu,+4}\right),
\end{aligned}
\tag{6.16}
$$

where $\tilde{\lambda} = \frac{J}{2h_{\mu,i}}$ and $\hat{T}_{B,\mu,n}$ is the $\hat{T}_n$ operator originating from the action of a $\hat{B}_c$ operator on μ quasi-particles. An example for all $\hat{T}_{B,\mu,n}$ operators is shown in figure 6.3.
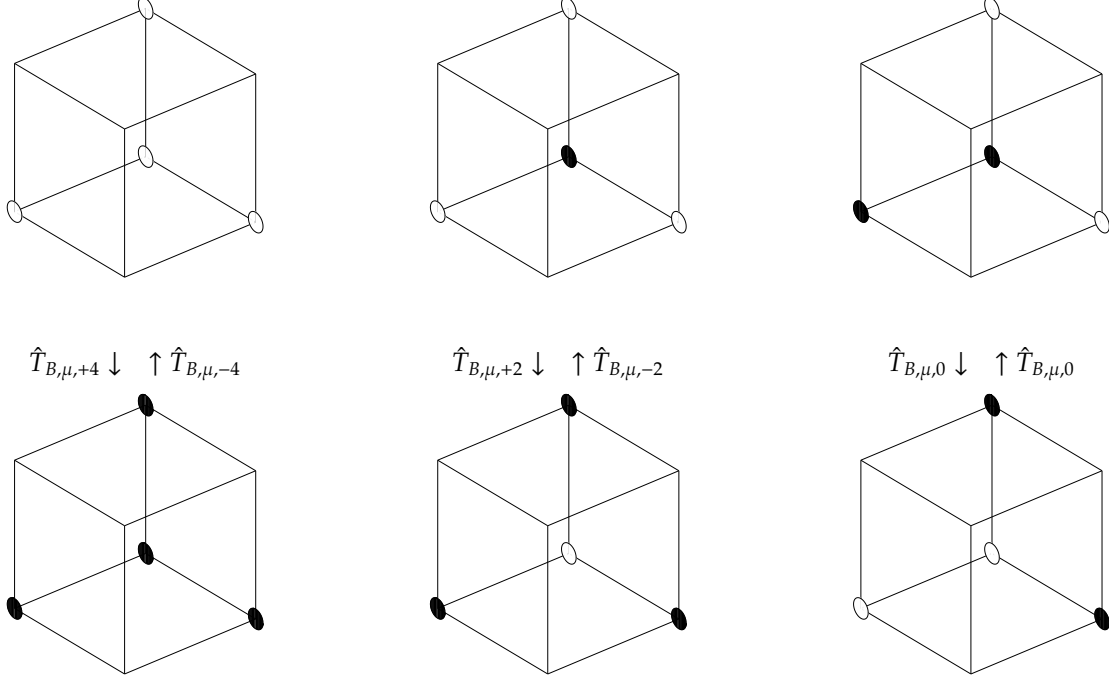

$$\hat{T}_{B,\mu,+4} \downarrow \quad \uparrow \hat{T}_{B,\mu,-4} \qquad\qquad \hat{T}_{B,\mu,+2} \downarrow \quad \uparrow \hat{T}_{B,\mu,-2} \qquad\qquad \hat{T}_{B,\mu,0} \downarrow \quad \uparrow \hat{T}_{B,\mu,0}$$

Figure 6.3: Examples of the action of the $\hat{T}_{B,\mu,n}$ operators in equation 6.16. On the left side, the action of the $\hat{T}_{B,\mu,+4}$ and $\hat{T}_{B,\mu,-4}$ operators is shown. The four excitations in the lower part highlight all μ-spin sites that a $\hat{T}_{\mu,n}$ operator can act on. A $\hat{T}_{B,\mu,+2}$ operators annihilates one of the four excitations and creates the remaining three. Hence, in total two excitations are created. The $\hat{T}_{\mu,-2}$ is the inverse process. A $\hat{T}_{B,\mu,0}$ operator annihilates two excitations and creates the other two, leading to no change in the number of particles.

For the case where $h_{\mu,z} = 0$ we get the similar expression

$$\frac{\hat{\mathcal{H}}}{2h_{\sigma,i}} = -\frac{1}{2}N_c + \hat{Q}_\sigma - \tilde{\lambda}N_c - \tilde{\lambda}\sum_c \left[\prod_{i\in\sigma}\left(\hat{s}_i^\dagger + \hat{s}_i\right)\right]$$

$$= -\frac{1}{2}N_c + \hat{Q}_\sigma - \tilde{\lambda}N_c - \tilde{\lambda}\left(\hat{T}_{B,\sigma,-4} + \hat{T}_{B,\sigma,-2} + \hat{T}_{B,\sigma,0} + \hat{T}_{B,\sigma,+2} + \hat{T}_{B,\sigma,+4}\right), \qquad (6.17)$$

with $\tilde{\lambda} = \frac{J}{2h_{\sigma,i}}$ and $\hat{T}_{B,\sigma,n}$ is the $\hat{T}_n$ operator caused by a $\hat{B}_c$ operator acting on σ quasi-particles. Examples of $\hat{T}_{B,\sigma,n}$ operators are shown in figure 6.4.

Finally, for the two-field case, we set $h_{\sigma,z} = h_{\mu,z} = h_z$ and equation 6.15 becomes

$$\frac{\hat{\mathcal{H}}}{2h} = -N_c + \hat{Q}_\sigma + \hat{Q}_\mu - \tilde{\lambda}N_c$$

$$\tilde{\lambda}\left(\hat{T}_{B,\sigma,-4} + \hat{T}_{B,\sigma,-2} + \hat{T}_{B,\sigma,0} + \hat{T}_{B,\sigma,+2} + \hat{T}_{B,\sigma,+4}\right)\left(\hat{T}_{B,\mu,-4} + \hat{T}_{B,\mu,-2} + \hat{T}_{B,\mu,0} + \hat{T}_{B,\mu,+2} + \hat{T}_{B,\mu,+4}\right)$$

$$= -N_c + \hat{Q}_\sigma + \hat{Q}_\mu - \tilde{\lambda}N_c$$

$$-\tilde{\lambda}\left(\hat{T}_{B,-8} + \hat{T}_{B,-6} + \hat{T}_{B,-4} + \hat{T}_{B,-2} + \hat{T}_{B,0} + \hat{T}_{B,+2} + \hat{T}_{B,+4} + \hat{T}_{B,+6} + \hat{T}_{B,+8}\right) \qquad (6.18)$$

$$\hat{T}_{B,\sigma,+4} \downarrow \quad \uparrow \hat{T}_{B,\sigma,-4} \qquad\qquad \hat{T}_{B,\sigma,+2} \downarrow \quad \uparrow \hat{T}_{B,\sigma,-2} \qquad\qquad \hat{T}_{B,\sigma,0} \downarrow \quad \uparrow \hat{T}_{B,\sigma,0}$$
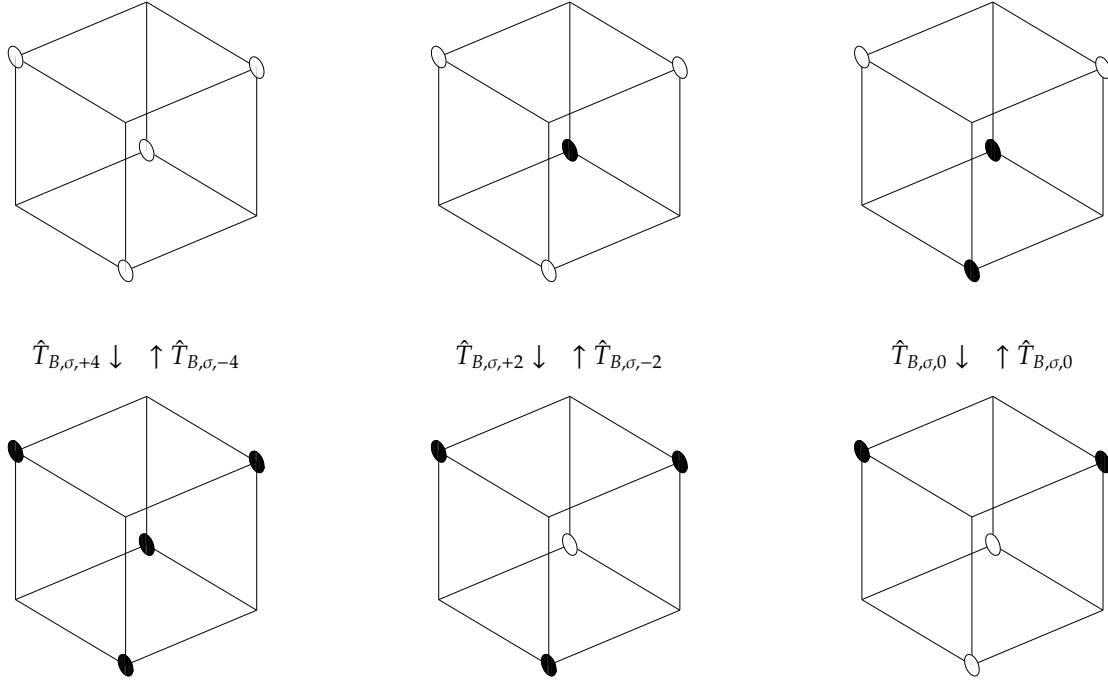

Figure 6.4: Examples of the action of the $\hat{T}_{B,\sigma,n}$ operators in equation 6.17. On the left side, the action of the $\hat{T}_{\sigma,+4}$ and $\hat{T}_{\sigma,-4}$ operators is shown. The four excitations in the lower part highlight all σ spins sites a $\hat{T}_{B,\sigma,n}$ operator can act on. A $\hat{T}_{B,\sigma,+2}$ operators annihilates one of the four excitations and creates the remaining three. Hence, in total two excitations are created. The $\hat{T}_{B,\sigma,-2}$ is the inverse process. A $\hat{T}_{\sigma,0}$ operator annihilates two excitations and creates the other two, leading to no change in the number of quasi-particles.

with $\tilde{\lambda} = \frac{J}{2h}$ and $\hat{T}_{B,n}$ is the $\hat{T}_n$ operator caused by a $\hat{B}_c$ operator acting on both σ and μ quasi-particles. The action on the σ and μ quasi-particles is independent from each other. Hence, a $\hat{T}_{B,n}$ can be interpreted as the action of a $\hat{T}_{B,\sigma,m}$ and $\hat{T}_{B,\mu,k}$ operator, such that $n = m + k$. Therefore, an illustration of the $\hat{T}_{B,n}$ operators would be a combination of the illustrations of the $\hat{T}_{B,\sigma,n}$ and $\hat{T}_{B,\mu,n}$ operators in figures 6.4 and 6.3.

6.4.3 Self duality of the single-field case

In this section we show that up to the exchange of J and h the pCUT results for the high- and low-field limit for the single-field case are identical. For that, we first explicitly write down the Hamiltonian for each case. We start with the low-field case. That means, we set either $h_{\mu,z}$ or $h_{\sigma,z}$ in equation 6.14 to zero. For the σ-field case, we set $h_{\mu,z}$ to zero and $h_{\sigma,z} = h$. We get

$$\frac{\hat{\mathcal{H}}}{2J} = -N_c + \hat{Q} - \lambda \left(\hat{T}_{\sigma,+4} + \hat{T}_{\sigma,+2} + \hat{T}_{\sigma,0} + \hat{T}_{\sigma,-2} + \hat{T}_{\sigma,-4} \right), \tag{6.19}$$

where $\lambda = \frac{h}{2J}$ is the perturbative parameter.

For the μ-field case, we set $h_{\sigma,z} = 0$ and $h_{\sigma,z} = h$. The Hamiltonian then reads

$$\frac{\hat{\mathcal{H}}}{2J} = -N_c + \hat{Q} - \lambda \left(\hat{T}_{\mu,+4} + \hat{T}_{\mu,+2} + \hat{T}_{\mu,0} + \hat{T}_{\mu,-2} + \hat{T}_{\mu,-4} \right), \tag{6.20}$$

where again $\lambda = \frac{h}{2J}$ is the perturbative parameter.

For the high-field case we already established the two cases. For the σ-field case we got (equation 6.17)

$$\frac{\hat{\mathcal{H}}}{2h} = -\frac{1}{2}N_c + \hat{Q}_\sigma - \tilde{\lambda}N_c - \tilde{\lambda}\left(\hat{T}_{B,\sigma,-4} + \hat{T}_{B,\sigma,-2} + \hat{T}_{B,\sigma,0} + \hat{T}_{B,\sigma,+2} + \hat{T}_{B,\sigma,+4}\right), \tag{6.21}$$

where we set $h_{\sigma,z} = h$ and $\tilde{\lambda} = \frac{J}{2h_{\sigma,i}}$ is the perturbative parameter. For the μ-field case, the resulting Hamiltonian for $h_{\sigma,z} = 0$ is

$$\frac{\hat{\mathcal{H}}}{2h} = \frac{1}{2}N_c + \hat{Q}_\mu - \tilde{\lambda}N_c - \tilde{\lambda}\left(\hat{T}_{B,\mu,-4} + \hat{T}_{B,\mu,-2} + \hat{T}_{B,\mu,0} + \hat{T}_{B,\mu,+2} + \hat{T}_{B,\mu,+4}\right) \tag{6.22}$$

where we set $h_{\mu,z} = h$ and $\tilde{\lambda} = \frac{J}{2h}$ is the perturbative parameter.

One can already see that the four equations share the perturbative term

$$\hat{V} = \lambda\left(\hat{T}_{-4} + \hat{T}_{-2} + \hat{T}_0 + \hat{T}_{+2} + \hat{T}_{+4}\right), \tag{6.23}$$

where $\hat{T}_n$ represents one of the four $\hat{T}$ operator types in the above equations and λ one of the four options for the perturbative parameter. In the following we argue that the result of the pCUT for all four options is the same. We approach this as follows. As we mentioned in section 5.1.4, only linked processes contribute to the results in pCUT. This also implies that locally identical processes that are linked in a topologically equivalent way yield the same result. Hence we will first show that all four $\hat{T}_n$ operators act locally in the same way and second that they are linked the same way. Two processes are linked if they share at least one site they both can act on non-trivially. We start by showing that all four processes are locally identical. Then we show that $\hat{T}_{\sigma^z,n}$ and $\hat{T}_{B,\sigma,n}$ are identical and do the same for $\hat{T}_{\mu^z,n}$ and $\hat{T}_{B,\mu,n}$. Finally, we prove that $\hat{T}_{B,\sigma,n}$ and $\hat{T}_{B,\mu,n}$ are linked in a topological equivalent way. This then implies all the remaining identities.

Locally indistinguishable

In the framework of pCUT, processes are locally identical if we have the same type of $\hat{T}$ operators. Similar to section section 5.1, we call these local $\hat{T}$ operators $\hat{\tau}$. That means that we have the same n's and that these $\hat{\tau}_n$ operators act locally in the same way. We now show this all four options.

A $\hat{\tau}_{\sigma,n}$, a $\hat{\tau}_{\mu,n}$, a $\hat{\tau}_{B,\sigma,n}$ and a $\hat{\tau}_{B,\mu,n}$ all act on four spins. Each operator changes the state of all four sites creating particles on an empty site and annihilating particles on occupied sites. That means we cannot have $\hat{\tau}$ operators with an uneven n. Hence we have $\hat{\tau}_{\pm4}$, $\hat{\tau}_{\pm2}$ and $\hat{\tau}_0$ operators for all options. A $\hat{\tau}_n$ creates $\frac{n+4}{2}$ quasi-particles and annihilates $\frac{n-4}{2}$ quasi-particles. All options for $\hat{\tau}_n$ operators to act on the four sites are explicitly given in table 6.4.1. The number of options for $\hat{\tau}_n$ operators for a certain number n can also be calculated. We need any configuration that has $\frac{n+4}{2}$ unoccupied and $\frac{n-4}{2}$ occupied sites. As we can construct these configurations from four contributing sites and the order of the creation and annihilation is not important, we have $\binom{\frac{n+4}{2}}{4}$ $\hat{\tau}_n$ operators.

All of the above relations hold for all four options. Hence, all four are locally identical.

Homotopy of linked $\hat{T}_{\sigma^z,n}$ and $\hat{T}_{B,\sigma,n}$ processes

Figure 6.5 shows the quasi-particles that a local $\hat{\tau}_{\sigma^z,n}$ and a $\hat{\tau}_{B,\sigma,n}$ act on. One can see that both operators act geometrically on the same sites up to a lattice inversion. Therefore, the way in

$\hat{\tau}_{+4}$	$\hat{\tau}_{+2}$	$\hat{\tau}_0$	$\hat{\tau}_{-2}$	$\hat{\tau}_{-4}$
$|0000\rangle \rightarrow |1111\rangle$	$|0001\rangle \rightarrow |1110\rangle$	$|0011\rangle \rightarrow |1100\rangle$	$|1110\rangle \rightarrow |0001\rangle$	$|1111\rangle \rightarrow |0000\rangle$
	$|0010\rangle \rightarrow |1101\rangle$	$|0101\rangle \rightarrow |1010\rangle$	$|1101\rangle \rightarrow |0010\rangle$	
	$\vdots$		$\vdots$	
	$|1000\rangle \rightarrow |0111\rangle$	$\vdots$	$|1110\rangle \rightarrow |0001\rangle$	
		$|1100\rangle \rightarrow |0011\rangle$		

Table 6.4.1: Action of a $\hat{T}$ operator that can occur in the single-field case for an arbitrary but fixed order of the sites. $|0\rangle$ denotes an unoccupied site and $|1\rangle$ an occupied one.
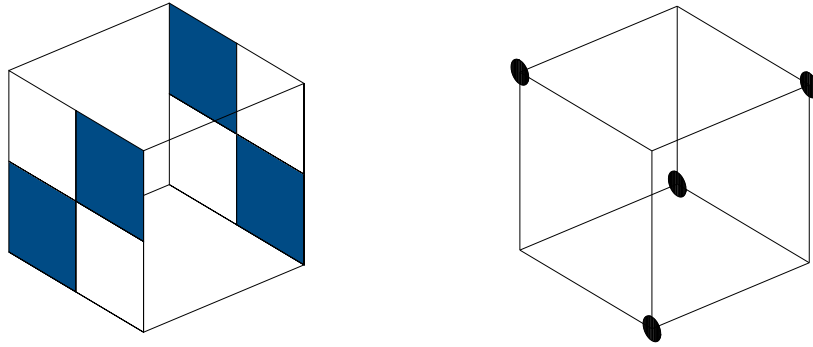
Figure 6.5: Illustration of the quasi-particles a $\hat{\tau}_{\sigma^z,n}$ acts on on the left and the quasi-particles a $\hat{\tau}_{B,\sigma,n}$ acts on on the right. The positions are identical up to a lattice inversion. This shows that the two operators are linked in the same way.

which two neighboring sites are linked is also identical up to a lattice inversion. Together with the local indistinguishably, this proves that the resulting perturbative series for both $\hat{\tau}_{\sigma^z,n}$ and $\hat{\tau}_{B,\sigma,n}$ are identical. As these two cases correspond to high- and low-field case of σ-field case, we call the σ-field case self dual. We discuss the implication of that in section 7.1.3.

Homotopy of linked $\hat{T}_{\mu^z,n}$ and $\hat{T}_{B,\mu,n}$ processes

In figure 6.6 the quasi-particles that a local $\hat{\tau}_{\mu^z,n}$ and a $\hat{\tau}_{B,\mu,n}$ act on are shown. Again the two operators act on the same quasi-particles sites, up to a lattice inversion. Hence these two case are identical and the μ-field case is self dual.

Homotopy of linked $\hat{T}_{B,\sigma,n}$ and $\hat{T}_{B,\mu,n}$ processes

Figure 6.7 shows the quasi-particles sites that the two operators act on. Note that the $\hat{\tau}_{B,\sigma,n}$ operator is rotated by 90° around the z-axis in order to make the illustrations in the following section clearer. We consider all possible links of a cube c with the neighboring cubes. From that we construct a three-dimensional lattice and show that these lattices are topologically equivalent.

We start with the $\hat{\tau}_{B,\sigma,n}$ operator. All processes in cubes that do not have a common site with a cube c, are automatically not linked. That means we only need to investigate the 26 direct neighbors of c. Processes on cubes that share a face not linked, because there is no site on the shared face, where both operators act on non-trivially. The same holds for processes on cubes
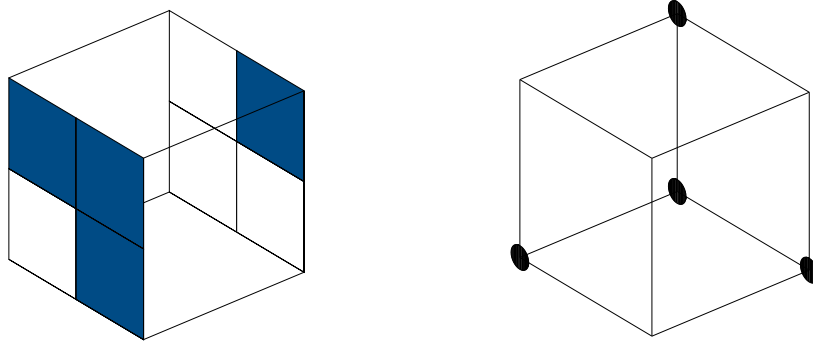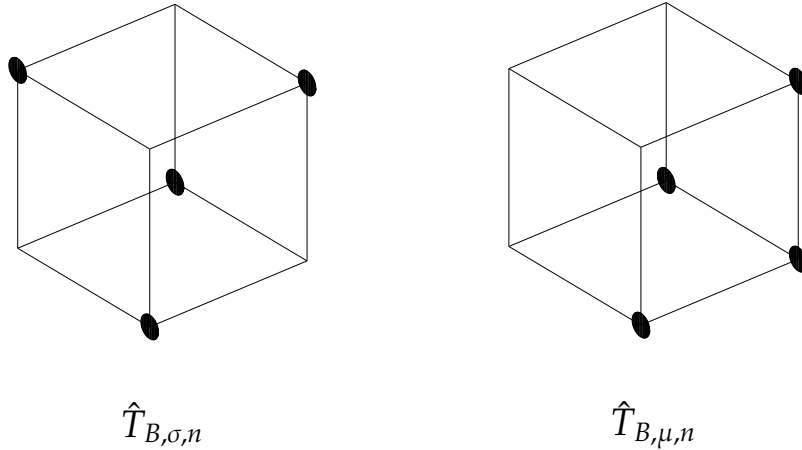
Figure 6.6: Illustration of the quasi-particles a $\hat{\tau}_{\mu^z,n}$ acts on on the left and the quasi-particles a $\hat{\tau}_{B,\mu,n}$ acts on on the right. The positions are identical up to a lattice inversion. This shows that the two operators are linked in the same way.

$$\hat{T}_{B,\sigma,n} \qquad\qquad \hat{T}_{B,\mu,n}$$

Figure 6.7: The left side shows the σ-spins a $\hat{\tau}_{B,\sigma,n}$ operator acts on non-trivially. On the right are the μ-spins shown that a $\hat{\tau}_{B,\mu,n}$ operator acts on non-trivially rotated by 90° around the z-axis are shown. The rotation makes the illustration of the topology of the linked processes in figures 6.8 and 6.9 clearer.

that share a single corner with c. The processes on the twelve cubes that share an edge with c are linked. All of these links are equivalent, because the processes share a single site. At the top left of figure 6.8 the links between connected processes are illustrated. Translating these links for all cubes gives rise to a face-centered cubic (fcc) lattice. In order to see the topological equivalence of between the linking of the $\hat{\tau}_{B,\sigma,n}$ and $\hat{\tau}_{B,\mu,n}$ operators, we highlight the octahedral interstitials of the lattice in the center and on the left of the top row in figure 6.8. These octahedral interstitial of neighboring cubs are shown in figure 6.9.

For the $\hat{\tau}_{B,\sigma,n}$ operators, we find that all processes on cubes that share a face with c are linked to processes on c. All of these processes act on one of the four shared sites non-trivially. Again, the processes on cubes sharing only a corner with c are not linked to processes on c. Six of the processes sharing an edge are linked and six are unlinked. The orientation of the six linked processes can be seen on the bottom left of figure 6.8. All linked processes also share a single
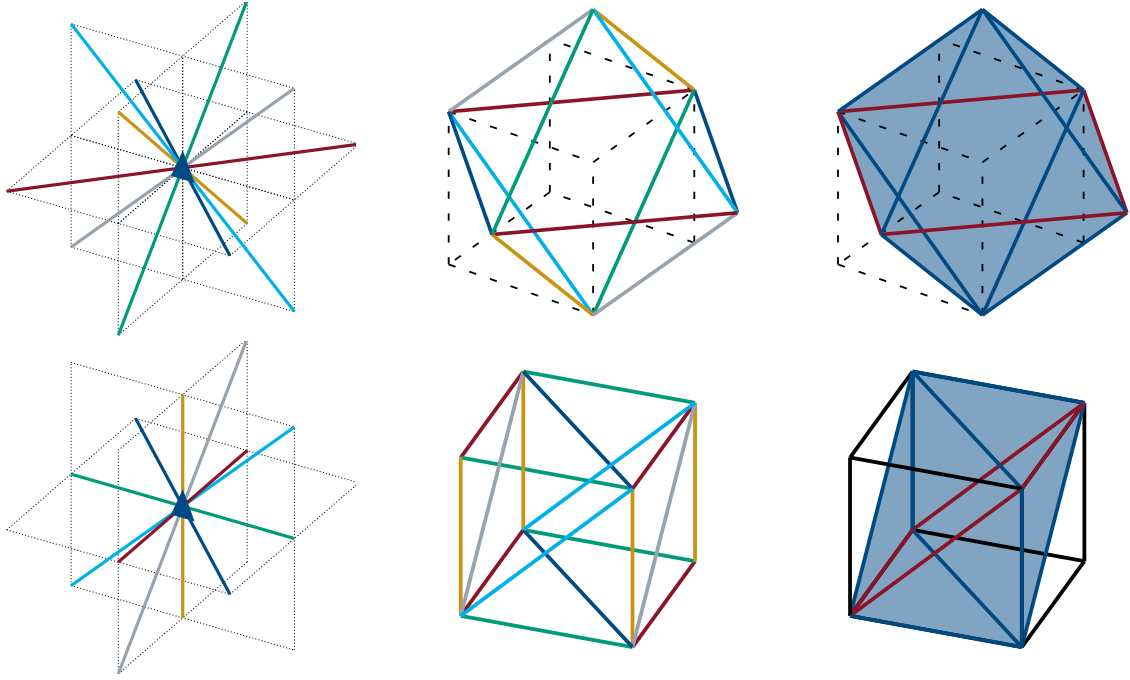
45

Figure 6.8: Topology of the way local processes are linked for the the $\hat{\tau}_{B,\sigma,n}$ operator in the top row and the $\hat{\tau}_{B,\mu,n}$ operator in the bottom row. The local processes in a cube c for the $\hat{\tau}_{B,\sigma,n}$ operators are linked to all processes on cubes that share an edge with c. This is shown at the top left, where a link is illustrated by a colored line. All links are equivalent. Translated, these form a face-centered cubic (fcc) lattice, which is shown in the center of the top row. We highlight the octahedral interstitials of the fcc lattice for an easier comparison of $\hat{\tau}_{B,\sigma,n}$ and $\hat{\tau}_{B,\mu,n}$. The local processes on cube c for the $\hat{\tau}_{B,\mu,n}$ are linked with all processes on cubes that share a face. Additionally, they are linked to six processes on cubes sharing an edge. This is illustrated on left in the bottom row. Translated these linked processes form the structure shown in the center. Again, we can find a octahedra. Hence, $\hat{\tau}_{B,\sigma,n}$ and $\hat{\tau}_{B,\mu,n}$ are linked topologically equivalent. Figure 6.9 shows the octahedral interstitials in neighboring cubes.

site, making them equivalent to the other six linked processes on the faces. As the lattice is transitionally invariant, we can combine this pattern to a three-dimensional lattice. All linked processes are drawn into a single cube in the center of the bottom row in figure 6.8. Similar to the $\hat{T}_{\sigma,n}$ case, we find an octahedral structure. Comparing theses octahedra in five neighboring cubes to the octahedral interstitials of the fcc lattice, one can see that they are topological equivalent. This is shown in figure 6.9. Hence, we showed that $\hat{T}_{B,\sigma,n}$ and $\hat{T}_{B,\mu,n}$ are locally identical and linked in a topological equivalent way. Therefore, the pCUT results are identical.
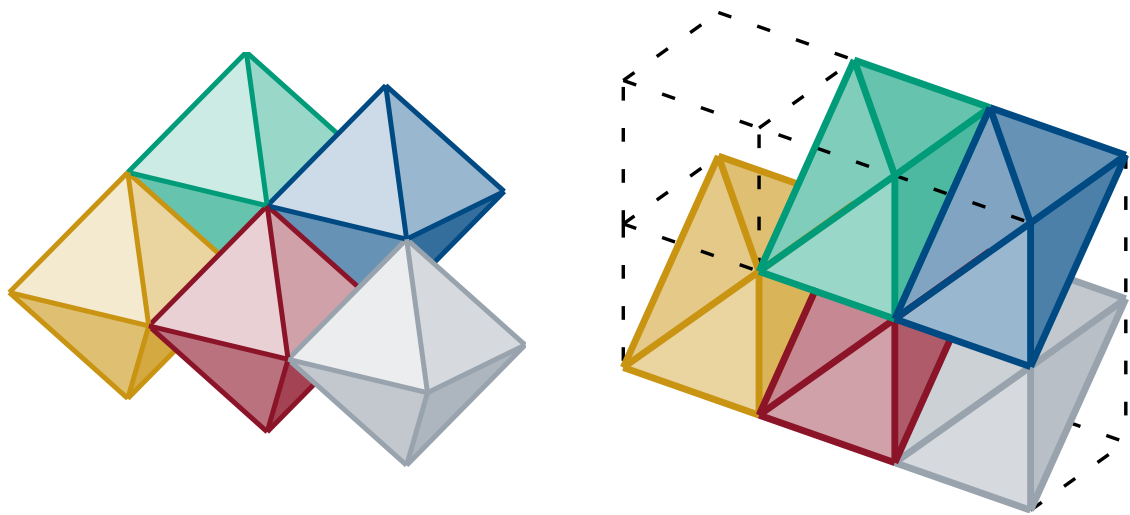
Figure 6.9: Alignment of the octahedral interstitials formed by the linked processes for $\hat{T}_{B,\sigma,n}$ on the left and for $\hat{T}_{B,\mu,n}$ on the right. The octahedra are interstitials of a face-centered cubic lattice. However, the lattice on the right is distorted. As these two configurations are topologically equivalent, pCUT gives the same results for $\hat{T}_{B,\sigma,n}$ and $\hat{T}_{B,\mu,n}$.

Chapter 7

Ground-state energies

In this chapter, we use the results form chapter 6 to investigate the ground-state energies. We will start with the single-field case. Here, we determine the variational ground-state energies and see signs for strong first-order phase transition. For pCUT we explicitly calculate the first two orders of the low-field limit and present the results for the computer aided calculations. Making use of the self-duality, we find a first-order phase transition at exactly $J = h_z$. For the two-field case we again start with the variational energies and continue with pCUT. Similar to the two-field case, we find a first-order phase transition.

7.1 Single-field case

In this section we discuss the results for the single-field case. Physically, one could imagine coupling either all σ- or μ-spin to a heat bath with infinite temperature. That way, all spin configurations of the coupled spin type have the same probability. Hence, the action of a $\hat{A}_c$ or $\hat{B}_c$ operator does not change the state of the spins coupled to the bath and we can look at the remaining spins separately.

We investigate the phase transition of the single-field case by calculating the ground-state energies both with the variational ansatz and pCUT.

7.1.1 Variational results

For the variational case, both single-field cases yield the same result. For this we take the variational result for a general homogeneous magnetic field from equation 6.12

$$\frac{\langle \mathcal{H} \rangle_\beta}{N_c} = -J \frac{(1+\beta)^2}{1+\beta^2} - (h_{\sigma,z} + h_{\mu,z}) \left(\frac{1-\beta^2}{1+\beta^2} \right)^4 .$$

One can see that both σ- and μ- field contribute with the same factor $\left(\frac{1-\beta^2}{1+\beta^2} \right)^4$. By setting either $h_{\sigma,z}$ or $h_{\mu,z}$ to zero and renaming the remaining field to h we get both times

$$\epsilon = \frac{\langle \mathcal{H} \rangle_\beta}{2N_c J} = -\frac{1}{2} \frac{(1+\beta)^2}{1+\beta^2} - \lambda \left(\frac{1-\beta^2}{1+\beta^2} \right)^4 , \tag{7.1}$$

with $\lambda = \frac{h}{2J}$. The left side of figure 7.1 shows equation 7.1 as a function of β for different values of λ. The idea is that for a certain λ the state realizes the configuration encoded by β with the lowest energy. Hence, we track the local and global minima for different λ. For $\lambda = 0$, i.e. the topological phase, there is exactly one minimum for $\beta = 1$. The curves at that point become flatter for higher λ, but the minimum at $\beta = 1$ stays stationary. At $\lambda \approx 0.3$ a new local minimum emerges at $\beta \approx 0.2$. The point where this new local minimum overtakes the minimum at $\beta = 1$ marks the phase transition. The value of β for the global minimum jumps from 1 to approximately 0.2 at the critical value of λ. This jump corresponds to a first-order phase transition. The critical value of $\lambda_c = 0.422$.
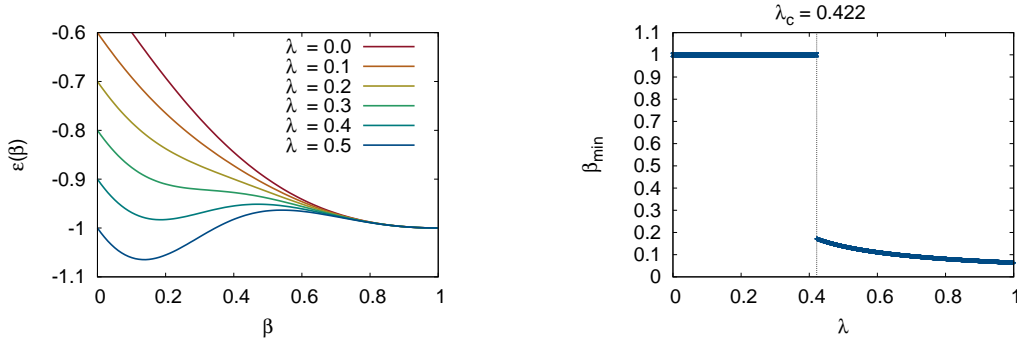
Figure 7.1: The mean ground-state energy per site for the single-field case divided by $2J$ as a function of β for different values of λ. The persisting minimum at $\beta = 1$ and $\epsilon = 1.0$ marks the topological phase. The emerging minimum at $\beta \approx 0.2$ can be interpreted as the polarized phase. The point where the polarized minimum passes the topological minimum marks the phase transition. At this point β_{min} jumps from 1 to approximately 0.2, which is shown on the left. This indicates a first-order phase transition. The critical value is $\lambda_c = 0.422$

We can also plot the energy of both the topological and the polarized minimum as a function of λ. This is done in figure 7.2. One can see that the two curves intersect in a non-continuous way at $\lambda_c = 0.422$. Additionally, this plot can be compared directly to the pCUT results below.

7.1.2 pCUT: Explicit calculations up to fourth order

In the following, we apply pCUT the the low-field limit in the case where just the σ-field contributes. The Hamiltonian is given in equation 6.19. Due to the self-duality of the single-field case, we can directly translate the results to the high-field limit. Using equation 5.6, we can expand equation 6.19 up to second order

$$\frac{\hat{\mathcal{H}}_{\text{eff}}}{2J} = -N_c + \sum_{k=1}^{\infty} \lambda^k \sum_{\substack{|\mathbf{m}|=k, \\ M(\mathbf{m})=0}} C(\mathbf{m})\hat{T}(\sigma, \mathbf{m}) =$$

$$= -N_c + \lambda C(0)\hat{T}_{\sigma,0} + \sum_{n=0}^{2} \frac{1}{2n}\left[\hat{T}_{\sigma,2n}, \hat{T}_{\sigma,-2n}\right] + O(\lambda^3) \tag{7.2}$$

In order to calculate the ground-state energy we evaluate $\langle 0| \frac{\hat{\mathcal{H}}_{\text{eff}}}{2J} |0\rangle$. We will consider each summand separately. A $\hat{T}_n$ operator can be interpreted in two ways. It can act on the state to the
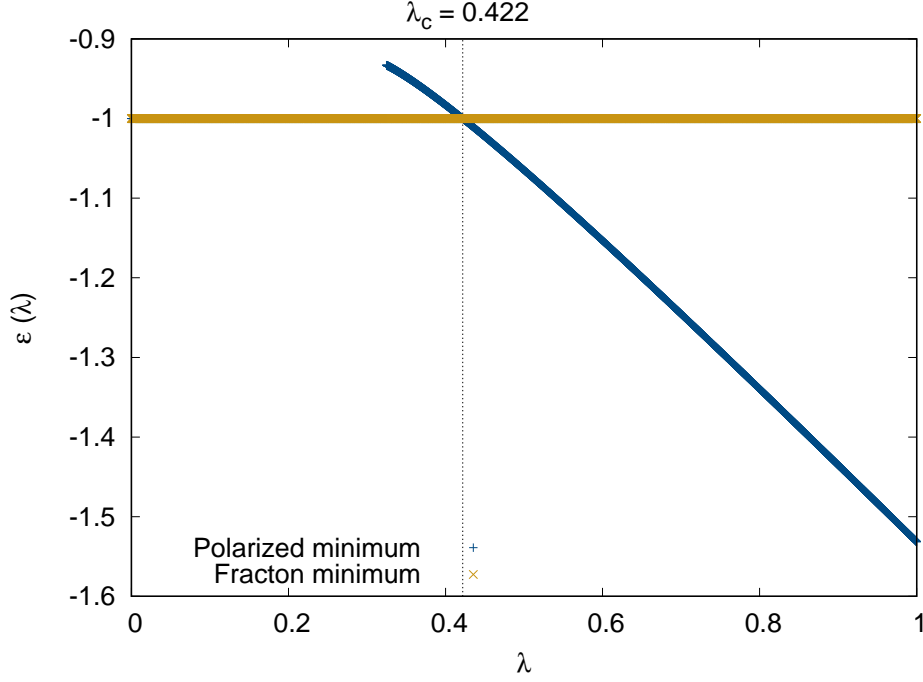
Figure 7.2: The mean ground-state energy per site for the single-field case divided by $2J$ as a function of β for different values of λ for both minimums in figure 7.1. The energies of the two minima intersect at $\lambda_c = 0.422$ in a non-continuous way, which indicates a first-order phase transition.

right as it is or it can act on the state on the left as its hermitian conjugate. As we act on both sides on the ground state, per construction the state without excitations, all operators that include an annihilation of at least one excitation give no contribution. These are all sequences that end with $\hat{T}_{\sigma,0}$, $\hat{T}_{\sigma,\pm 2}$ or $\hat{T}_{\sigma,-4}$ and all sequences that start with $\hat{T}_{\sigma,0}$, $\hat{T}_{\sigma,\pm 2}$ or $\hat{T}_{\sigma,+4}$. Therefore, the summands $\langle 0| \hat{T}_{\sigma,-2}\hat{T}_{\sigma,+2} |0\rangle$, $\langle 0| \hat{T}_{\sigma,+2}\hat{T}_{\sigma,-2} |0\rangle$ and $\langle 0| \hat{T}_{\sigma,+4}\hat{T}_{\sigma,-4} |0\rangle$ all give zero contribution. We are left with $\langle 0| \hat{T}_{\sigma,-4}\hat{T}_{\sigma,+4} |0\rangle$, which we will analyze starting from the right. The first step is

$$\hat{T}_{\sigma,+4} |0\rangle = \sum_i \hat{\tau}_{\sigma,+4,i} |0\rangle = \sum_i \left| \raisebox{-0.5em}{\includegraphics[height=1.2em]{hex}} \right\rangle_i,$$

where $\left| \raisebox{-0.5em}{\includegraphics[height=1.2em]{hex}} \right\rangle_i$ is the state where the four colored spins surrounding site i are flipped.

$$\hat{T}_{\sigma,-4}\hat{T}_{\sigma,+4} |0\rangle = \sum_j \hat{\tau}_{\sigma-4,j} \sum_i \left| \raisebox{-0.5em}{\includegraphics[height=1.2em]{hex}} \right\rangle_i = \sum_{j=i} |0\rangle + \sum_{j\neq i} 0 = N_c |0\rangle,$$

because the only operator that can annihilate four spins for $\left| \raisebox{-0.5em}{\includegraphics[height=1.2em]{hex}} \right\rangle_i$ is the one acting on site i. Hence, $\langle 0| \hat{T}_{\sigma,-4}\hat{T}_{\sigma,4} |0\rangle = N_c$. Using this in equation 7.2, we conclude

$$\langle 0| \frac{\hat{\mathcal{H}}_{\text{eff}}}{2J} |0\rangle = -N_c - \frac{\lambda^2 \cdot N_c}{4} + O(\lambda^3). \tag{7.3}$$

One can calculate the fourth order in a similar way. All contributing coefficients and multiplicities are listed in appendix A. We divide the result up to 4th order by N_c and get

$$\epsilon_{LF} = \frac{\hat{\mathcal{H}}_{\text{eff}}}{2JN_c} = -1 - \lambda^2 \frac{1}{4} - \lambda^4 \frac{3}{64} + O(\lambda^5).$$

Using the result this for the high-field limit in equation 6.17 yields

$$\epsilon_{HF} = \frac{\hat{\mathcal{H}}_{\text{HF}}}{2hN_c} = -\frac{1}{2} - \tilde{\lambda} - \tilde{\lambda}^2 \frac{1}{4} - \tilde{\lambda}^4 \frac{3}{64} + O(\tilde{\lambda}^6).$$

For higher orders we use computer aided evaluation.

pCUT: Computer aided results

For the evaluation of $\hat{\mathcal{H}}_{\text{eff}}$ in higher orders we used a computer program that systematically evaluates all operator sequences on a finite cluster. As explained in section 5.1.5 we choose periodic boundary conditions for ground-state energies. In order to prevent contributing, linked processes over the periodic boundary, the cluster must be a $7 \times 7 \times 7$ cube in 6th order. However, we can further reduce the size of the cluster. The linked sites for the $\hat{T}_{\sigma^z,n}$ form a three-dimensional checkerboard pattern. This is illustrated in figure 7.3. For periodic boundary conditions and even linear system sizes L, we have two independent checkerboard patterns. Hence, we can choose an $8 \times 8 \times 8$ cube as a cluster and only half of the sites are contributing. This reduces the number of site from $7^3 = 343$ to $\frac{8^3}{2} = 256$.
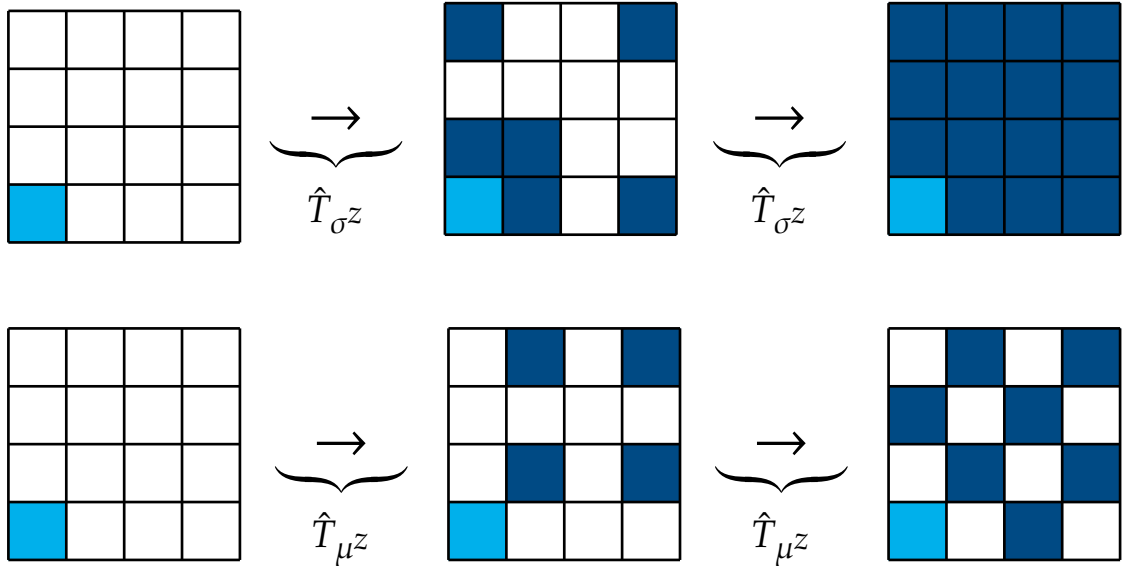
Figure 7.3: Cluster construction for both the $\hat{T}_{\mu^z,n}$ in the top row and $\hat{T}_{\sigma^z,n}$ in the bottom row for periodic boundary conditions reduced to two dimensions. For both cases we start from the site in the bottom left. Then we add all linked sites step by step. For $\hat{T}_{\mu^z,n}$ this process quickly fills the whole lattice, while the cluster for the $\hat{T}_{\sigma^z,n}$ is a checkerboard pattern, which only contains half of the sites. Note that this is only applicable for even lattice sizes.

The result for the ground-state energy in the low-field case is

$$\epsilon_{\text{LF}} = \frac{\hat{\mathcal{H}}_{\text{LF}}}{2JN_c} = -1 - \lambda^2 \frac{1}{4} - \lambda^4 \frac{3}{64} - \lambda^6 \frac{559}{15360} + O(\lambda^8), \tag{7.4}$$

where $\lambda = \frac{J}{2h}$. The result for the high-field case is

$$\epsilon_{\text{HF}} = \frac{\hat{\mathcal{H}}_{\text{HF}}}{2hN_c} = -\frac{1}{2} - \tilde{\lambda} - \tilde{\lambda}^2 \frac{1}{4} - \tilde{\lambda}^4 \frac{3}{64} - \tilde{\lambda}^6 \frac{559}{15360} + O(\tilde{\lambda}^8), \tag{7.5}$$

where $\tilde{\lambda} = \frac{h}{2J}$. The two above expressions have the same form apart from the zeroth order. This is due to the fact that the term $-JN_c$ coming for the fixed $\hat{A}_c$ eigenvalues in equation 6.2 has a different form in the units of the two cases. For the low-field limit, we divide by $2JN_c$ and that way $-JN_c$ becomes $-\frac{1}{2}$. In contrast to that, we divide by $2h_zN_c$ in the high-field limit and $-JN_c$ becomes $-\tilde{\lambda}$. Subtracting these two factors from the corresponding equations 7.4 and 7.5 results in the exact same form.

A plot of the low-field limit including Padé approximants is shown in figure 7.4. As expected, the influence of the magnetic field lowers the energies of the ground state. One can see that the bare series and the Padé approximates are close until $\lambda \approx 0.6$. As we see in chapter 7.1.3, the critical point is at $\lambda = 0.5$. Hence, the series is convergent in this regime.
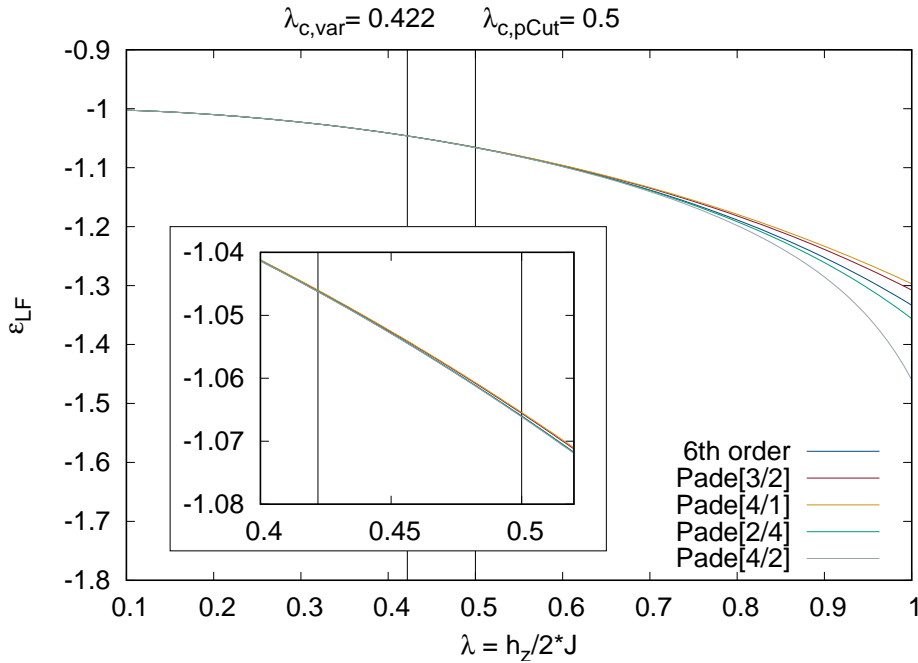
Figure 7.4: Low-field expansion of the ground-state energy per site in the single-field case using pCUT. The perturbation lowers the energy of the ground state. In order to gain insight about the convergence of the series, the bare series and its Padé approximants are plotted. All agree in the relevant regime from 0.4 to 0.5.

As we later want to compare the pCUT calculation with the variational ansatz, we want to plot all results in the same figure. This means that we have to use the same units for all cases. We choose to plot $\frac{\hat{\mathcal{H}}}{2JN_c}$ as a function of $\lambda = \frac{h}{2J}$. Hence, we have to multiply equation 7.5 with $\frac{h}{J}$ and rewrite $\tilde{\lambda} = \frac{1}{4\lambda}$. A plot of the high-field limit results including Padé approximants are shown

in figure 7.5. Similar to what we observed for the low-field case, the series is convergent in the relevant regime.
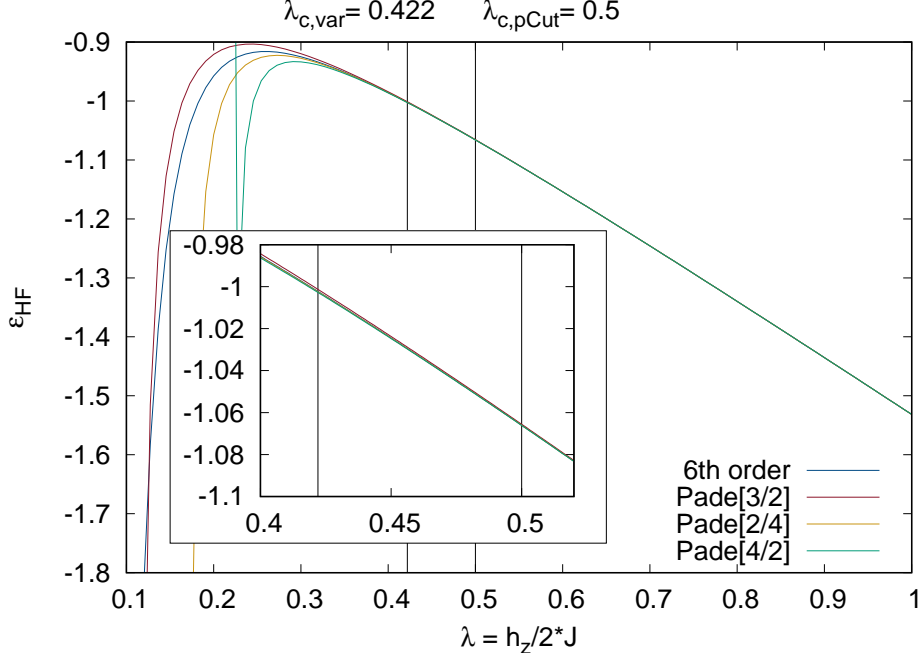

Figure 7.5: High-field expansion fo the mean ground-state energy per site ϵ for the single-field case by pCUT and the relevant Padé approximations in the units of the low-field case. One can see that the bare series and the approximations agree in the relevant case from 0.4 to 0.5.

The 7th order is the limit for our calculations. This is mainly due to the exponentially growing number of possible $\hat{T}$ operator sequences and the need of a $10 \times 10 \times 10$ cluster in eighth order. Both combined lead to a memory usage of over $200\,\text{GB}$ RAM, which is the limit for the available system. This large memory usage could be reduced by the a graph expansion. We will elaborate on that in the outlook in chapter 9.

In the next section, we investigate the phase transition with the obtained pCUT results and compare it with the results for the variational ansatz.

7.1.3 Phase transition

We now plot the curves in figures 7.2, 7.4 and 7.5 into one plot in figure 7.6.

The high-field case for the pCUT intersect exactly at $\lambda = 0.5$. This follows from the self-duality of the σ- and μ-field case. To see this from the series, we start by subtracting the constant contribution of the $\hat{A}_c$ operators. For the low-field limit the contribution of the unchanged $\hat{A}_c$ operators is $-\frac{1}{2}$. Subtracting these from the expression in equation 7.4 yields

$$\epsilon_{\text{LF}} = -\frac{1}{2} - \lambda^2 \frac{1}{4} - \lambda^4 \frac{3}{64} - \lambda^6 \frac{559}{15360} + O(\lambda^8).$$

For the high-field case, the $\hat{A}_c$ operator gives the contribution $-\tilde{\lambda}$. Subtracting this from equation 7.5 we get

$$\epsilon_{\text{HF}} = -\frac{1}{2} - \tilde{\lambda}^2 \frac{1}{4} - \tilde{\lambda}^4 - \frac{3}{64} \tilde{\lambda}^6 \frac{559}{15360} + O(\tilde{\lambda}^8).$$

As λ and $\tilde{\lambda}$ can be converted into each other by exchanging J and h, this implies that

$$\epsilon_{\text{LF}}(J, h) = \epsilon_{\text{HF}}(h, J). \tag{7.6}$$

Hence ϵ_{LF} and ϵ_{HF} intersect exactly at $h = J$. This is also true for all higher orders.

We can also compare the variational results with the pCUT results. In figure 7.6 one can see that curves for the high-field case for pCUT and the polarized minimum in the variational approach agree. This implies that the variational ansatz captures the physics of the polarized phase and gives quantitatively good results. However, this is different for the fracton phase. The calculated variational energies do not change in the magnetic field, while the ground-state energy obtained by pCUT indicates a lowering of the energy. This implies that the variational ansatz does not capture the correct energetics of the fracton phase. The fact that the variational approach yields higher energies than pCUT is plausible. By making a variational ansatz, we use the variational parameters to span a space of states and minimize the energy of these states. However, if the true ground state of the problem is not in this space, we will not find the state with the lowest possible energy. Therefore, if the ground state is in the variational space we get correct ground-state energy by minimizing within this variational space. Conversely, if the true ground state is not in the variational space, the lowest energy in the variational space can only be higher than the ground state. The stationary behavior of the fracton minimum also explains why the critical $\lambda_{\text{c,var}} = 0.422$ is 16% lower than the exact $\lambda_{\text{c}} = 0.5$.
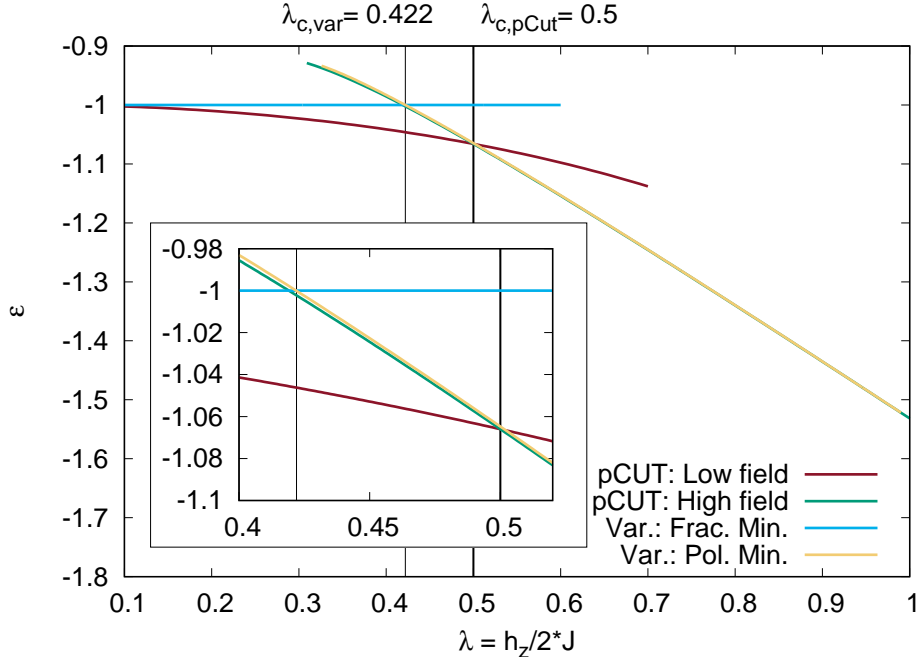

Figure 7.6: Ground-state energy per site in the single-field case for pCUT and the variational ansatz. The high- and low-field expansion for pCUT intersect exactly at $\lambda_{\text{c,pCUT}} = 0.5$ due to the self-duality of the two limiting phases. This result also holds for all higher orders. The variational curve for the fracton minimum and the polarized minimum intersect at $\lambda_{\text{c,var}} \approx 0.422$. The variational result is 16% lower than due to the fact that the energy of the fracton minimum is not changed by the perturbation in the variational approach.

7.2 Results for the two-field case

In this chapter we consider the case where $h_{\sigma,z} = h_{\mu,z} = h$. That means that both magnetic fields are pointing into the z-direction with the same strength h. This case describes the whole system in a homogeneous magnetic field. The phase transition is identical to the case, where a magnetic field points in x-direction, due to the symmetry of $\hat{A}_c$ and $\hat{B}_c$ operators. We will start with the variational calculation and continue with the high- and low-field pCUT expansion.

7.2.1 Variational energies

Similar to the approach for the single-field case, we start with equation 6.12. By setting $h_{\sigma,z} = h_{\mu,z} = h$ we get

$$\frac{\langle \mathcal{H} \rangle_\beta}{2JN_c} = -\frac{1}{2}\frac{(1+\beta)^2}{1+\beta^2} - 2\lambda\left(\frac{1-\beta^2}{1+\beta^2}\right)^4, \tag{7.7}$$

where $\lambda = \frac{h}{2J}$. The only difference to the single-field case in equation 7.1 is the factor 2 in front of λ. Hence, the results of determining the global and local minima with respect to β for a certain λ are the same than for the the single-field case with $2 \cdot \lambda$. The relevant plots are shown in figure 7.7.
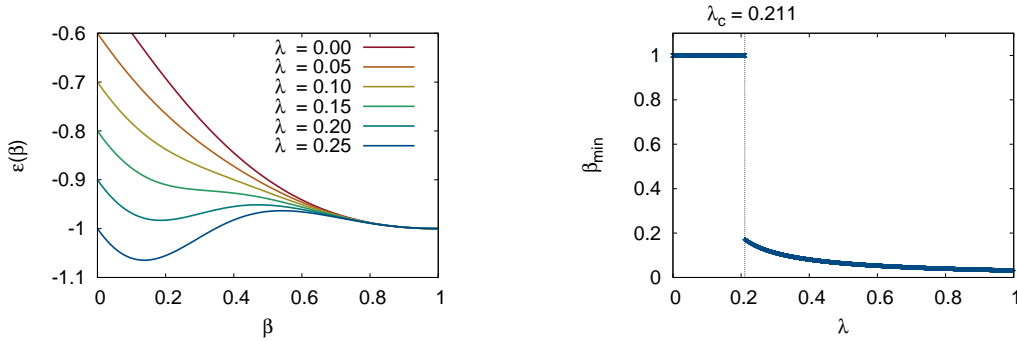
Figure 7.7: The mean ground-state energy per site for the two-field case divided by $2J$ as a function of β for different values of λ. The persisting minimum at $\beta = 1$ and $\epsilon/2J = 1.0$ marks the fracton phase. The emerging minimum at $\beta \approx 0.2$ can be interpreted as the polarized phase. The point where the polarized minimum passes the topological minimum marks the phase transition. At this point $\beta_{\min}$ jumps from 1 to approximately 0.2, which is shown on the left. This indicates a first-order phase transition. The critical value of $\lambda_{c,var} = 0.2109$

Figure 7.8 shows the energy of both the fracton and the polarized minimum as a function of λ. One can see that the two curves intersect in a non-continuous way at $\lambda_{c,var} = 0.2109$, which is exactly half of the value for the single-field case.
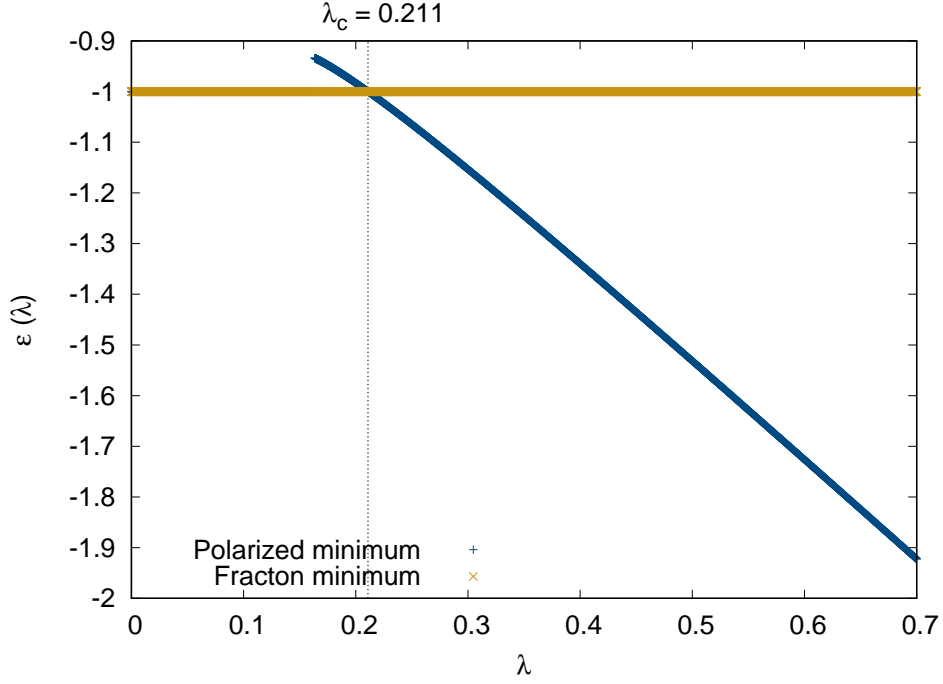
Figure 7.8: The mean ground-state energy per site for the two-field case divided by $2J$ for different values of λ for both minimums in figure 7.1. The energies of the two minima intersect at $\lambda_{c,var} = 0.2109$ in a non-continuous way, which indicates a first-order phase transition.

7.2.2   pCUT: Low-field limit

For the low-field limit, we use equation 6.14 and set $h_{\sigma,z} = h_{\mu,z} = h$. This yields

$$
\frac{\hat{\mathcal{H}}}{2J} = -N_c + \hat{Q} - \lambda\Big[\big(\hat{T}_{\sigma^z,+4} + \hat{T}_{\sigma^z,+2} + \hat{T}_{\sigma^z,0} + \hat{T}_{\sigma,-2} + \hat{T}_{\sigma^z,-4}\big)
$$
$$
+ \big(\hat{T}_{\mu^z,+4} + \hat{T}_{\mu^z,+2} + \hat{T}_{\mu^z,0} + \hat{T}_{\mu^z,-2} + \hat{T}_{\mu^z,-4}\big)\Big],
\tag{7.8}
$$

where $\lambda = \frac{h}{2J}$.

Again, we treat the first two orders explicitly and then continue with the result of the computer aided calculation. For the explicit evaluation we insert the result for the effective Hamiltonian in equation 5.6 and get

$$
\frac{\hat{\mathcal{H}}_{\text{eff}}}{2J} = -N_c + \hat{Q} + \sum_{\substack{\lambda=k}}^{\infty} \lambda^k \sum_{\substack{|\mathbf{m}|=k,\\ M(\mathbf{m})=0}} C(\mathbf{m})\hat{T}(\mathbf{m})
$$
$$
= -N_c + \lambda C(0)\hat{T}_{\sigma,0} + \sum_{n=0}^{2} \frac{1}{2n}\Big[\hat{T}_{2n}, \hat{T}_{-2n}\Big] + O(\lambda^3)
\tag{7.9}
$$

Analogous to the single-field case only the $\hat{T}_{-4}\hat{T}_{+4}$ summand contributes. For evaluating $\langle 0|\,\hat{T}_{-4}\hat{T}_{+4}\,|0\rangle$ we start with

$$
\hat{T}_4\,|0\rangle = \big(\hat{T}_{\sigma,+4} + \hat{T}_{\mu,+4}\big)|0\rangle = \sum_i \big(\hat{\tau}_{\sigma,+4,i} + \hat{\tau}_{\mu,+4,i}\big)|0\rangle = \sum_i \left(\left|\vcenter{\hbox{\includegraphics{a}}}\right\rangle_i + \left|\vcenter{\hbox{\includegraphics{b}}}\right\rangle_{i'}\right),
$$

where $\left|\;\vcenter{\hbox{[cube]}}\;\right\rangle_i$ and $\left|\;\vcenter{\hbox{[cube]}}\;\right\rangle_i$ are the states where the four colored cubes surrounding site i are flipped. The next step is

$$\hat{T}_{-4}\sum_i \left(\left|\;\vcenter{\hbox{[cube]}}\;\right\rangle_i + \left|\;\vcenter{\hbox{[cube]}}\;\right\rangle_i\right) = \sum_j \left(\hat{\tau}_{\sigma,-4,j} + \hat{\tau}_{\mu,-4,j}\right)\sum_i \left(\left|\;\vcenter{\hbox{[cube]}}\;\right\rangle_i + \left|\;\vcenter{\hbox{[cube]}}\;\right\rangle_i\right) = 2N_c \left|0\right\rangle. \tag{7.10}$$

Therefore, $\langle 0|\,\hat{T}_{-4}\hat{T}_{+4}\,|0\rangle = 2N_c$. Note that, this is twice the result of the single field, because there are twice as many $\hat{T}_{\pm 4}$ operators for the dual field case. Using this in equation 7.9 we get

$$\hat{\mathcal{H}}_{\text{eff}} = -N_c + \hat{Q} - \lambda^2 \frac{N_c}{2} + O(\lambda^3). \tag{7.11}$$

For the computer aided evaluation, we took a $7 \times 7 \times 7$ cluster with periodic boundary conditions. The results is

$$\epsilon_{\text{LF}} = \frac{\hat{\mathcal{H}}_{\text{LF}}}{2JN_c} = -1 - \lambda^2 \frac{1}{2} - \lambda^4 \frac{7}{24} - \lambda^6 \frac{18907}{30720} + O(\lambda^8).$$

ϵ_{LF} as a function of λ is plotted together with the relevant Padé approximants in figure 7.4. One can see that magnetic field lowers the ground-state energy and the functions agree in the relevant regime.
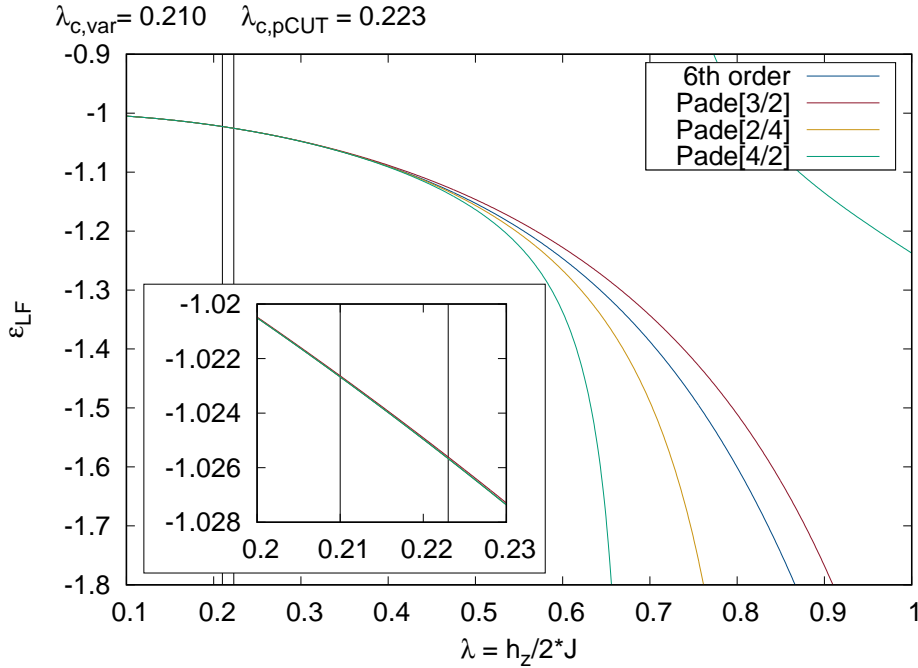

Figure 7.9: Low-field limit of the mean ground-state energy per site obtained by pCUT as a function of the perturbation $\lambda = \frac{h}{2J}$. The perturbation lowers the energy of the state. In order to get a measure for the convergence of the series, the relevant Padé approximants are plotted. One can see that the bare series and the Padé approximants agree in the most relevant regime from 0.20 to 0.25.

7.2.3 pCUT: High-field limit

For the high-field case, we take the Hamiltonian 6.18

$$
\begin{aligned}
\frac{\hat{\mathcal{H}}}{2h} &= -N_c + \hat{Q}_\sigma + \hat{Q}_\mu - \tilde{\lambda} N_c \\
&\quad - \tilde{\lambda}\left(\hat{T}_{B,-8} + \hat{T}_{B,-6} + \hat{T}_{B,-4} + \hat{T}_{B,-2} + \hat{T}_{B,0} + \hat{T}_{B,+2} + \hat{T}_{B,+4} + \hat{T}_{B,+6} + \hat{T}_{B,+8}\right),
\end{aligned}
$$

where each $\hat{T}_{B,n}$ is a combination of a $\hat{T}_{B,\sigma,m}$ and a $\hat{T}_{B,\mu,k}$ operator, such that $n = m + k$.

We start again by doing the fist two orders explicitly. We use the result of the effective Hamiltonian in equation 5.6 and get

$$
\begin{aligned}
\frac{\hat{\mathcal{H}}_{\text{eff}}}{2J} &= -N_c + \hat{Q}_\sigma + \hat{Q}_\mu - \tilde{\lambda} N_c + \sum_{\lambda=k}^{\infty} \lambda^k \sum_{\substack{|\mathbf{m}|=k, \\ M(\mathbf{m})=0}} C(\mathbf{m})\hat{T}(\mathbf{m}) \\
&= -N_c + \hat{Q}_\sigma + \hat{Q}_\mu + \lambda C(0)\hat{T}_{B,0} + \sum_{n=0}^{4} \frac{1}{2n}\left[\hat{T}_{B,2n}, \hat{T}_{B,-2n}\right] + O(\lambda^3)
\end{aligned}
\tag{7.12}
$$

In order to get the ground-state energy, we evaluate $\langle 0| \frac{\hat{\mathcal{H}}_{\text{eff}}}{2J} |0\rangle$. This time, only the $\hat{T}_{B,+8}$ operator includes no annihilation of a quasi-particle. Hence, all sequences except the $\hat{T}_{B,-8}\hat{T}_{B,+8}$ sequence give no contribution. We evaluate $\langle 0| \hat{T}_{B,-8}\hat{T}_{B,+8} |0\rangle$ by starting with

$$
\hat{T}_{B,+8} |0\rangle = \sum_i \tau_{B,+8,i} |0\rangle = \sum_i \left| \underset{\sigma}{\boxtimes}, \underset{\mu}{\boxtimes} \right\rangle_i,
\tag{7.13}
$$

where $\left| \underset{\sigma}{\boxtimes}, \underset{\mu}{\boxtimes} \right\rangle_i$ is the state where all σ quasi-particle sites at the marked corners of $\boxtimes$ and all μ quasi-particle site at the marked corners of $\boxtimes$ are occupied. Acting with the $\hat{T}_{B,-8}$ operator on the state gives one non-zero contribution per summand, because the only site in the lattice where eight quasi-particles can be annihilated is the site where eight were created by the $\hat{\tau}_{B,+8,i}$ operator in the first step. Hence,

$$
\hat{T}_{B,-8} \sum_i \left| \underset{\sigma}{\boxtimes}, \underset{\mu}{\boxtimes} \right\rangle_i = N_c |0\rangle.
\tag{7.14}
$$

Using this in equation 7.12 we get

$$
\langle 0| \frac{\hat{\mathcal{H}}_{\text{eff}}}{2J} |0\rangle = -N_c - \tilde{\lambda} N_c - \tilde{\lambda}^2 \frac{N_c}{8} + O(\tilde{\lambda}^3).
\tag{7.15}
$$

For the computer aided calculation, we again used a $7 \times 7 \times 7$ cluster with periodic boundary conditions. Note that, we now have two types of quasi-particles on each lattice site. Hence, we have a total of $2 \cdot 7^3 = 686$ bits representing quasi-particles. The result is

$$
\epsilon = \langle 0| \frac{\hat{\mathcal{H}}_{\text{eff}}}{2J N_c} |0\rangle = -1 - \tilde{\lambda} - \frac{1}{8}\tilde{\lambda}^2 - \frac{19}{7168}\tilde{\lambda}^4 - \frac{373249}{433520640}\tilde{\lambda}^6 + O(\tilde{\lambda}^8).
\tag{7.16}
$$

As a coefficients for all orders are negative, we can see that the perturbation lowers the energy of the ground state. This is what we expect. The limiting factor for higher orders is memory. A graph expansion could reduce the needed memory, which discuss in the outlook in section 9.

Similar to the single-field case, we want to plot the high- and low-field limit in the same graph. Therefore, we again multiply equation 7.16 by $\frac{h}{J}$ and use $\tilde{\lambda} = \frac{1}{4\lambda}$. This is shown in figure 7.10. One can see that the bare series and the Padé approximants are close for $\lambda > 0.2$. However, in the inset one can see that the series differ slightly in the phase transition regime.
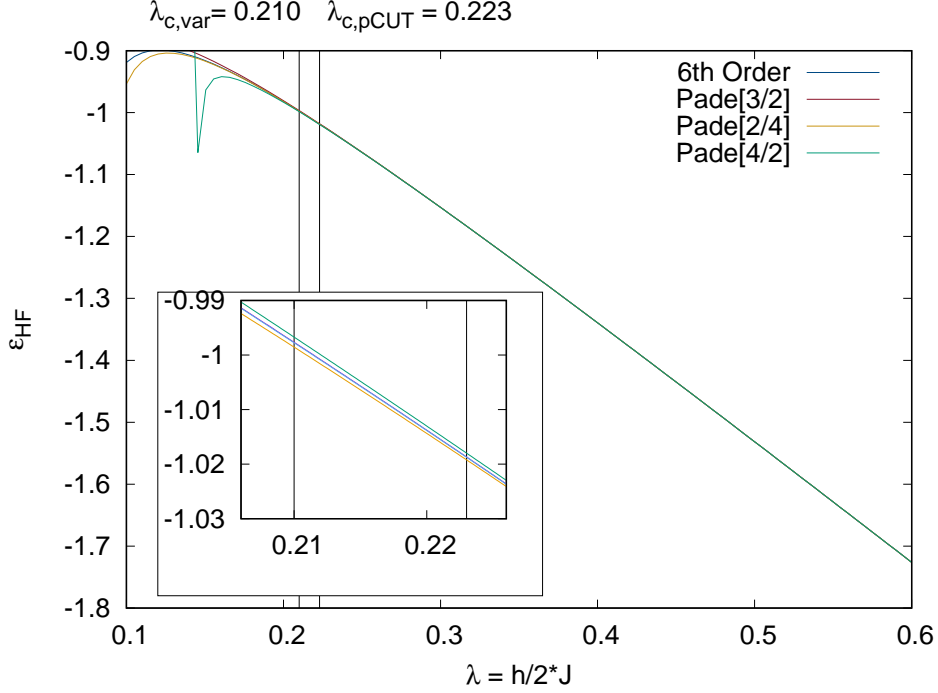

Figure 7.10: High-field limit of the mean ground-state energy per site obtained by pCUT as a function of the perturbation parameter of the low-field limit $\lambda = \frac{h}{2J}$. In this plot, the unperturbed energy is the line that both the bare series and the Padé approximants converge to for large λ. The perturbation lowers the energy of the state. In order to see where the series is converging, the relevant Padé approximates are plotted. One can see that the bare series and the Padé approximants agree in the most relevant regime from 0.20 to 0.25.

7.2.4 Phase transition

We now plot the curves in figures 7.8, 7.9 and 7.10 into one plot as in figure 7.11. One can see that the variational ground-state energies and the pCUT results agree qualitatively. For both methods the two energies intersect in a non-continuous way.

In order to give a mean value and an uncertainty for the critical λ, we numerically calculate the intersection of all Padé approximates of the low-field limit with all Padé approximates of the high-field case. The result is $\lambda_{c,pCUT} = 0.2280 \pm 0.0003$, where 0.0003 is not an error in the usual way, but rather an uncertainty that is connected to the different ways to extrapolate the series. This result is approximately 6% lower than the variational result of $\lambda_{c,var} = 02109$. The fact that the variational energy is lower than the pCUT result is expected. We already discussed this for this single-field case in section 7.1.3.
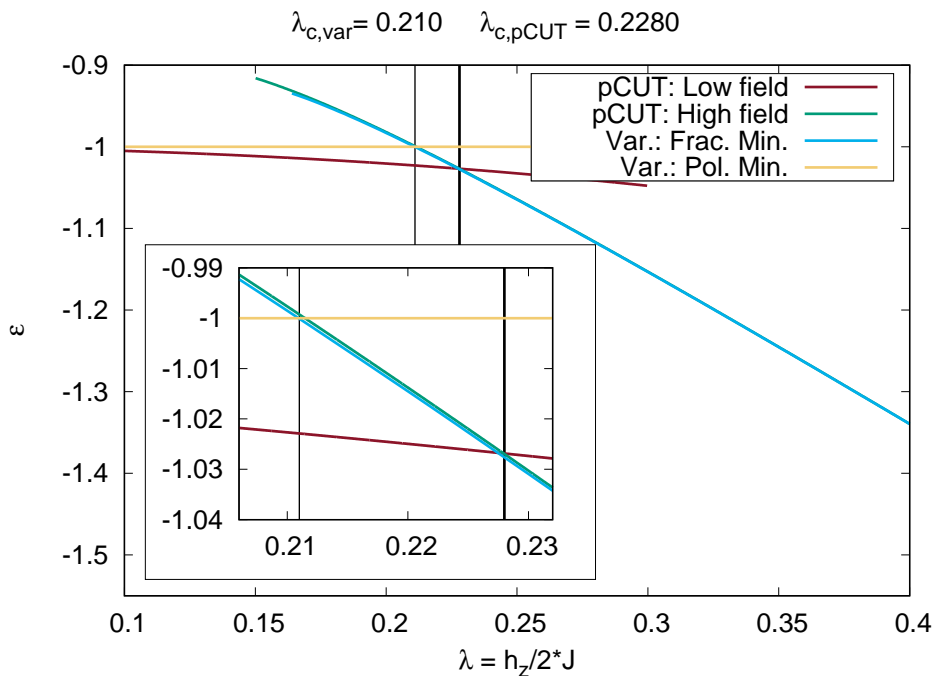
Figure 7.11: Ground-state energy per site for pCUT and the variational ansatz for the two-field case. The high- and low-field expansion for pCUT intersect at $\lambda = 0.2280 \pm 0.003$. The uncertainty is the standard deviation of the energies at which the relevant Padé approximates of the low- and high-field limit intersect. The variational curve for the fracton minimum and the polarized minimum intersect at $\lambda \approx 0.2109$. The variational result is 6% lower than the results obtained by pCUT, because the lowering of the energy of the fracton phase in the magnetic field seems not to be captured by the variational ansatz.

7.3   Results for the mixed-field case

For the mixed-field case, we already established in equations 6.5 and 6.6 that we can write the Hamiltonian for both options as

$$\hat{\mathcal{H}} = \underbrace{-J\sum_c \hat{A}_c - \sum_i h_{\sigma,x} \cdot \hat{\sigma}_i^x}_{\hat{\mathcal{H}}_{A,\sigma^x}} \underbrace{-J\sum_c \hat{B}_c - h_{\mu,z} \cdot \hat{\mu}_i^z}_{\hat{\mathcal{H}}_{B,\mu^z}}, \tag{7.17}$$

$$\hat{\mathcal{H}} = \underbrace{-J\sum_c \hat{A}_c - \sum_i h_{\mu,x} \cdot \hat{\sigma}_i^x}_{\hat{\mathcal{H}}_{A,\mu^x}} \underbrace{-J\sum_c \hat{B}_c - h_{\mu,z} \cdot \hat{\sigma}_i^z}_{\hat{\mathcal{H}}_{B,\sigma^z}}, \tag{7.18}$$

where both $[\hat{\mathcal{H}}_{A,\sigma^x}, \hat{\mathcal{H}}_{B,\mu^z}] = 0$ and $[\hat{\mathcal{H}}_{A,\mu^x}, \hat{\mathcal{H}}_{B,\sigma^z}] = 0$. Additionally, $\hat{\mathcal{H}}_{A,\sigma^x}$ and $\hat{\mathcal{H}}_{B,\mu^z}$ give the same results due to the symmetry between $\hat{A}_c$ and $\hat{B}_c$. The same also holds for $\hat{\mathcal{H}}_{A,\mu^x}, \hat{\mathcal{H}}_{B,\sigma^z}$. Due to the homotopy of the linking of the $\hat{T}$ operators in $\hat{\mathcal{H}}_{B,\mu^z}$ and $\hat{\mathcal{H}}_{B,\sigma^z}$ established in section 7.1, both 7.17 and 7.18 yield the same result. In the following, we apply the variational ansatz to the mixed-field case. This is new, because, we consider a case where $\alpha \neq 1$ and minimize an energy for two variational parameters α and β. We will use the pCUT results from the single-field case and compare them with the variational approach.

We will consider the case where the σ-field points in z-direction and the μ-field in x-direction. The Hamiltonian then reads

$$\hat{\mathcal{H}} = -J\sum_c \left(\hat{A}_c + \hat{B}_c\right) - h_{\sigma,z}\sum_i \hat{\sigma}_i^z - h_{\mu,x}\sum_i \hat{\mu}_i^x. \tag{7.19}$$

The ground state in the high- and low-field limit are different from the single- and two-field case. In the high-field limit, all σ-spins are aligned in z-direction, while the μ-spins point in x-direction. We indicate this state with $|h\rangle = \left|\Uparrow_\sigma, \Rightarrow_\mu\right\rangle$. In the low-field limit the ground state is the topological fracton state given in equation 4.4. In contrast to previous cases, we use projectors acting on the high-field ground state $|h\rangle = \left|\Uparrow_\sigma, \Rightarrow_\mu\right\rangle$ instead of $|\Uparrow\rangle$. That way, the low-field limit ground state reads

$$|0\rangle = \prod_c \left(\frac{\mathbb{1} + \hat{A}_c}{2}\right)\left(\frac{\mathbb{1} + \hat{B}_c}{2}\right)\left|\Uparrow_\sigma, \Rightarrow_\mu\right\rangle. \tag{7.20}$$

This is highly entangled state including all options to flip μ-spins due to the action of the $\hat{A}_c$ operators and all options to flip the σ-spin due to the action of the $\hat{B}_c$ operators.

7.3.1   Variational ansatz

Despite the fact that we already analyzed that the mixed-field case is a superposition of two single-field cases, we want to do the variational calculations explicitly. The main reason is that we cannot set either α or β to one, because both eigenvalues can be changed by the magnetic terms. In the following we show explicitly that the calculation considering both $\alpha \neq 1$ and $\beta \neq 1$ yields the expected sum of two independent terms.

We start from the general form of the variational state (equation 5.8)

$$\left|\alpha, \beta\right\rangle = \mathcal{N}\prod_c \left(\mathbb{1} + \alpha\hat{A}_c\right)\prod_c \left(\mathbb{1} + \beta\hat{B}_c\right)\left|\Uparrow_\sigma, \Rightarrow_\mu\right\rangle,$$

where we set $|h\rangle = \left|\Uparrow_\sigma, \Rightarrow_\mu\right\rangle$. In the following, we calculate the normalization and the energy per site for the whole state $|\alpha, \beta\rangle$.

Normalization

For the Normalization we start with

$$
\begin{aligned}
\langle \alpha, \beta | \alpha, \beta \rangle &= \mathcal{N}^2 \left\langle \Uparrow_\sigma, \Rightarrow_\mu \right| \left(\prod_c (\mathbb{1} + \alpha \hat{A}_c) \prod_c (\mathbb{1} + \beta \hat{B}_c) \right) \left(\prod_c (\mathbb{1} + \alpha \hat{A}_c) \prod_c (\mathbb{1} + \beta \hat{B}_c) \right) \left| \Uparrow_\sigma, \Rightarrow_\mu \right\rangle \\
&= \mathcal{N}^2 \left\langle \Uparrow_\sigma, \Rightarrow_\mu \right| \left(\prod_c (\mathbb{1} + \alpha \hat{A}_c)^2 \prod_c (\mathbb{1} + \beta \hat{B}_c)^2 \right) \left| \Uparrow_\sigma, \Rightarrow_\mu \right\rangle \\
&= \mathcal{N}^2 \left\langle \Uparrow_\sigma, \Rightarrow_\mu \right| \prod_c \left((1 + \alpha^2) + 2\hat{A}_c \right) \left((1 + \beta^2) + 2\hat{B}_c \right) \left| \Uparrow_\sigma, \Rightarrow_\mu \right\rangle \\
&= \mathcal{N}^2 \left(1 + \alpha^2 \right)^{N_c} \left(1 + \beta^2 \right)^{N_c}.
\end{aligned}
$$

Therefore, $\mathcal{N}^2 = \left(1 + \alpha^2 \right)^{-N_c} \left(1 + \beta^2 \right)^{-N_c}$.

Calculation of $\left\langle \hat{A}_c \right\rangle_{\beta,\alpha}$ and $\left\langle \hat{B}_c \right\rangle_{\beta,\alpha}$

For the contribution of an $\hat{A}_c$ operator we get

$$
\begin{aligned}
\langle \alpha, \beta | \hat{A}_{c'} | \alpha, \beta \rangle &= \mathcal{N}^2 \left\langle \Uparrow_\sigma, \Rightarrow_\mu \right| \left(\prod_c (\mathbb{1} + \alpha \hat{A}_c) \prod_c (\mathbb{1} + \beta \hat{B}_c) \right) \hat{A}_{c'} \left(\prod_c (\mathbb{1} + \alpha \hat{A}_c) \prod_c (\mathbb{1} + \beta \hat{B}_c) \right) \left| \Uparrow_\sigma, \Rightarrow_\mu \right\rangle \\
&= \mathcal{N}^2 \left(1 + \beta^2 \right)^{N_c} \left\langle \Uparrow_\sigma, \Rightarrow_\mu \right| \prod_c (\mathbb{1} + \alpha \hat{A}_c) \prod_c \hat{A}_{c'} \prod_c (\mathbb{1} + \alpha \hat{A}_c) \left| \Uparrow_\sigma, \Rightarrow_\mu \right\rangle \\
&= \mathcal{N}^2 \left(1 + \beta^2 \right)^{N_c} \left\langle \Uparrow_\sigma, \Rightarrow_\mu \right| \prod_{c \neq c'} (\mathbb{1} + \alpha \hat{A}_c)^2 (\hat{A}_{c'} + \alpha \mathbb{1})(\mathbb{1} + \alpha \hat{A}_{c'}) \left| \Uparrow_\sigma, \Rightarrow_\mu \right\rangle \\
&= \mathcal{N}^2 \left(1 + \beta^2 \right)^{N_c} \left(1 + \alpha^2 \right)^{N_c-1} 2\alpha = \frac{2\alpha}{1 + \alpha^2},
\end{aligned}
$$

where we used the fact that $\hat{A}_{c'}$ commutes with all $\hat{B}_c$ from the first to the second line. Analogously, we get

$$
\langle \alpha, \beta | \hat{B}_{c'} | \alpha, \beta \rangle = \frac{2\beta}{1 + \beta^2}.
$$

Calculation of $\langle \hat{\sigma}^z \rangle_{\beta,\alpha}$ and $\langle \hat{\mu}^x \rangle_{\beta,\alpha}$

The expectation value of a $\hat{\sigma}^z$ operator is

$$
\begin{aligned}
\langle \alpha, \beta | \hat{\sigma}_i^z | \alpha, \beta \rangle &= \mathcal{N}^2 \left\langle \Uparrow_\sigma, \Rightarrow_\mu \right| \left(\prod_c (\mathbb{1} + \alpha \hat{A}_c) \prod_c (\mathbb{1} + \beta \hat{B}_c) \right) \hat{\sigma}_i^z \left(\prod_c (\mathbb{1} + \alpha \hat{A}_c) \prod_c (\mathbb{1} + \beta \hat{B}_c) \right) \left| \Uparrow_\sigma, \Rightarrow_\mu \right\rangle \\
&= \mathcal{N}^2 \left(1 + \alpha^2 \right)^{N_c} \left\langle \Uparrow_\sigma, \Rightarrow_\mu \right| \prod_c (\mathbb{1} + \beta \hat{B}_c) \prod_c \hat{\sigma}_i^z \prod_c (\mathbb{1} + \beta \hat{B}_c)) \left| \Uparrow_\sigma, \Rightarrow_\mu \right\rangle \\
&= \mathcal{N}^2 \left(1 + \alpha^2 \right)^{N_c} \left\langle \Uparrow_\sigma, \Rightarrow_\mu \right| \prod_{i \neq c} (\mathbb{1} + \beta \hat{B}_c)^2 \prod_{i \in c} (\mathbb{1} + \beta \hat{B}_c)(\mathbb{1} - \beta \hat{B}_c) \left| \Uparrow_\sigma, \Rightarrow_\mu \right\rangle \\
&= \mathcal{N}^2 \left(1 + \beta^2 \right)^{N_c} \left(1 + \alpha^2 \right)^{N_c-4} \left(1 - \alpha^2 \right)^4 \alpha = \left(\frac{1 - \alpha^2}{1 + \alpha^2} \right)^4,
\end{aligned}
$$

where we made use of $\left[\hat{A}_c, \hat{\sigma}_i^z\right] = 0 \; \forall i, c$ from the first to the second line.

For $\hat{\mu}_i^x$ we can again do the calculation in a similar way and get

$$\langle \alpha, \beta | \hat{\mu}_i^x | \alpha, \beta \rangle = \left(\frac{1 - \beta^2}{1 + \beta^2} \right)^4 . \tag{7.21}$$

Variational energy per site

Using all the results from above we can write down the expression for the energy per site

$$\epsilon = \frac{\langle \mathcal{H} \rangle_{\alpha,\beta}}{N_c 2J} = \frac{1}{N_c 2J} \left[-J \sum_c \frac{2\alpha}{1 + \alpha^2} - J \sum_c \frac{2\beta}{1 + \beta^2} - \sum_p \left(h_{\sigma,z} \left(\frac{1 - \beta^2}{1 + \beta^2} \right)^4 + h_{\mu,x} \left(\frac{1 - \alpha^2}{1 + \alpha^2} \right)^4 \right) \right]$$

$$= -\frac{1}{2} \frac{2\alpha}{1 + \alpha^2} - \underbrace{\lambda_x}_{\frac{h_{\mu,x}}{2J}} \left(\frac{1 - \alpha^2}{1 + \alpha^2} \right)^4 - \frac{1}{2} \frac{2\beta}{1 + \beta^2} - \underbrace{\lambda_z}_{\frac{h_{\sigma,z}}{2J}} \left(\frac{1 - \beta^2}{1 + \beta^2} \right)^4 . \tag{7.22}$$

As expected, this term looks like two copies of the single-field case. Therefore, we expect two independent phase transitions. One at $\lambda_x = \frac{h_{\mu,x}}{2J} \approx 0.422$ indicated by a jump in α and one at $\lambda_z = \frac{h_{\sigma,z}}{2J} \approx 0.422$ for a jump in β.

In figure 7.12, we choose $\lambda_z = \lambda$ and $\lambda_x = 1.5 \cdot \lambda$ and plot the two-dimensional energy landscape for different values of λ. Indeed, one can see that the minimum for $\alpha = \beta = 1$ is global minimum for $\lambda_x < \lambda_c$ and $\lambda_z < \lambda_c$. For $\lambda = 0.4$, that means, $\lambda_x = 0.6 > \lambda_c$ and $\lambda_z = 0.4 < \lambda_c$, the a global minimum is at $\beta = 1$ and $\alpha \approx 0.2$. Hence, the σ-spins are still in the fracton phase, while the μ-spin are already in the polarized phase. For $\lambda = 0.6$, hence both $\lambda_x > \lambda_c$ and $\lambda_z > \lambda_c$ the global minimum is at $\alpha \approx 0.15$ and $\beta \approx 0.2$. This indicates that both spin types are in the polarized phase. The plot in the bottom right in figure 7.12 shows the the jump of α and β from 1 to 0.2. The jump of α is occurs at $\lambda = s0.281$, which corresponds to $\lambda_x \approx 0.422$.

7.3.2 pCUT

As already described in section 6.1, we can write the mixed field Hamiltonian as

$$\hat{\mathcal{H}} = -J \sum_c \left(\hat{A}_c + \hat{B}_c \right) - h_{\sigma,z} \sum_i \hat{\sigma}_i^z - h_{\mu,x} \sum_i \hat{\mu}_i^x .$$

$$= \underbrace{-J \sum_c \hat{A}_c - h_{\mu,x} \sum_i \hat{\mu}_i^x}_{\hat{\mathcal{H}}_{A,\mu}} + \underbrace{-J \sum_c \hat{b}_c - h_{\sigma,x} \sum_i \hat{\sigma}_i^x}_{\hat{\mathcal{H}}_{B,\sigma}} .$$

All terms in $\hat{\mathcal{H}}_{A,\mu}$ commute with all terms in $\hat{\mathcal{H}}_{B,\sigma}$, that is $[\hat{A}_c, \hat{B}_{c'}] = 0 \; \forall c, c'$, $[\hat{A}_c, \hat{\sigma}_i^z] = 0 \; \forall c, i$, $[\hat{\mu}_i^x, \hat{B}_c] = 0 \; \forall i, c$ and $[\hat{\mu}_i^x, \hat{\sigma}_j^z] = 0 \; \forall i, j$. This means that the two systems are independent of each other. Hence, we can do the pCUT for each system individually.

We start with

$$\hat{\mathcal{H}}_{B,\sigma} = -J \sum_c \hat{B}_c - h_{\mu,x} \sum_i \hat{\sigma}_i^z . \tag{7.23}$$

One can see that this is the same Hamiltonian than the single-field case in equation 6.7 without the constant $-JN_c$ that came form the fixed $\hat{A}_c$ operator eigenvalues. Hence, we already calculated
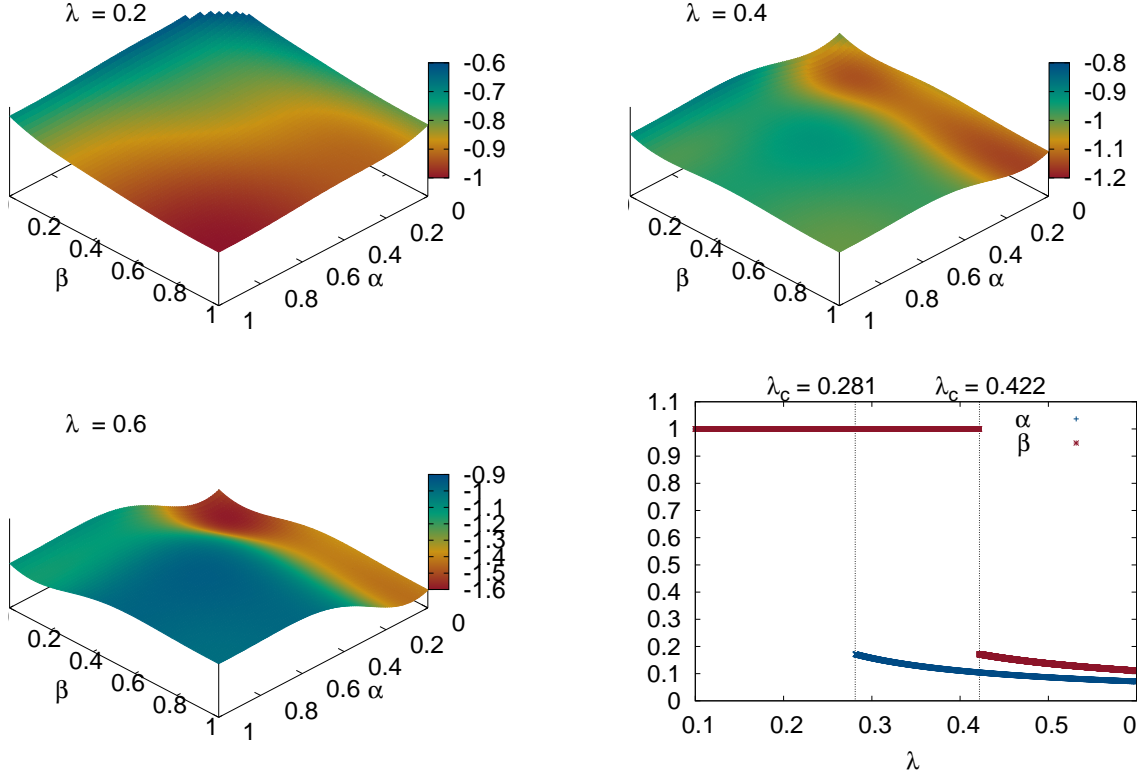
Figure 7.12: Variational energy per site for the mixed field case as a function of two variational parameters α and β for the case where $\lambda_z = \lambda$ and $\lambda_x = 1.5 \cdot \lambda$. One can see that the global minimum is at $\alpha = \beta = 1$ for $\lambda = 0.2$. Hence, both systems are in the fracton phase. For $\lambda = 0.4$, λ_x is already above the critical value for the phase transition, while the λ_z is below it. This results in the global energy minimum being $\alpha \approx 0.2$ and $\beta = 1$. Hence the μ-spins are already in the polarized phase while the σ-spins are still in the topological phase. For $\lambda = 0.6$ both $\alpha \approx 0.2$ and $\beta \approx 0.2$, which indicates that both spin are in the polarized phase. The bottom left shows the α and β values of the global minimum as a function of λ. As expected there are two first-order phase transitions. One for $\lambda_x \approx 0.422$ and one for $\lambda_z \approx 0.422$.

the low- and high-field solution. The low-field solution is

$$\epsilon_{B,\sigma,\mathrm{LF}} = \langle 0| \frac{\hat{\mathcal{H}}_{B,\sigma,\mathrm{eff}}}{2JN_c} |0\rangle = -\frac{1}{2} - \lambda_x^2 \frac{1}{4} - \lambda_x^4 \frac{3}{64} - \lambda_x^6 \frac{559}{15360} + O(\lambda_x^8), \tag{7.24}$$

where $\lambda_x = \frac{h_{\mu,x}}{2J}$. The treatment of high-field case already in the same units as the low-field case yields

$$\epsilon_{B,\sigma,\mathrm{HF}} = \langle 0| \frac{\hat{\mathcal{H}}_{B,\sigma,\mathrm{eff}}}{2JN_c} |0\rangle = 2\lambda_x \left(-\frac{1}{2} - \left(\frac{1}{4\lambda_x}\right)^2 \frac{1}{4} - \left(\frac{1}{4\lambda_x}\right)^4 \frac{3}{64} - \left(\frac{1}{4\lambda_x}\right)^6 \frac{559}{15360} \right) + O(\lambda_x^{-8}). \tag{7.25}$$

As already established in section 7.1.3, the phase transition is a first-order phase transition at $h_{\mu,x} = J \Leftrightarrow \lambda_x = 0.5$.

The results for $\hat{\mathcal{H}}_{A,\mu}$ are identical, due to the symmetry of $\hat{A}_c$ and $\hat{B}_c$ operators. Hence, the
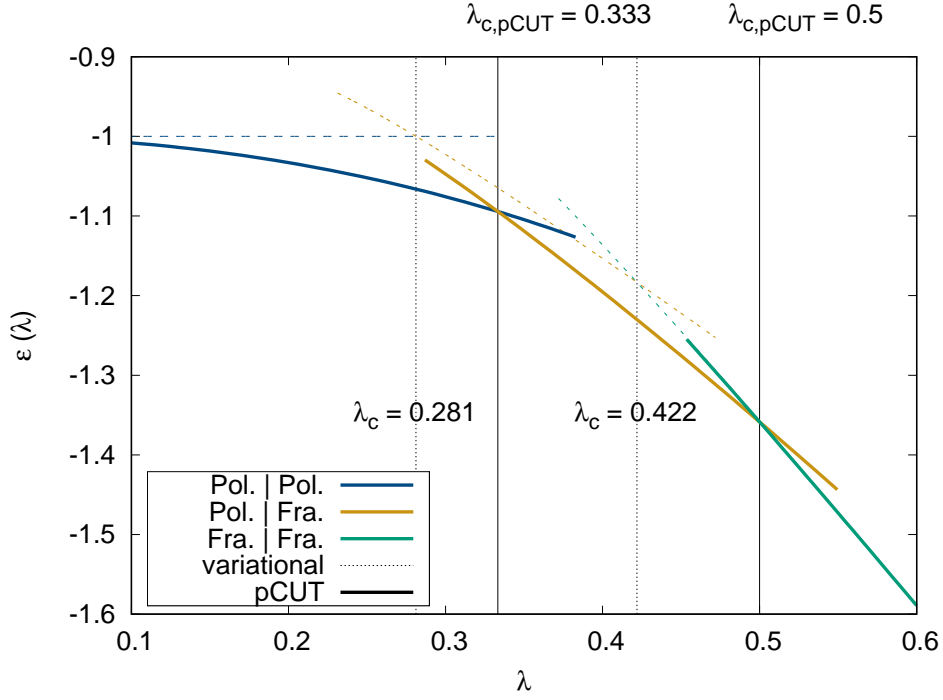
Figure 7.13: Variational energy per state as a function of λ for the case that $\lambda_z = \lambda$ and $\lambda_x = 1.5 \cdot \lambda$. The dotted lines are the variational energies and the solid lines the pCUT results. For both cases we ca see two first-order phase transitions. Each happens when either λ_z or λ_x cross their critical value of 0.422 for the variational ansatz and 0.5 for the ground-states energies obtained by pCUT.

low-field solution is

$$\epsilon_{A,\mu,\mathrm{LF}} = \langle 0| \frac{\hat{\mathcal{H}}_{A,\mu,\mathrm{eff}}}{2JN_c} |0\rangle = -\frac{1}{2} - \lambda_z^2 \frac{1}{4} - \lambda_z^4 \frac{3}{64} - \lambda_z^6 \frac{559}{15360} + O(\lambda_z^8), \tag{7.26}$$

with $\lambda_z = \frac{h_{\sigma,z}}{2J}$. Similarly,

$$\epsilon_{A,\mu,\mathrm{HF}} = \langle 0| \frac{\hat{\mathcal{H}}_{A,\mu,\mathrm{eff}}}{2JN_c} |0\rangle = 2\lambda_z \left(-\frac{1}{2} - \left(\frac{1}{4\lambda_z}\right)^2 \frac{1}{4} - \left(\frac{1}{4\lambda_z}\right)^4 \frac{3}{64} - \left(\frac{1}{4\lambda_z}\right)^6 \frac{559}{15360} \right) + O(\lambda_z^{-8}). \tag{7.27}$$

and the first-order phase transition is at $h_{\sigma,z} = J \Leftrightarrow \lambda_z = 0.5$.

The energy for the whole system is the the sum of both systems. That means that we have two first-order phase transitions at the lines where $\lambda_x = 0.5$ or $\lambda_z = 0.5$. The phase diagram is shown in figure 7.14.

In order to compare pCUT and the variational calculations, we consider the case with $\lambda_z = \lambda$ and $\lambda_x = 1.5 \cdot \lambda$. For $\lambda < \frac{0.5}{1.5}$ both systems are in the fracton phase and $\epsilon = \epsilon_{A,\mu,\mathrm{LF}} + \epsilon_{B,\sigma,\mathrm{LF}}$. After the phase transition $\frac{0.5}{1.5} < \lambda < 0.5$ of the μ-spins, this changes to $\epsilon = \epsilon_{A,\mu,\mathrm{HF}} + \epsilon_{B,\sigma,\mathrm{LF}}$. For $\lambda > 0.5$ both systems are in the polarized phase and we get $\epsilon = \epsilon_{A,\mu,\mathrm{HF}} + \epsilon_{B,\sigma,\mathrm{HF}}$. This can be seen in figure 7.13.
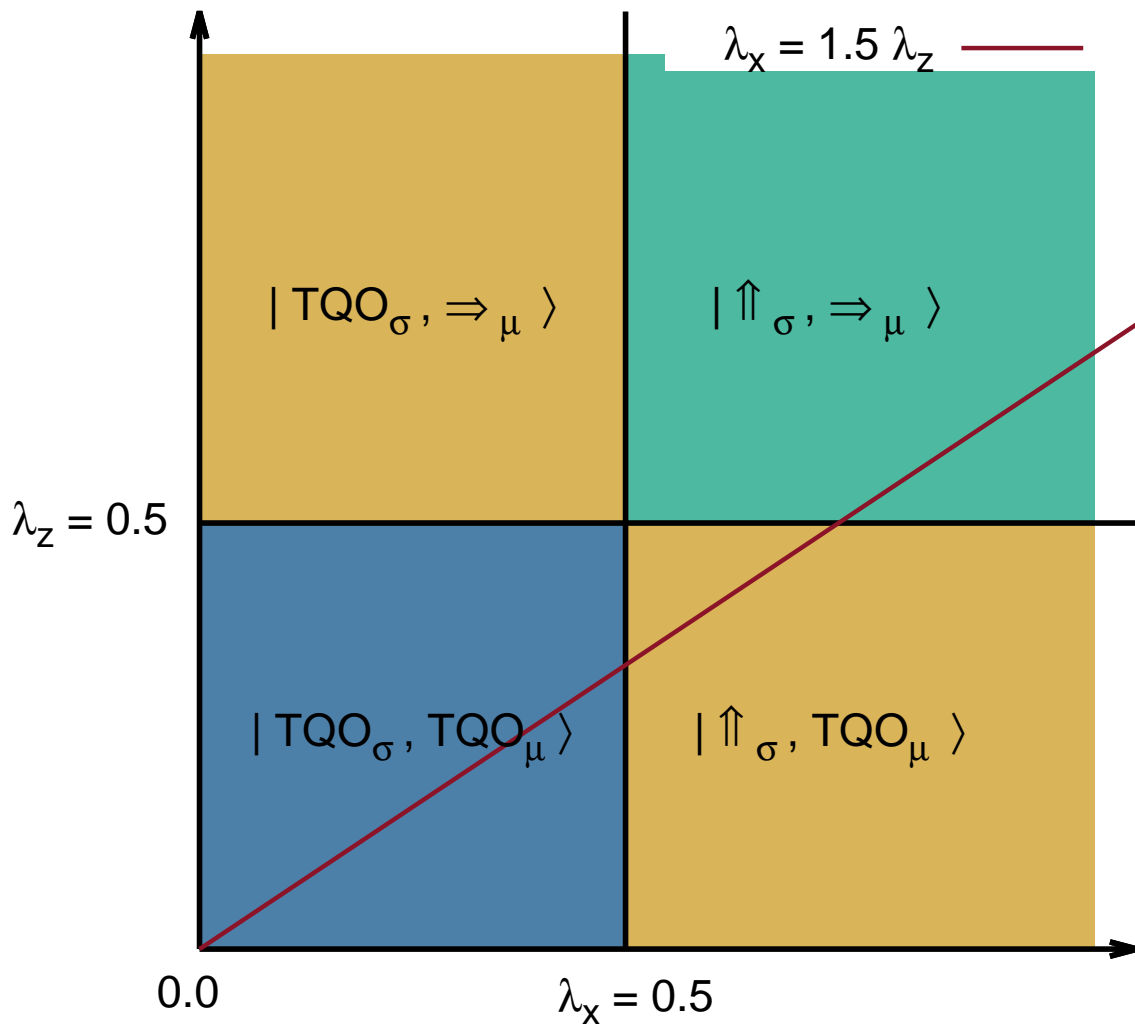
Figure 7.14: Phase diagram of the mixed-field case. As the mixed field can be written as two completely independent subsystems, there are two independent phase transitions. One when $\lambda_z = 0.5$ and on when $\lambda_x = 0.5$. The red line indicates the case considered in figures 7.12 and 7.13.

Chapter 8

Fracton excitations

In chapter 7, we investigated the phase transition between the two phases by studying the ground-states energies. This is only legitimate if there is no additional phase transition into an intermediate phase. A possible mechanism that could drive such a phase transition is a closing of the energy gap for an excitation. In order to rule out that a second-order phase transition taking place before the observed first-order phase transition, we investigate the energy of the fractons. We consider the single-field and the two-field case. For both cases, we investigate the one quasi-particle and two quasi-particle excitations in the fracton phase.

8.1 Single-field case

In this section we use pCUT to investigate the energies of excitations in the single-field case. As already argued in section 6.1, it is sufficient to investigate the case where the μ-field is zero and the σ-field points in z-direction. The Hamiltonian derived in 6.17 is

$$\frac{\hat{\mathcal{H}}}{2J} = -N_c + \hat{Q} - \lambda \left(\hat{T}_{\sigma,+4} + \hat{T}_{\sigma,+2} + \hat{T}_{\sigma,0} + \hat{T}_{\sigma,-2} + \hat{T}_{\sigma,-4} \right),$$

where $\lambda = \frac{h}{2J}$ is the perturbative parameter.

In the following we will investigate the single- and two quasi-particle block of the effective Hamiltonian.

8.1.1 One quasi-particle excitations

We already argued in section 3.6 and 4.4 that single fractons are fundamentally immobile. That means that all off-diagonal hooping elements are zero, which we also verified with computer aid up to sixth order. Due to the translational invariance, all diagonal entries are equal. The effective Hamiltonian then reads

$$\hat{\mathcal{H}}_{\text{eff}} = C \sum_{\mathbf{j}} \hat{b}_{\mathbf{j}}^{\dagger} \hat{b}_{\mathbf{j}},$$

where C is the value of the local hopping. In momentum space this is

$$\hat{\mathcal{H}}_{\text{eff}} = C \sum_{\mathbf{j}} \hat{b}_{\mathbf{j}}^{\dagger} \hat{b}_{\mathbf{j}} = C(2\pi)^{-3} \sum_{\mathbf{j}} \sum_{\mathbf{k},\mathbf{k}'} e^{i m \mathbf{j}(\mathbf{k}-\mathbf{k}')} \hat{b}_{\mathbf{k}}^{\dagger} \hat{b}_{\mathbf{k}'} = C \sum_{\mathbf{k}} \hat{b}_{\mathbf{k}}^{\dagger} \hat{b}_{\mathbf{k}'}$$

where $\hat{b}_{\mathbf{k}}$ and $\hat{b}_{\mathbf{k}}^{\dagger}$ are the creation an annihilation operators of a fracton with momentum $\mathbf{k}$. For the above equation one can directly see that the dispersion is flat.

Because of the flat dispersion, we just have to evaluate

$$C = \left\langle \blacksquare_i \left| \frac{\hat{\mathcal{H}}_{\text{eff}}}{2J} \right| \blacksquare_i \right\rangle,$$

where $\left| \blacksquare_i \right\rangle$ is the state with an excited $\hat{B}_c$ in cube i. By applying the general formula for pCUT in equation 5.6 in 6.17 we get

$$\frac{\hat{\mathcal{H}}_{\text{eff}}^{(0)}}{2J} = -N_c + \hat{Q} \tag{8.1}$$

$$\frac{\hat{\mathcal{H}}_{\text{eff}}^{(1)}}{2J} = \lambda C(0)\hat{T}_0 \tag{8.2}$$

$$\frac{\hat{\mathcal{H}}_{\text{eff}}^{(2)}}{2J} = \lambda^2 \sum_{n=0}^{2} \frac{1}{2n} \left[\hat{T}_{2n}, \hat{T}_{-2n} \right], \tag{8.3}$$

where $\frac{\hat{\mathcal{H}}_{\text{eff}}^{(n)}}{2J}$ is the nth order expansion. We now evaluate the zeroth, first and second order explicitly. In the following, we consider a infinite cubic lattice with N_c cubes as the cluster. We have to be careful here, because the evaluation of the $\hat{T}$ operator sequence on the cluster also includes vacuum fluctuations that are not linked to the processes including the fracton in c. Hence, we will do the calculation on the cluster including vacuum fluctuations denoted by and then subtract the vacuum energy on the same cluster. For the explicit calculation we can use the vacuum energies we already calculated in chapter 7. However, for the computer aided results we have to evaluate the vacuum energy on the optimized cluster and subtract this from the results on the very same cluster. In the following we explicitly calculate the first two orders before we do a computer aided calculation.

Explicit calculation

For the zeroth order we get

$$\left\langle \square_i \left| \frac{\hat{\mathcal{H}}_{\text{eff}}^{(0)}}{2J} \right| \square_i \right\rangle = \left\langle \square_i \left| -N_c + \hat{Q} \right| \square_i \right\rangle_c = -N_c + 1.$$

In the first order we have

$$\left\langle \square_i \left| \frac{\hat{\mathcal{H}}_{\text{eff}}^{(1)}}{2J} \right| \square_i \right\rangle = \left\langle \square_i \left| \lambda C(0)\hat{T}_0 \right| \square_i \right\rangle = 0,$$

because the $\hat{T}_0$ operator only give a non-zero contribution if it act on a state with two fractons. As we act on a state with just one fracton, this is not possible in first order.

For the second order we evaluate all $\hat{T}$ operator sequences separately. The sequences that do not contribute are

$$\left\langle \square_i \left| \hat{T}_{+4}\hat{T}_{-4} \right| \square_i \right\rangle = 0,$$

$$\left\langle \square_i \left| \hat{T}_{+2}\hat{T}_{-2} \right| \square_i \right\rangle = 0.$$

70

The reason for this is that $\hat{T}_0$, $\hat{T}_{-2}$ and $\hat{T}_{-4}$ only give a non-zero contribution if they act on state with more than one quasi-particle. As in the above sequences all of these operators act on an one quasi-particle state, these expressions give no contribution.

The next sequence is

$$\left\langle \text{[diagram]}_i \middle| \hat{T}_{-4}\hat{T}_4 \middle| \text{[diagram]}_i \right\rangle = \left\langle \text{[diagram]}_i \middle| \hat{T}_{-4} \sum_j \hat{\tau}_{+4,j} \middle| \text{[diagram]}_i \right\rangle = \left\langle \text{[diagram]}_i \middle| \hat{T}_{-4} \sum_{\hat{b}_i \notin \hat{\tau}_j} \middle| \text{[diagram]}_i, \text{[diagram]}_j \right\rangle,$$

where $\left| \text{[diagram]}_i, \text{[diagram]}_j \right\rangle$ is the state, where the original excitation in s is still present and we have four additional excitations in the pattern [diagram] around a vertex j. As i is explicitly not in this pattern, there are $(N_c - 4)$ states $\left| \text{[diagram]}_i, \text{[diagram]}_j \right\rangle$. The next step is

$$\left\langle \text{[diagram]}_i \middle| \hat{T}_{-4} \sum_{\hat{b}_i \notin \hat{\tau}_j} \middle| \text{[diagram]}_i, \text{[diagram]}_j \right\rangle = \left\langle \text{[diagram]}_i \middle| \sum_k \hat{\tau}_{-4,k} \sum_{\hat{b}_i \notin \hat{\tau}_j} \middle| \text{[diagram]}_i, \text{[diagram]}_j \right\rangle$$

$$= (N_c - 4)\left\langle \text{[diagram]}_i \middle| \text{[diagram]}_i \right\rangle = N_c - 4,$$

where the only $\hat{\tau}_{-4,k}$ operators that contribute are the ones that annihilate the four excitations created by $\hat{\tau}_{+4,j}$ in the step before.

The last non-zero sequence is

$$\left\langle \text{[diagram]}_i \middle| \hat{T}_{-2}\hat{T}_2 \middle| \text{[diagram]}_i \right\rangle = \left\langle \text{[diagram]}_i \middle| \hat{T}_{-2} \sum_j \hat{\tau}_{-2,i} \middle| \text{[diagram]}_i \right\rangle =$$

$$= \left\langle \text{[diagram]}_i \middle| \hat{T}_{-2} \left(\middle| \text{[diagram]}_i \right\rangle + \middle| \text{[diagram]}_i \right\rangle + \middle| \text{[diagram]}_i \right\rangle + \middle| \text{[diagram]}_i \right\rangle \right)$$

$$= 4 \cdot \left\langle \text{[diagram]}_i \middle| \text{[diagram]}_i \right\rangle = 4.$$

Here we have four options to act with a $\hat{T}_{+2}$ operator on the one-particle state.

Gathering all of the contributions the second order we get

$$\left\langle \text{[diagram]}_i \middle| \frac{\hat{\mathcal{H}}_{\text{eff}}^{(2)}}{2J} \middle| \text{[diagram]}_i \right\rangle = -\frac{1}{4}(N_c - 4) - \frac{1}{2} \cdot 4.$$

That means in all orders we have

$$\left\langle \text{[diagram]}_i \middle| \frac{\hat{\mathcal{H}}_{\text{eff}}}{2J} \middle| \text{[diagram]}_i \right\rangle = -N_c + 1 - \lambda^2 \left(-\frac{1}{4}(N_c - 4) - \frac{1}{2} \cdot 4 \right) + O(\lambda^3). \tag{8.4}$$

However, this still includes the vacuum fluctuations. In order to get the isolated contribution of the excitation we have to subtract the vacuum energy up to third order. Using the expression in equation 7.3 we get

$$\left\langle \text{[diagram]}_i \middle| \frac{\hat{\mathcal{H}}_{\text{eff}}}{2J} \middle| \text{[diagram]}_i \right\rangle = \left\langle \text{[diagram]}_i \middle| \frac{\hat{\mathcal{H}}_{\text{eff}}}{2J} \middle| \text{[diagram]}_i \right\rangle - \left\langle \text{[diagram]} \middle| \frac{\hat{\mathcal{H}}_{\text{eff}}}{2J} \middle| \text{[diagram]} \right\rangle$$

$$= 1 - \lambda^2 + O(\lambda^3) \tag{8.5}$$

Computer aided calculation

For the computer aided calculation, we construct the minimal cluster with the method described in section 5.1.5.

The result is

$$\left\langle \blacksquare_i \left| \frac{\hat{\mathcal{H}}_{\text{eff}}}{2J} \right| \blacksquare_i \right\rangle = 1 - \lambda^2 - \frac{5}{16}\lambda^4 - \frac{775}{1152}\lambda^6 + O(\lambda^8). \tag{8.6}$$

We plot and discuss the implication of this result in section 8.1.3.

8.1.2   Two quasi-particle block

In this chapter we consider the two quasi-particle block. A general state in this regime depends on the two positions $\mathbf{r}_1$ and $\mathbf{r}_2$ of the fractons. That means we have to consider all states $|2QP, \mathbf{r}_1, \mathbf{r}_2\rangle$. However, we can also define the state by the position of the center of mass $\mathbf{R} = \frac{\mathbf{r}_1 + \mathbf{r}_2}{2}$ and the relative position $\mathbf{d} = \frac{\mathbf{r}_1 - \mathbf{r}_2}{2}$. The energies of the systems cannot depend on the center of mass, because the problem is translational invariant and the locality of possible processes in Haah's code. Hence, we can restrict us to the treatment of the relative positions. That means, we are left with a state $|2QP, \mathbf{d}\rangle$. In general, this is an infinite matrix. However, due to the immobility of the fractons, we only have local processes. These can be classified as follows. The vast majority of configurations cannot be transformed to a different state by the terms in $\hat{\mathcal{H}}_{\text{eff}}$. Hence, the only non-zero entry in the matrix for these states are the diagonal elements. These contribution have a flat dispersion, similar to the single-particle case. Configurations that can be transformed to a different configuration are the hooping terms already identified in section 4.4. These form a finite matrix, that we will diagonalize in the position space and are back with diagonal entries with a flat dispersion. We start with these hopping terms.

For the energetic contribution of the hopping terms we want to diagonalize the matrix

$$\begin{pmatrix} \left\langle \boxplus \left| \frac{\hat{\mathcal{H}}_{\text{eff}}}{2J} \right| \boxplus \right\rangle & \left\langle \boxplus \left| \frac{\hat{\mathcal{H}}_{\text{eff}}}{2J} \right| \boxplus \right\rangle \\[2ex] \left\langle \boxplus \left| \frac{\hat{\mathcal{H}}_{\text{eff}}}{2J} \right| \boxplus \right\rangle & \left\langle \boxplus \left| \frac{\hat{\mathcal{H}}_{\text{eff}}}{2J} \right| \boxplus \right\rangle \end{pmatrix}.$$

Instead of doing the calculations explicitly, we directly give the results of the computer aided evaluation. For the interested reader, the relevant sequences can be found in appendix A. The results for the contributing matrix elements are

$$\left\langle \boxplus \left| \frac{\hat{\mathcal{H}}_{\text{eff}}}{2J} \right| \boxplus \right\rangle = \lambda - \frac{3}{8}\lambda^3 - \frac{1553}{2304}\lambda^5 + O(\lambda^7),$$

$$\left\langle \boxplus \left| \frac{\hat{\mathcal{H}}_{\text{eff}}}{2J} \right| \boxplus \right\rangle = 2 - \frac{5}{4}\lambda^2 - \frac{241}{192}\lambda^4 - \frac{558043}{276480}\lambda^6 + O(\lambda^8),$$

$$\left\langle \boxplus \left| \frac{\hat{\mathcal{H}}_{\text{eff}}}{2J} \right| \boxplus \right\rangle = 2 - \frac{5}{4}\lambda^2 - \frac{241}{192}\lambda^4 - \frac{558043}{276480}\lambda^6 + O(\lambda^8).$$

We diagonalized the hopping matrix numerically for certain values of λ and get the binding and anti-binding solutions plotted in figure 8.1.

For the remaining diagonal elements the results differ depending on the configuration of the two excitations. If two excitations are far away from each other, they behave like two independent quasi-particles. Conversely, they can interact in configurations where the fractons are close to

each other. We consider all cases with two excitations at relative position $\mathbf{d} = (d_x, d_y, d_z)^T$ in sixth order. Note that all excitations with $d_i > 3$ with $i \in (x, y, z)$ are automatically not linked, because the fractons are too far away for a $\hat{T}_{\sigma,n}$ operator sequence in sixth order to touch both excitations. Hence, the energy correction of these configurations is twice the energy correction of a single particle. All results are given in table 8.1.1. For a distance relative position $\mathbf{d} = (a, b, c)^T$, all positions that are permutations of a, b and c yield the same result. This is due to the symmetry of the $\hat{T}_{\sigma,n}$ operators. Furthermore, the results for all distances $\mathbf{d} = (a, b, c)^T$ with $a + b + c$ being odd number are two times the single-particle energy. This makes sense as the $\hat{T}_{\sigma,n}$ operators can only link excitations in a checkerboard pattern. If an excitation is in one of the vacancies of the checkerboard pattern originating from the other excitation, the processes are not linked. In second order, all configurations are not linked, where the two fractons are more than one site away from each other. Therefore, these configurations are independent in second order. As a result, the energy correction in second order is two times the energy of a single particle. The same is true for $d_i > 2$ for direction i in fourth order and for $d_i > 3$ in sixth order. The result for the distance $(1, 1, 0)^T$ and all permutations are diagonal elements of the configurations that allow for hopping discussed above. All of the above results together are shown in figure 8.1 forming the two-particle continuum. We discuss the physical interpretation in the next section.

distance d	function
$(1, 1, 0)^T$	$2 - \frac{5}{4}\lambda^2 - \frac{241}{192}\lambda^4 - \frac{558043}{276480}\lambda^6$
$(2, 0, 0)^T$	$2 - 2\lambda^2 - \frac{31}{24}\lambda^4 - \frac{559}{480}\lambda^6$
$(1, 1, 2)^T$	$2 - 2\lambda^2 - \frac{23}{24}\lambda^4 - \frac{210211}{138240}\lambda^6$
$(2, 2, 0)^T$	$2 - 2\lambda^2 - \frac{19}{24}\lambda^4 - \frac{216463}{138240}\lambda^6$
$(3, 3, 0)^T$	$2 - 2\lambda^2 - \frac{5}{8}\lambda^4 - \frac{75301}{55296}\lambda^6$
$(0, 1, 3)^T$	$2 - 2\lambda^2 - \frac{5}{8}\lambda^4 - \frac{27503}{18432}\lambda^6$
$(2, 1, 3)^T$	$2 - 2\lambda^2 - \frac{5}{8}\lambda^4 - \frac{8567}{6144}\lambda^6$
$(2, 2, 2)^T$	$2 - 2\lambda^2 - \frac{5}{8}\lambda^4 - \frac{13301}{9216}\lambda^6$
rest	$2 - 2\lambda^2 - \frac{5}{8}\lambda^4 - \frac{775}{576}$

Table 8.1.1: Table of the energies for configurations with two excitations separated by the distance **d** as a function of λ for the low-field limit of the single-field case. The distances given in the table are representatives of distances that give identical contributions due to symmetries. The processes are unlinked in second order for larger distances than one site in each direction. Hence, the energy correction for these processes is two times the energy correction for the single particle regime. This holds for configurations with $d_i > 2$ in fourth order and for $d_i > 3$ in sixth order for for any direction i.

8.1.3 Discussion

Figure 8.1 shows the single-particle energies and the two-particle energies of the single-field case for $\lambda < 0.5$. The one-particle contribution shows a lowering of the energy due to the magnetic field. However, it is far from closing the excitation gap. Hence, we can rule out a second-order phase transition driven by single particle energies. For the two-particle regime, we have the two particle continuum with all possible corrections in sixth order, a binding and an anti-binding contribution. The configurations in the continuum lower their energy in a similar rate than the
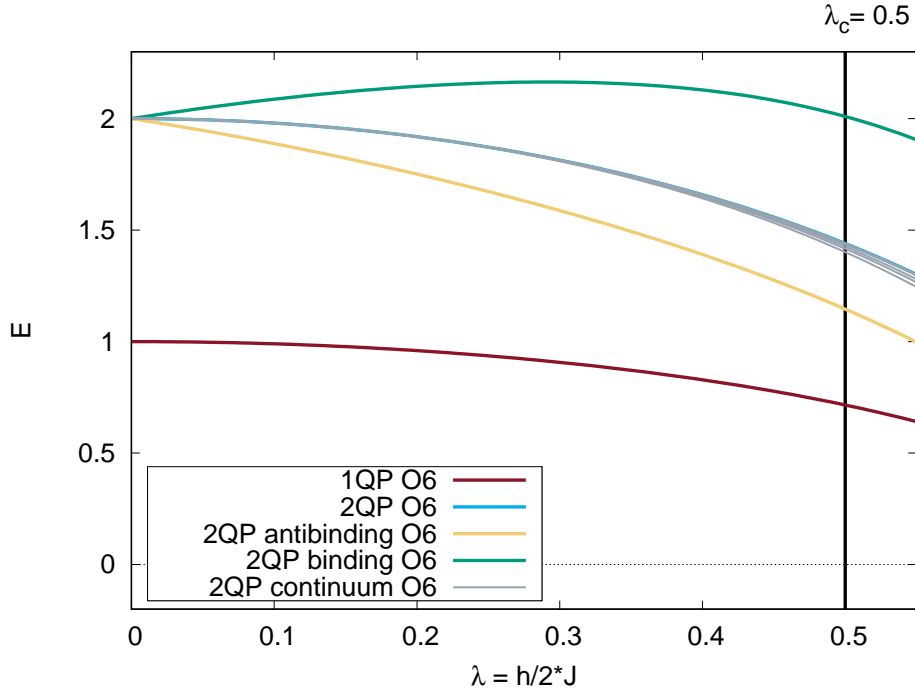
Figure 8.1: All Energies E of the one and two particle block as function of $\lambda = \frac{h}{2J}$ in the fracton phase of the single-field cases up to sixth order. Single fractons are immobile. Therefore, we have a single contributing energy with a flat dispersion. For two excitations and varying distances between the fractons, we get only slight variation to the case of two independent terms. The diagonalized hopping terms yield a binding and anti-binding particles. We find no evidence of a level crossings or a closing of the gap for both the one- and two-particle regime. This excludes a second-order phase transition.

single-particle case. The energy of the anti-bonding term is always lower than the continuum, but never crosses the single particle energy. Hence, the two-particle block shows no signs of a second-order phase transition.

As the single-field case is self dual, an extrapolation of the one- and two-particle energies in the high-field limit yields the same results. In conclusion we find no evidence for a second-order phase transition in the low- and high-field limit.

8.2 Two-field case

In this section use pCUT to investigate the fracton excitations in the two-field case. As already argued in section 6.1, it is sufficient to investigate the case where the μ-field and σ-field are finite and point in z-direction. The Hamiltonian derived in 6.14 is

$$
\begin{aligned}
\frac{\hat{\mathcal{H}}}{2J} \;=\; & -N_c + \hat{Q} - \lambda\Big(\hat{T}_{\sigma^z,+4} + \hat{T}_{\sigma^z,+2} + \hat{T}_{\sigma^z,0} + \hat{T}_{\sigma,-2} + \hat{T}_{\sigma^z,-4} \\
& + \hat{T}_{\mu^z,+4} + \hat{T}_{\mu^z,+2} + \hat{T}_{\mu^z,0} + \hat{T}_{\mu^z,-2} + \hat{T}_{\mu^z,-4}\Big).
\end{aligned}
$$

where $\lambda = \frac{h_z}{2J}$.

Similar to the single-field case, we investigate the one and two quasi-particle block.

8.2.1 One quasi-particle excitations

Due to the fractal character of the $\hat{T}_{\sigma^z,+4}$ and $\hat{T}_{\mu^z,+4}$ operators, single excitations cannot move. As argued in section 8.1.1, we therefore have a flat dispersions and is sufficient to calculate a single matrix element. The explicit calculation up to second order is given in apprendix A.

The results for a computer aided calculation are

$$
\left\langle \blacksquare_i \left| \frac{\hat{\mathcal{H}}_{\text{eff}}}{2J} \right| \blacksquare_i \right\rangle = 1 - 2\lambda^2 - \frac{57}{16}\lambda^4 - \frac{10297}{768}\lambda^6 + O(\lambda^8). \tag{8.7}
$$

In figure 8.2, this energy is plotted. We discuss the physical implications in section 8.2.3. Similar, to the single-field case, we explicitly checked immobility of fractons up to sixth order with pCUT.

8.2.2 Two quasi-particle dynamics

In contrast to the single-field case, we now have a non-diagonal 3×3 matrix for the the hopping terms. It consists of hopping processes discussed in section 4.4. Hence, we have to diagonalize the matrix

$$
\begin{pmatrix}
\left\langle \left| \frac{H_{\text{eff}}}{2J} \right| \right\rangle & \left\langle \left| \frac{H_{\text{eff}}}{2J} \right| \right\rangle & 0 \\[12pt]
\left\langle \left| \frac{H_{\text{eff}}}{2J} \right| \right\rangle & \left\langle \left| \frac{H_{\text{eff}}}{2J} \right| \right\rangle & \left\langle \left| \frac{H_{\text{eff}}}{2J} \right| \right\rangle \\[12pt]
0 & \left\langle \left| \frac{H_{\text{eff}}}{2J} \right| \right\rangle & \left\langle \left| \frac{H_{\text{eff}}}{2J} \right| \right\rangle
\end{pmatrix}. \tag{8.8}
$$

The results for these matrix elements are

$$\left\langle \blacksquare \left| \frac{H_{\text{eff}}}{2J} \right| \blacksquare \right\rangle \;=\; 2 - \frac{13}{4}\lambda^2 - \frac{661}{96}\lambda^4 - \frac{15933427}{552960}\lambda^6 + O\!\left(\lambda^8\right) \tag{8.9}$$

$$\left\langle \blacksquare \left| \frac{H_{\text{eff}}}{2J} \right| \blacksquare \right\rangle \;=\; 2 - \frac{5}{2}\lambda^2 - \frac{365}{48}\lambda^4 - \frac{3895117}{110592}\lambda^6 + O\!\left(\lambda^8\right) \tag{8.10}$$

$$\left\langle \blacksquare \left| \frac{H_{\text{eff}}}{2J} \right| \blacksquare \right\rangle \;=\; 2 - \frac{13}{4}\lambda^2 - \frac{383}{48}\lambda^4 - \frac{3180593}{92160}\lambda^6 + O\!\left(\lambda^8\right) \tag{8.11}$$

$$\left\langle \blacksquare \left| \frac{H_{\text{eff}}}{2J} \right| \blacksquare \right\rangle \;=\; \lambda - 3\lambda^3 - \frac{1837}{32}\lambda^5 + O\!\left(\lambda^7\right) \tag{8.12}$$

$$\left\langle \blacksquare \left| \frac{H_{\text{eff}}}{2J} \right| \blacksquare \right\rangle \;=\; \lambda - 3\lambda^3 - \frac{513}{8}\lambda^5 + O\!\left(\lambda^7\right). \tag{8.13}$$

The explicit calculation of the leading orders for all of the above cases are given in appendix A. Diagonalizing this matrix numerically yields the anti-binding and anti-binding curves in figure 8.2.

Similar to the single-field case we calculated the energy of all configurations with two fractons at a relative position $\mathbf{d} = (d_x, d_y, d_z)^T$. The contributions are given in table 8.2.1. The structure of the results is similar to the single-field case. For larger distance than one site in each direction, the processes are unlinked in second order. Hence, the energy correction for these processes is two times the energy correction for the single-particle regime. This also holds for configurations with excitations that are separated by more than two sites in fourth order and configurations with excitations that are separated by more than three site in sixth order. All configurations with linked processes lower the energy faster than the unlinked ones. All of these contributions form the two particle continuum in figure 8.2. We discuss the results in the following chapter.

8.2.3 Discussion

Figure 8.2 shows the one and two-fracton excitation energies of the two-field case for $\lambda < 0.223$. For the single-particle energies we have a single curve that shows the expected lowering of the energy in the magnetic field. However, there is no closing of the gap before the phase transition. In the two-fracton block we find the two-particle continuum containing all possible corrections in sixth order. The hopping terms give rise to binding and anti-binding contributions. The continuum as well as the anti-binding term are far from closing the energy gap before the phase transition. Hence, we find no evidence for a second-order phase transition the energetics of the fracton excitations.

distance d	function	distance d	function
$(0,1,1)^T$	$2 - \frac{13}{4}\lambda^2 - \frac{383}{48}\lambda^4 - \frac{3180593}{92160}\lambda^6$	$(0,0,1)^T$	$2 - \frac{13}{4}\lambda^2 - \frac{661}{96}\lambda^4 - \frac{15933427}{552960}\lambda^6$
$(0,1,-1)^T$	$2 - \frac{5}{2}\lambda^2 - \frac{365}{48}\lambda^4 - \frac{3895117}{110592}\lambda^6$	$(1,1,1)^T$	$2 - 4\lambda^2 - \frac{65}{8}\lambda^4 - \frac{370123}{11520}\lambda^6$
$(-1,1,2)^T$	$2 - 4\lambda^2 - \frac{187}{24}\lambda^4 - \frac{8509729}{276480}\lambda^6$	$(0,1,-2)^T$	$2 - 4\lambda^2 - \frac{187}{24}\lambda^4 - \frac{2057831}{69120}\lambda^6$
$(0,2,-2)^T$	$2 - 4\lambda^2 - \frac{187}{24}\lambda^4 - \frac{417361}{13824}\lambda^6$	$(0,1,2)^T$	$2 - 4\lambda^2 - \frac{179}{24}\lambda^4 - \frac{345181}{11520}\lambda^6$
$(1,1,2)^T$	$2 - 4\lambda^2 - \frac{179}{24}\lambda^4 - \frac{2678513}{92160}\lambda^6$	$(1,1,-1)^T$	$2 - 4\lambda^2 - \frac{707}{96}\lambda^4 - \frac{285163}{9216}\lambda^6$
$(0,2,2)^T$	$2 - 4\lambda^2 - \frac{175}{24}\lambda^4 - \frac{645101}{23040}\lambda^6$	$(0,0,2)^T$	$2 - 4\lambda^2 - \frac{691}{96}\lambda^4 - \frac{668009}{23040}\lambda^6$
$(1,1,-2)^T$	$2 - 4\lambda^2 - \frac{225}{32}\lambda^4 - \frac{1291783}{46080}\lambda^6$	$(0,1,-3)^T$	$2 - 4\lambda^2 - \frac{57}{8}\lambda^4 - \frac{86275}{3072}\lambda^6$
$(0,2,3)^T$	$2 - 4\lambda^2 - \frac{57}{8}\lambda^4 - \frac{495157}{18432}\lambda^6$	$(0,2,-3)^T$	$2 - 4\lambda^2 - \frac{57}{8}\lambda^4 - \frac{124465}{4608}\lambda^6$
$(0,3,3)^T$	$2 - 4\lambda^2 - \frac{57}{8}\lambda^4 - \frac{1483669}{55296}\lambda^6$	$(0,3,-3)^T$	$2 - 4\lambda^2 - \frac{57}{8}\lambda^4 - \frac{186247}{6912}\lambda^6$
$(0,0,3)^T$	$2 - 4\lambda^2 - \frac{57}{8}\lambda^4 - \frac{1516073}{55296}\lambda^6$	$(0,1,3)^T$	$2 - 4\lambda^2 - \frac{57}{8}\lambda^4 - \frac{1512469}{55296}\lambda^6$
$(1,1,3)^T$	$2 - 4\lambda^2 - \frac{57}{8}\lambda^4 - \frac{248029}{9216}\lambda^6$	$(1,1,-3)^T$	$2 - 4\lambda^2 - \frac{57}{8}\lambda^4 - \frac{378793}{13824}\lambda^6$
$(1,2,2)^T$	$2 - 4\lambda^2 - \frac{57}{8}\lambda^4 - \frac{498761}{18432}\lambda^6$	$(-1,2,2)^T$	$2 - 4\lambda^2 - \frac{57}{8}\lambda^2 - \frac{1517875}{55296}\lambda^6$
$(-1,2,-2)^T$	$2 - 4\lambda^2 - \frac{57}{8}\lambda^4 - \frac{129863}{4608}\lambda^6$	$(1,2,-3)^T$	$2 - 4\lambda^2 - \frac{57}{8}\lambda^4 - \frac{23843}{864}\lambda^6$

Table 8.2.1: Table of the energies for configurations with two excitations separated by the distance **d** as a function of λ for the low-field limit of the two-field case. The distances given in the table are representatives of distances that give identical contributions due to symmetries. For larger distances than one site in each direction, the processes are unlinked in second order. Hence, the energy correction for these processes is two times the energy correction for the single-particle regime. This holds for configurations with excitations that are separated by more than two sites in fourth order and configurations with excitations that are separated by more than three sites in sixth order.
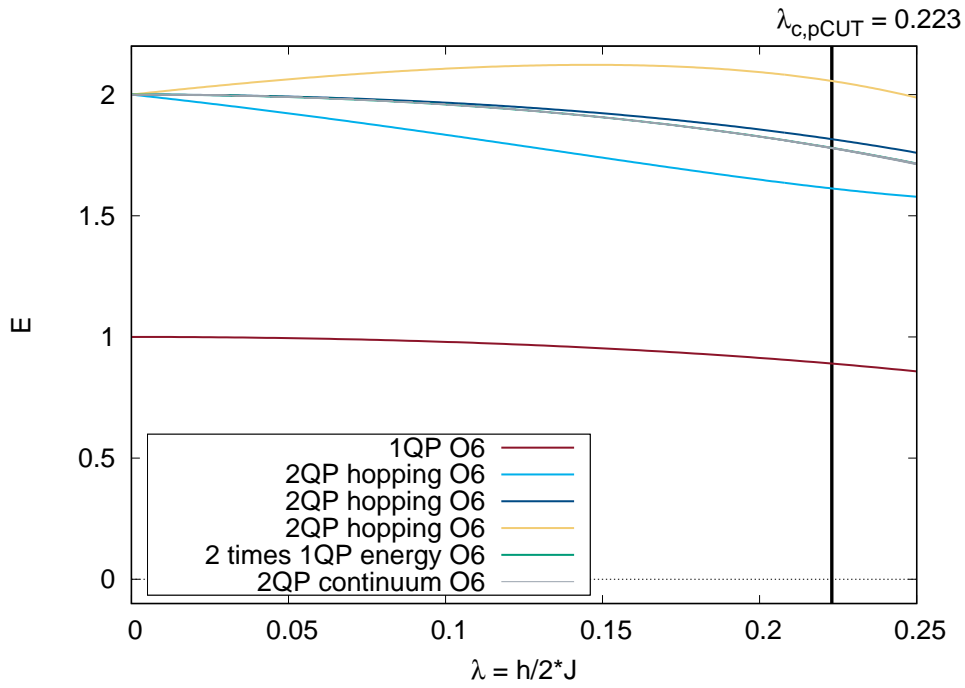
Figure 8.2: All single- and two-fracton energies E as a function of $\lambda = \frac{h_z}{2J}$ inside the fracton phase for the two-field case up to sixth order. Single excitations are immobile. Therefore, we have flat dispersion and a single contributing energy. For two excitations and varying distances between the fractons, we get only slight variation to the case of two independent particles. The diagonalized hopping terms yield a binding and anti-binding term. The two-particle energies also have a flat dispersion. Similar to the single-field case we find no evidence of a level crossings or a closing of the gap for both the one- and two-fracton regime. This excludes a second-order phase transition.

Chapter 9

Summary and Outlook

Type-II fracton phases with their completely immobile fracton excitations are a new type quantum matter in three dimensions. The degenerate ground state in this fracton phase are separated by a macroscopic energy barrier and hence are good candidates for a self-correcting quantum memory. In this thesis, we investigated Haah's code in a homogeneous magnetic in order to study its zero-temperature quantum robustness fo type-II fracton phases.

For the single-field case - i.e. the case where only either the σ or μ field contributes - we found that the high- and low-field phase are self dual. By determining the ground-state energies with pCUT in the high- and low-field limit we found a strong first-order phase transition between the topological fracton phase and the trivial phase at $h = J$. Additionally, we ruled out a second-order phase transition by determining the energies of the elementary excitations using pCUT up to th order. For the two-field case - i.e. the case where both σ and μ field contribute and are polarized in the same direction- we found a first-order phase transition at $h = 0.4560 \pm 0.0006$ by investigating the ground-state energies with pCUT up to 6th order. We studied the elementary excitations in the low-field case using pCUT up to 6th order and found no evidence for a second-order phase transition. For both cases, in the high- and low-field phase, we found a good agreement of pCUT and the variational ansatz with $6 - 16\%$ smaller critical magnetic fields for the variational ansatz. The mixed-field case - i.e. the case where both σ and μ field contribute and one of them point in x- and the other in z-direction- we found that it can be treated as two independent systems that resemble the single-field case. We verified that using both pCUT and the variational ansatz.

For all pCUT calculations we used an iterative approach to optimize the clusters. The limiting factor for higher orders is the exponentially increasing memory usage of the computer aided program.

To our knowledge, we are the first that explicitly find a strong first-order phase transition between the type-II fracton phase and the polarized phase. Additionally, we find no mechanism that could drive a second-order phase transition. Therefore, we expect only first-order phase transitions for all remaining field directions.

A good starting point for further investigations is to refine the used methods. In chapters 7.1 and 7.2, we noted that the reason for the deviating critical magnetic fields for the variational ansatz is due to the fact that the energy of the ground state in the topological phase does not change in the presence of a magnetic field. A next step could be to refine the variational state $|\alpha, \beta\rangle$. One way of doing this is to define a state that interpolates between the perturbed ground states in

leading orders instead of the exact ground states. In [42] L. Vanderstraeten et. al. successfully applied this approach to the transverse-field Ising model and to the two-dimensional toric code in a magnetic field. However, as L. Vanderstraeten et. al. pointed out, in order to get non-trivial results one has to do exponentiated perturbation theory. Hence, a variational state has the form

$$|\beta, \gamma\rangle = \exp\left(\gamma \hat{V}\right)|\beta\rangle,$$

where γ is a new variational parameter and $\hat{V}$ is the first-order perturbation. Unfortunately, this makes an analytical evaluation difficult. In [42] tensor network methods were used instead. This approach can be straight forwardly applied to Haah's code in a magnetic field. As first step, this enhanced variational ansatz could be applied to the self-dual single-field case, where we know the exact λ_c. After that one can use the enhanced variational ansatz for the two-field case and compare the results with pCUT.

As pointed out in sections 7.1 and 7.2, the limiting factor for pCUT is the memory usage. This can be drastically reduced by a graph expansion. For example in 10th order the largest contributing graphs include ten sites, while the optimized cluster for the ground state is several hundred sites big. This increased performance can then be used to determine the critical magnetic field for the two-field case better. Additionally, the improved performance can be used to get closer to calculating the whole phase-diagram for Haah's code in a homogeneous magnetic field. In this thesis we did not investigate cases with a homogeneous magnetic field in y-direction or even a general homogeneous magnetic field with arbitrary polarization. One reason for this is, that for both cases, we have to store more information - for example both the eigenvalues of the $\hat{A}_c$ and $\hat{B}_c$ operators in the low-field case. Additionally, we have more options to act with a local $\hat{\tau}_i$ operator as each of the field directions induces a $\hat{\tau}_{i,h}$ with $h \in \{x, y, z\}$. These two factors combined increase the computational cost, making it impossible to reach reasonable higher orders with the cluster optimization approach. However, with a graph expansion we can increase the performance such that we can gain insight to these field polarizations.

A different approach to characterize topological order is via the topological entropy. Han Ma et. al. in [43] determined the topological entanglement entropy for Haah's code. An interesting question to ask is how the entanglement entropy changes in the presence of a homogeneous magnetic field. In [44] Halász and Hamma determine the Rényi entropy for the toric code using pCUT applied to observables. Using this ansatz for Haah's code and including computer aided calculations could give some insight to that question. A different route is using Wilson loops. For the type-I fracton phase in the X-Cube model this was first done with Quantum Monte Carlo in [45]. In [41] M. Mühlhauser showed that pCUT can be applied in this case and yields similar results. This could now be transfered to type-II fracton phases like Haah's code.

Bibliography

[1] Gordon E Moore. Cramming more components onto integrated circuits. *Electronics*, 38(8):114, 1965.

[2] M Mitchell Waldrop. The chips are down for moore's law. *Nature News*, 530(7589):144, 2016.

[3] IEEE International Roadmap for Devices and Systems. International Roadmap for Devices and Systems (IRDS$^{\text{TM}}$) 2017 edition.

[4] Michael A Nielsen and Isaac L Chuang. *Quantum computation and quantum information*. Cambridge University Press, Cambridge, 2000.

[5] Ronald L Rivest, Adi Shamir, and Leonard Adleman. A method for obtaining digital signatures and public-key cryptosystems. *Communications of the ACM*, 21(2):120–126, 1978.

[6] Peter W Shor. Polynomial-time algorithms for prime factorization and discrete logarithms on a quantum computer. *SIAM review*, 41(2):303–332, 1999.

[7] MJ Schwarz, Jan Goetz, Z Jiang, T Niemczyk, F Deppe, A Marx, and R Gross. Gradiometric flux qubits with a tunable gap. *New J. Phys*, 15(4):045001, 2013.

[8] Peter W. Shor. Scheme for reducing decoherence in quantum computer memory. *Phys. Rev. A*, 52:R2493–R2496, Oct 1995.

[9] J Von Neumann. First draft of a report on the edvac. contract no. w-670-ord-4926. *The Origins of Digital Computers: Selected Papers, 3rd edn*, 1945.

[10] Matteo Mariantoni, Haohua Wang, Tsuyoshi Yamamoto, Matthew Neeley, Radoslaw C Bialczak, Yu Chen, Michael Lenander, Erik Lucero, Aaron D O'Connell, Daniel Sank, et al. Implementing the quantum von neumann architecture with superconducting circuits. *Science*, 334(6052):61–65, 2011.

[11] Xiao-Gang Wen. Topological orders in rigid states. *International Journal of Modern Physics B*, 4(02):239–271, 1990.

[12] Elizabeth Gibney and Davide Castelvecchi. Physics of 2d exotic matter wins nobel. *Nature News*, 538(7623):18, 2016.

[13] Sergey Bravyi, Matthew B Hastings, and Spyridon Michalakis. Topological quantum order: stability under local perturbations. *Journal of mathematical physics*, 51(9):093512, 2010.

[14] Jon M Leinaas and Jan Myrheim. On the theory of identical particles. *Il Nuovo Cimento B (1971-1996)*, 37(1):1–23, 1977.

[15] Frank Wilczek. Magnetic flux, angular momentum, and statistics. *Phys. Rev. Lett.*, 48(17):1144, 1982.

[16] A Yu Kitaev. Fault-tolerant quantum computation by anyons. *Annals of Physics*, 303(1):2–30, 2003.

[17] Chetan Nayak, Steven H. Simon, Ady Stern, Michael Freedman, and Sankar Das Sarma. Non-abelian anyons and topological quantum computation. *Rev. Mod. Phys.*, 80:1083–1159, Sep 2008.

[18] Graham P Collins. Computing with quantum knots. *Scientific American*, 294(4):56–63, 2006.

[19] Sergey Bravyi and Barbara Terhal. A no-go theorem for a two-dimensional self-correcting quantum memory based on stabilizer codes. *New J. Phys*, 11(4):043029, 2009.

[20] Sergey Bravyi and Jeongwan Haah. Energy landscape of 3d spin hamiltonians with topological order. *Phys. Rev. Lett.*, 107(15):150504, 2011.

[21] Jeongwan Haah. Local stabilizer codes in three dimensions without string logical operators. *Phys. Rev. A*, 83(4):042330, 2011.

[22] Sagar Vijay, Jeongwan Haah, and Liang Fu. Fracton topological order, generalized lattice gauge theory, and duality. *Phys. Rev. B*, 94(23):235157, 2016.

[23] David Anselm Reiss and Kai Phillip Schmidt. Quantum robustness and phase transitions of the 3D toric code in a field. *arXiv:1902.03908*, 2019.

[24] Wolfgang Nolting. *Grundkurs Theoretische Physik; Band 5: Quantenmechanik, Teil 1: Grundlagen*. Springer, 7th edition edition, 1994.

[25] Alexei Kitaev. Anyons in an exactly solved model and beyond. *Annals of Physics*, 321(1):2–111, 2006.

[26] Sébastien Dusuel, Michael Kamfor, Román Orús, Kai Phillip Schmidt, and Julien Vidal. Robustness of a perturbed topological phase. *Phys. Rev. Lett.*, 106:107203, Mar 2011.

[27] Alexei Kitaev and John Preskill. Topological entanglement entropy. *Phys. Rev. Lett.*, 96(11):110404, 2006.

[28] Michael Levin and Xiao-Gang Wen. Detecting topological order in a ground state wave function. *Phys. Rev. Lett.*, 96(11):110405, 2006.

[29] Sergey Bravyi and Jeongwan Haah. Quantum self-correction in the 3d cubic code model. *Phys. Rev. Lett.*, 111(20):200501, 2013.

[30] Sagar Vijay, Jeongwan Haah, and Liang Fu. A new kind of topological quantum order: A dimensional hierarchy of quasiparticles built from stationary excitations. *Phys. Rev. B*, 92(23):235136, 2015.

[31] Rahul M Nandkishore and Michael Hermele. Fractons. *Annual Review of Condensed Matter Physics*, 2018.

[32] F. Wegner. Flow-equations for hamiltonians. *Annalen der Physik*, 506(2):77–91, 1994.

[33] C. Knetter and S. Uhrig. Perturbation theory by flow equations: dimerized and frustrated s= 1/2 chain. *Eur. Phys. J. B*, 13(2):209–225, 2000.

[34] Richard D Mattuck. *A guide to Feynman diagrams in the many-body problem*. Courier Corporation, 1992.

[35] Christian Knetter. *Perturbative continuous unitary transformations: spectral properties of low dimensional spin systems*. PhD thesis, Universität zu Köln, 2003.

[36] Michael Kamfor. *Robustness and spectroscopy of the toric code in a magnetic field*. PhD thesis, Technische Universität Dortmund, 2013.

[37] K Coester and KP Schmidt. Optimizing linked-cluster expansions by white graphs. *Phys. Rev. E*, 92(2):022118, 2015.

[38] George A. Baker and P. R. Graves-Morris. *Padé Approximants.*, volume Second edition of *Encyclopedia of Mathematics and Its Applications*. Cambridge University Press, 1996.

[39] Andreas R Hehn. *Series expansion methods for quantum lattice models*. PhD thesis, ETH Zurich, 2016.

[40] Sébastien Dusuel and Julien Vidal. Mean-field ansatz for topological phases with string tension. *Phys. Rev. B*, 92(12):125150, 2015.

[41] Matthias Mühlhauser. Robustness of fracton phases under external magnetic fields. Master's thesis, Friedrich-Alexander-Universität Erlangen-Nürnberg, 2018.

[42] Laurens Vanderstraeten, Michaël Mariën, Jutho Haegeman, Norbert Schuch, Julien Vidal, and Frank Verstraete. Bridging perturbative expansions with tensor networks. *Phys. Rev. Lett.*, 119(7):070401, 2017.

[43] Han Ma, A. T. Schmitz, S. A. Parameswaran, Michael Hermele, and Rahul M. Nandkishore. Topological entanglement entropy of fracton stabilizer codes. *Phys. Rev. B*, 97:125101, Mar 2018.

[44] Gábor B Halász and Alioscia Hamma. Probing topological order with rényi entropy. *Phys. Rev. A*, 86(6):062330, 2012.

[45] Trithep Devakul, SA Parameswaran, and SL Sondhi. Correlation function diagnostics for type-I fracton phases. *Phys. Rev. B*, 97(4):041110, 2018.

Appendix A

pCUT contributions by hand

In this appendix, we present the contributing $\hat{T}$ operator sequences. For each matrix element, we give all contributing $\hat{T}$ operator sequences in a table. The first column is the sequence, the second the corresponding coefficient and the third the multiplicity. The multiplicity for each sequence is given as a product of integer numbers that represent the number of options to act with the $\hat{T}$ at that position in the sequence on a state to the right. The contribution of a sequence is zero if it is not listed in the corresponding table.

A.1   Ground-state energies

Low-field limit in the single-field case

We consider the matrix element

$$\langle 0| \frac{\hat{\mathcal{H}}_{\text{eff},\sigma}}{2J \cdot N_c} |0\rangle = -1 - \lambda^2 \frac{1}{4} - \lambda^4 \frac{3}{64} + O(\lambda^6).$$

The second order contribution was explicitly shown in section 7.1.2. All contributing $\hat{T}$ operator sequences up to fourth order are

$\hat{T}$-Sequence	Coef.	Mult.	$\hat{T}$-Sequence	Coef.	Mult.
$\langle 0| \hat{T}_{-4}\hat{T}_4 |0\rangle$	$-\frac{1}{4}$	$1 \cdot N_c$	$\langle 0| \hat{T}_{-4}\hat{T}_{-4}\hat{T}_4\hat{T}_4 |0\rangle$	$-\frac{1}{128}$	$1 \cdot 2 \cdot (N_c - 13) \cdot N_c$
$\langle 0| \hat{T}_{-4}\hat{T}_4\hat{T}_{-4}\hat{T}_4 |0\rangle$	$+\frac{1}{64}$	$1 \cdot N_c \cdot 1 \cdot N_c$	$\langle 0| \hat{T}_{-4}\hat{T}_{-2}\hat{T}_2\hat{T}_4 |0\rangle$	$-\frac{1}{96}$	$1 \cdot 2 \cdot 12 \cdot N_c$

A.2   Excitation energies

A.2.1   Single field case

In this section we introduce the contributing terms for the pCUT in the single-field case. The Hamiltonian reads

$$\frac{\hat{\mathcal{H}}}{2J} = -N_c + \hat{Q} - \lambda \left(\hat{T}_{\sigma,+4} + \hat{T}_{\sigma,+2} + \hat{T}_{\sigma,0} + \hat{T}_{\sigma,-2} + \hat{T}_{\sigma,-4} \right).$$

We will list the contributing $\hat{T}$ operator sequences with multiplicities and coefficients. The single-particle case is up to second order explicitly given section 8.2.

Two particle hopping

We consider the matrix element

$$\left\langle \blacksquare \middle| \frac{\hat{\mathcal{H}}_{\text{eff}}}{2J} \middle| \blacksquare \right\rangle = \lambda - \frac{3}{8}\lambda^3 + O(\lambda^4). \tag{A.1}$$

The contributing sequence are up to third order where $\langle a| = \left\langle \blacksquare \right|$ and $|b\rangle = \left| \blacksquare \right\rangle$

$\hat{T}$-Sequence	Coef.	Mult.	$\hat{T}$-Sequence	Coef.	Mult.
$\langle a| \hat{T}_0 |b\rangle$	1	1	$\langle a| \hat{T}_0 \hat{T}_{-2} \hat{T}_2 |b\rangle$	$-\frac{1}{8}$	$1 \cdot 1 \cdot 6$
$\langle a| \hat{T}_{-4} \hat{T}_2 \hat{T}_2 |b\rangle$	$\frac{1}{8}$	$1 \cdot 1 \cdot 6$	$\langle a| \hat{T}_{-2} \hat{T}_{-2} \hat{T}_4 |b\rangle$	$\frac{1}{8}$	$1 \cdot 1 \cdot 6$
$\langle a| \hat{T}_{-4} \hat{T}_2 \hat{T}_2 |b\rangle$	$\frac{1}{8}$	$1 \cdot 1 \cdot 6$	$\langle a| \hat{T}_{-2} \hat{T}_2 \hat{T}_0 |b\rangle$	$-\frac{1}{8}$	$1 \cdot 6 \cdot 1$
$\langle a| \hat{T}_4 \hat{T}_{-4} \hat{T}_0 |b\rangle$	$-\frac{1}{32}$	$1 \cdot (N_c - 6) \cdot 1$	$\langle a| \hat{T}_0 \hat{T}_{-4} \hat{T}_4 |b\rangle$	$-\frac{1}{32}$	$1 \cdot 1 \cdot (N_c - 6)$
$\langle a| \hat{T}_{-4} \hat{T}_0 \hat{T}_4 |b\rangle$	$\frac{1}{16}$	$1 \cdot 1 \cdot (N_c - 13)$			

We consider the matrix element

$$\left\langle \blacksquare \middle| \frac{\hat{\mathcal{H}}_{\text{eff}}}{2J} \middle| \blacksquare \right\rangle - \langle 0| \frac{\hat{\mathcal{H}}_{\text{eff}}}{2J} |0\rangle = 2 - \frac{5}{4}\lambda^2 + O(\lambda^3), \tag{A.2}$$

The contributing sequences up to second order with $\langle a| = \left\langle \blacksquare \right|$ are

$\hat{T}$-Sequence	Coef.	Mult.	$\hat{T}$-Sequence	Coef.	Mult.
$\langle a| \hat{T}_{-2} \hat{T}_2 |b\rangle$	$-\frac{1}{2}$	$1 \cdot 6$	$\langle a| \hat{T}_4 \hat{T}_{-4} \hat{T}_2 |b\rangle$	$-\frac{1}{4}$	$1 \cdot (N_c - 7)$

A.3   Two field case

In this section we introduce the contributing terms for the pCUT in the two-field case. The Hamiltonian reads

$$
\begin{aligned}
\frac{\hat{\mathcal{H}}}{2J} &= -N_c + \hat{Q} - \lambda \Big(\hat{T}_{\sigma^z,+4} + \hat{T}_{\sigma^z,+2} + \hat{T}_{\sigma^z,0} + \hat{T}_{\sigma,-2} + \hat{T}_{\sigma^z,-4} \\
&\quad + \hat{T}_{\mu^z,+4} + \hat{T}_{\mu^z,+2} + \hat{T}_{\mu^z,0} + \hat{T}_{\mu^z,-2} + \hat{T}_{\mu^z,-4} \Big).
\end{aligned}
$$

We will list the contributing $\hat{T}$ operator sequences with multiplicities and coefficients

One particle energy

We consider the matrix element

$$\left\langle \blacksquare \middle| \frac{\hat{\mathcal{H}}_{\text{eff}}}{2J} \middle| \blacksquare \right\rangle = 1 - 2\lambda^2 + O(\lambda^3) \tag{A.3}$$

The contributing sequences up to second order with $\langle a| = \left\langle \blacksquare \right|$ are

$\hat{T}$-**Sequence**	**Coef.**	**Mult.**	$\hat{T}$-**Sequence**	**Coef.**	**Mult.**
$\langle a|\hat{T}_{-2}\hat{T}_2|a\rangle$	$-\frac{1}{2}$	$1\cdot 8$	$\langle a|\hat{T}_4\hat{T}_{-4}|a\rangle$	$-\frac{1}{4}$	$1\cdot(N_c-8)$

Two particle hopping

We consider the matrix element

-
$$\left\langle \;\middle|\frac{\hat{\mathcal{H}}_{\text{eff}}}{2J}\middle|\;\right\rangle - \langle 0|\frac{\hat{\mathcal{H}}_{\text{eff}}}{2J}|0\rangle = 2 - \frac{13}{4}\lambda^2 + O(\lambda^3) \tag{A.4}$$

The contributing sequences up to second order with $\langle a| = \left\langle \;\middle|\right.$ are

$\hat{T}$-**Sequence**	**Coef.**	**Mult.**	$\hat{T}$-**Sequence**	**Coef.**	**Mult.**
$\langle a|\hat{T}_{-2}\hat{T}_2|a\rangle$	$-\frac{1}{2}$	$1\cdot 14$	$\langle a|\hat{T}_4\hat{T}_{-4}|a\rangle$	$-\frac{1}{4}$	$1\cdot(2N_c-15)$

-
$$\left\langle \;\middle|\frac{\hat{\mathcal{H}}_{\text{eff}}}{2J}\middle|\;\right\rangle - \langle 0|\frac{\hat{\mathcal{H}}_{\text{eff}}}{2J}|0\rangle = 2 - \frac{13}{4}\lambda^2 + O(\lambda^3) \tag{A.5}$$

The contributing sequences are up to second order with $\langle a| = \left\langle \;\middle|\right.$

$\hat{T}$-**Sequence**	**Coef.**	**Mult.**	$\hat{T}$-**Sequence**	**Coef.**	**Mult.**
$\langle a|\hat{T}_{-2}\hat{T}_2|a\rangle$	$-\frac{1}{2}$	$1\cdot 14$	$\langle a|\hat{T}_4\hat{T}_{-4}|a\rangle$	$-\frac{1}{4}$	$1\cdot(2N_c-15)$

-
$$\left\langle \;\middle|\frac{\hat{\mathcal{H}}_{\text{eff}}}{2J}\middle|\;\right\rangle - \langle 0|\frac{\hat{\mathcal{H}}_{\text{eff}}}{2J}|0\rangle = 2 - \frac{5}{2}\lambda^2 - +O(\lambda^3) \tag{A.6}$$

The contributing sequences up to second order with $\langle a| = \left\langle \;\middle|\right.$ are

$\hat{T}$-**Sequence**	**Coef.**	**Mult.**	$\hat{T}$-**Sequence**	**Coef.**	**Mult.**
$\langle a|\hat{T}_{-2}\hat{T}_2|a\rangle$	$-\frac{1}{2}$	$1\cdot 12$	$\langle a|\hat{T}_4\hat{T}_{-4}|a\rangle$	$-\frac{1}{4}$	$1\cdot(2N_c-14)$

- We consider the matrix element
$$\left\langle \;\middle|\frac{\hat{\mathcal{H}}_{\text{eff}}}{2J}\middle|\;\right\rangle - \langle 0|\frac{\hat{\mathcal{H}}_{\text{eff}}}{2J}|0\rangle = 2 - \frac{5}{2}\lambda^2 - O(\lambda^3) \tag{A.7}$$

The contributing sequences up to second order with $\langle a| = \left\langle \;\middle|\right.$ are

$\hat{T}$-Sequence	Coef.	Mult.	$\hat{T}$-Sequence	Coef.	Mult.
$\langle a | \hat{T}_{-2} \hat{T}_2 | a \rangle$	$-\frac{1}{2}$	$1 \cdot 12$	$\langle a | \hat{T}_4 \hat{T}_{-4} | a \rangle$	$-\frac{1}{4}$	$1 \cdot (2N_c - 14)$

Danksagung

An erster Stelle meiner Danksagung steht natürlich Kai Phillip Schmidt, der mir diese Arbeit ermöglicht hat. Die Betreuung war fachlich und menschlich exzellent und ich habe unglaublich viel gelernt. Der Rat und die Zusammenarbeit mit Matthias Mühlhauser haben einen großen Anteil am Gelingen dieser Arbeit. Ich bedanke mich außerdem bei der AG Schmidt und der gesamten Theorie I für die produktive und kollegiale Atmosphäre.

Meine Eltern und meine Schwester haben mich während meines ganzen Studiums immer unterstützt - Danke dafür. Nicht zuletzt danke ich Janina Baßler dafür, dass sie immer mein Sonnenschein ist.

Eigenständigkeitserklärung

Hiermit bestätige ich, dass ich die vorliegende Arbeit selbstständig verfasst und keine anderen als die angegebenen Quellen und Hilfsmittel benutzt habe. Die Arbeit wurde in gleicher oder ähnlicher Form noch keiner Prüfungsbehörde vorgelegt.

Erlangen, den _____   _____